NF-κB-INDUCING KINASE REGULATION OF DEVELOPMENT, METABOLISM, AND DISEASE

A Dissertation

by

KATHRYN M. PFLUG

Submitted to the Graduate and Professional School of
Texas A&M University
in partial fulfillment of the requirements for the degree of

DOCTOR OF PHILOSOPHY

Chair of Committee,	Raquel Sitcheran
Committee Members,	Paul Lindahl
	Joseph Rutkowski
	David Threadgill
Head of Department,	David Threadgill

December 2021

Major Subject: Genetics

ABSTRACT

NF-κB-inducing kinase (NIK), the essential upstream kinase which regulates activation of the noncanonical NF-κB pathway, has important roles in regulating immunity and inflammation. In addition, NIK is vital for maintaining cellular health through its control of fundamental cellular processes, including differentiation, growth, and cell survival. As such aberrant expression or regulation of NIK is associated with several disease states. For example, loss of NIK leads to immune defects, while the overexpression of NIK is observed in inflammatory diseases, metabolic disorders, and the development and progression of cancer.

Obesity is a predominant risk factor for metabolic syndrome, which refers to a cluster of disorders that include diabetes, cardiovascular disease and fatty liver disease. Obesity and overnutrition are associated with aberrant immune and inflammatory responses resulting in increased local fat deposition, insulin resistance and systemic metabolic dysregulation. Here we show NIK has local and systemic effects on metabolic processes. We demonstrate that NIK has NF-κB-independent and -dependent roles on adipose development and function. Independently of noncanonical NF-κB, NIK deficiency regulates mitochondrial spare respiratory capacity (SRC) and proton leak but establishes higher basal oxygen consumption and glycolytic capacity in preadipocytes and *ex vivo* adipose tissue. In addition, we demonstrate NIK promotes adipogenesis through its role in activation of the noncanonical NF-κB pathway. Strikingly, when challenged with a high fat diet, NIK deficient mice are protected against diet-induced obesity and insulin insensitivity. Overall, mice lacking NIK exhibit decreased overall fat mass and increased

energy expenditure. Our results establish that, through its influences on adipose development, metabolic homeostasis and rewiring, NIK is a driver of pathologies associated with metabolic dysfunction.

Furthermore, as aberrant expression or regulation of NIK is associated with several disease states including cancer progression it is of interest to investigate effective ways of targeting chemotherapeutics to tumor cells including that of NIK or other kinase inhibitors. A novel method of specifically targeting chemotherapeutics to tumor cells involves the conjugation of heptamethine cyanine dyes. We show that use of these dyes improves chemotherapeutic efficacy in passing the blood brain barrier and treating glioblastoma.

ACKNOWLEDGEMENTS

I would like to thank Raquel for welcoming me into her lab and believing in me over the years. I would also like to thank my lab mates for always being there for me and all the quality time we've shared. Finally, I would like to thank my family and friends for all the love and support, especially my significant other, Ryan, who has helped me through all the ups and downs that come with graduate school.

CONTRIBUTORS AND FUNDING SOURCES

Contributors

This work was supported by a thesis committee consisting of Professor Raquel Sitcheran of the Department of Molecular and Cellular Medicine and Professors David Threadgill of the Department of Veterinary Medicine, Joseph Rutkowski of the Department of Medical Physiology, and Paul Lindahl of the Department of Chemistry.

The data analyzed for Chapter II were provided in part by Dr. Dong Lee. Data depicted in Chapter III were in part published in collaboration with a TAMU chemistry lab in Journal of Medical Chemistry (DOI: 10.1021/acs.jmedchem.9b01147) and ChemMedChem (DOI: 10.1002/cmdc.201900356) .

All other work conducted for the thesis was completed by the student independently.

Funding Sources NIH & CPRIT

NOMENCLATURE

ADIPOQ- Adiponectin

ALK- Anaplastic Lymphoma Kinase

ALL- Acute Lymphoblastic Leukemia

ALT- Alanine Transferase

AP2- Adipocyte Specific protein 2

ATP- Adenosine Triphosphate

BAT- Brown Adipose Tissue

BBB- Blood Brain Barrier

C/EBP- CCAAT Enhancer Binding Protein

cIAP1/2- Cellular Inhibitor of Apoptosis Protein 1 and 2

CML- Chronic Myeloid Leukemia

CPT1α- Carnitine Palmitoyl Transferase

CREB- cAMP Response Element Binding

CRIZ- Crizotinib

CY- Cyanine

CY-DAS- Dasatinib conjugated to a cyanine dye

CY-GEM- Gemcitabine conjugated to a cyanine dye

DAS- Dasatinib

DIO- Diet-Induced Obesity

DRP1- Dynamin Related Protein 1

ECAR- Extracellular Acidification Rate

EGFR- Epidermal Growth Factor Receptor

ETYA- Eicosatetraynoic Acid

FABP1- Fatty Acid Binding Protein 1

FABP4- Fatty Acid Binding Protein 4 (aka AP2)

FA- Fatty Acids

FDA- Food and Drug Administration

FFA- Free Fatty Acids

GEM- Gemcitabine

GBM- Glioblastoma Multiforme

GLUT4- Glucose Transporter 4

GPD1- Glycerol-3-phosphate Dehydrogenase

gWAT- Gonadal WAT

H&E- Hematoxylin and Eosin

HFD- High Fat Diet

HMCDs- Heptamethine Cyanine Dyes

IκBα- Inhibitory kappa B alpha

IKKα- Inhibitory kappa B kinase alpha

IKKβ- Inhibitory kappa B Kinase beta

IKKγ- Inhibitory kappa B Kinase gamma (aka NEMO)

ingWAT- Inguinal WAT

IP- Intraperitoneally

IR- Infrared

IR-CRIZ- Crizotinib conjugated to a cyanine (infrared) dye

IV- Intravenous

KO- Knockout

LPS- Lipopolysaccharide

LTα/β- Lymphotoxin alpha/ beta

LUC- Luciferase

Map3k14- Mitogen Activated Protein Kinase, Kinase, Kinase 14 (aka NIK)

MCAD- Medium Chain Acyl-CoA Dehydrogenase

MET- Mesenchymal Epithelial Transition

MSCs- Mesenchymal Stem Cells

NFATc1- Nuclear Factor of Activated T-cells 1

NF-κB- Nuclear Factor Kappa-Light-Chain-Enhancer of Activated B Cells

NIK- NF-κB-Inducing Kinase

NIRF- Near-Infrared Fluorescence

OATPs- Organic Anion-Transporting Polypeptides

OCR- oxygen Consumption Rate

OXPHOS0- Oxidative Phosphorylation

PDGFR- Platelet Derived Growth Factor Receptor

PPARα- Peroxisome Proliferator Activated Receptor Alpha

PPARγ- Peroxisome Proliferator Activated Receptor Gamma

RANKL- Receptor Activator of NF-κB Ligand

RE- Radiant Efficiency

RFP- Red Fluorescence Protein

ROS- Reactive Oxygen Species

ROS1- ROS Proto-oncogene 1

SRC- Spare Respiratory Capacity

SLC2A4- Solute Carrier Family 2 Member 4 (aka GLUT4)

TAK1- Transforming Growth Factor Beta-Activated Kinase 1

TCA- Tricarboxylic Acid Cycle

TBK1- TANK-binding Kinase 1

TLR- Toll-like Receptor

TMZ- Temozolomide

TNF- Tumor Necrosis Factor

TRAF2/3- TNF-Receptor Associated Factor 2 and 3

TWEAK- Tumor Necrosis Factor-like Weak Inducer of Apoptosis

WAT- White Adipose Tissue

WT- Wild-type

TABLE OF CONTENTS

Page

LIST OF FIGURES

CHAPTER I

INTRODUCTION TO NF-κB INDUCING KINASE (NIK) AND NF-κB *

Canonical and Noncanonical NF-κB Signaling

NF-κB Inducing Kinase and the Noncanonical NF-κB Pathway

NIK (gene name *MAP3K14*) is well known for being the key upstream kinase to activate the noncanonical NF-κB (nuclear factor-kappa light chain enhancer of activated B cells) pathway [1]. Though initially identified by its ability to activate the canonical NF-κB pathway, loss of NIK did not impair TNF-induced activation of IKKβ/p65/p50 and NIK was subsequently shown to be essential for activation of noncanonical NF-κB signaling [2,3]. This mitogen activated, serine/threonine kinase has 4 domains including a N-terminal region for TRAF3 binding, a negative regulatory domain (NRD) that helps regulate the catalytic activity of NIK, a core kinase domain, and a C-term domain responsible for binding with proteins such as IKKα and p100 [4] (Figure 1). NIK is ubiquitously expressed but is seen to have low levels of expression due to constant degradation [5]. In steady state NIK is bound to Tumor Necrosis Factor (TNF) Receptor Associated Factor 2 and 3 (TRAF2/3) and Cellular Inhibitor of Apoptosis protein 1 and 2 (cIAP1/2). TRAF3 directly binds NIK while TRAF2 engages with cIAP1/2. Unstimulated, NIK is tagged for ubiquitination by the E3 ubiquitin ligases cIAP1/2 and is continually

degraded. Activation and stabilization of NIK occurs through cytokine binding to membrane receptors which sequesters the TRAF/cIAP complex. TRAF3 is then tagged for ubiquitination by cIAP1. Once TRAF3 has been degraded newly synthesized NIK is allowed to accumulate within the cell [6,7] (Figure 2).

Members of NF-κB

Nuclear factor-kappa light chain enhancer of activated B cells (NF-κB) refers to a family of evolutionarily conserved transcription factors that regulate a wide range of biological processes, including cell growth and survival as well as immunity and inflammation [8]. Downstream members of the mammalian NF-κB pathways include IκB (inhibitory kappa B), IKKα (inhibitory κB kinase alpha), IKKβ, IKKγ (NEMO), p105/p50 (NF-κB1), p100/p52 (NF-κB2), RelA (p65), RelB (p68), c-Rel, and Bcl-3. Members of the canonical pathway include IκBα, IKKα, IKKβ, IKKγ (NEMO), p105/p50, RelA and typically c-Rel (though c-Rel has functionality in the noncanonical pathway as well). Noncanonical NF-κB pathway proteins downstream of NIK include IKKα, p100 which is processed into p52, and RelB. RelA, RelB, c-Rel, p105/p50, p100/p52 belong to a family of Rel proteins that contain a rel homology domain that facilitates nuclear localization and DNA binding [9]. Only RelA, RelB and c-Rel contain transcriptional activation domains. NF-κB transcriptional activation occurs by heterodimers typically seen as p50/RelA or p52/RelB for the canonical or noncanonical pathways respectively. However, RelA can also dimerize with itself or p52 while RelB is not observed to form homodimers but can form a heterodimer with p50. Homodimers of p50/p50 and p52/p52 have also been observed,

but since these proteins do not contain transcriptional activation domains these dimers bind and suppress transcription [10].

NIK activity is tightly regulated by several levels of negative regulatory feedback mechanisms. For example, activation of the noncanonical NF-κB pathway requires NIK and IKKα, but not NEMO. However, NEMO was found to suppress levels of NIK protein, suggesting a role for NEMO in limiting noncanonical NF-κB signaling [11]. TANK-Binding Kinase 1 (TBK1) directly interacts with NIK in a signal-dependent manner, inducing NIK phosphorylation on Ser-862, triggering degradation independently of TRAF3, and resulting in class switching to the immunoglobulin A (IgA) isotype [12]. Additionally, IKKα also functions to phosphorylate NIK at three residues in the C-terminus (Ser-809, Ser-812, and Ser-815), which are required for degradation of NIK downstream of BAFF-R and LTβR ligation [13]. Notably, IKKα-mediated negative regulation of NIK stability is independent of TRAF-cIAP complex, which limits basal levels of NIK in unstimulated cells. Similarly, the E3 ligase CRL4DCAF2 promoted the polyubiquitination and, consequently, the degradation of NIK in dendritic cells, independent of TRAF3 degradation [14].

Noncanonical NF-κB Activation

Well characterized receptors of the noncanonical NF-κB pathway include BAFF (B-Cell activating receptor), LTβR (lymphotoxin beta receptor), CD40, Fn14, RANK (receptor activator of NF-κB), and all belong to the family of TNF receptors. Though these receptors are heavily associated with immune cell development and function, several can be found on varying cell types to help regulate cell survival and growth. Activators of the

noncanonical NF-κB include LPS (lipopolysaccharide; commonly found on the membrane of bacteria), CD40L, TWEAK (TNF-like weak inducer of apoptosis; binds specifically to Fn14 receptor), and LTα/β (lymphotoxin alpha/beta) [15].

NIK stabilization and accumulation is critical for subsequent activation of the noncanonical NF-κB pathway. NIK accumulation can trigger autophosphorylation at Thr-559 [16]. This site resides in the activation loop of NIK's kinase domain (Figure 1). Once activated NIK then binds and phosphorylates IKKα homodimers at Ser-176 and Ser-180 resulting in its activation [17]. NIK and bound IKKα then bind to p100/RelB heterodimer, where IKKα phosphorylates p100 at several serines at both the N- and C-term of p100 [18]. Phosphorylation of p100 by IKKα induces binding of ubiquitin ligase, β-TrCP, thus allowing p100 to undergo partial proteasomal processing to p52 [19,20]. In an unprocessed form p100 binds and inhibits the noncanonical transcription factor RelB. Proteasomal processing of p100 removes the C-term ankyrin repeat domain which functions similar to the inhibitory nature of mature IκB proteins. After processing of p100 into p52, p52/RelB translocate to the nucleus to regulate transcription (Figure 3). Inhibition of noncanonical activation has been studied through point mutations in the kinase domain of NIK (KK429/430AA) to form a dominant-negative, kinase dead mutant [21] (Figure 1).

Canonical NF-κB Pathway

Crosstalk between NF-κB pathways also occurs and in addition to regulating the noncanonical pathway NIK is also able to activate the canonical pathway [22]. The canonical NF-κB pathway is regulated commonly by TNF receptors, TLRs (Toll Like

Receptors), T-cell receptors, and interleukin receptors. Several inflammatory cytokines activate the canonical NF-κB pathway, the most notorious being TNFα. The canonical NF-κB pathway is well characterized for having an IKK complex consisting of IKKα, IKKβ and IKKγ, also known as NEMO. IKKα and IKKβ are the catalytic units of the complex, and IKKγ is a regulatory subunit required for activation of IKKβ. After receptor activation various kinases such as RIP1 (receptor interacting kinase 1), TAK1 (Transforming growth factor beta-activated kinase 1) and TBK1 (TANK binding kinase) can phosphorylate and activate the IKK complex, preferentially on IKKβ. Unlike the noncanonical pathway p105 is constitutively processed for a subset pool of p50, but p105 processing can also be induced by phosphorylation by IKKβ [23–25]. p50 preferentially binds RelA which is held inactive in the cytoplasm by IκBα. Active IKKβ phosphorylates IκBα inducing its proteasomal degradation. Once relieved of the inhibitory protein, p50/RelA is then able to translocate to the nucleus (Figure 3).

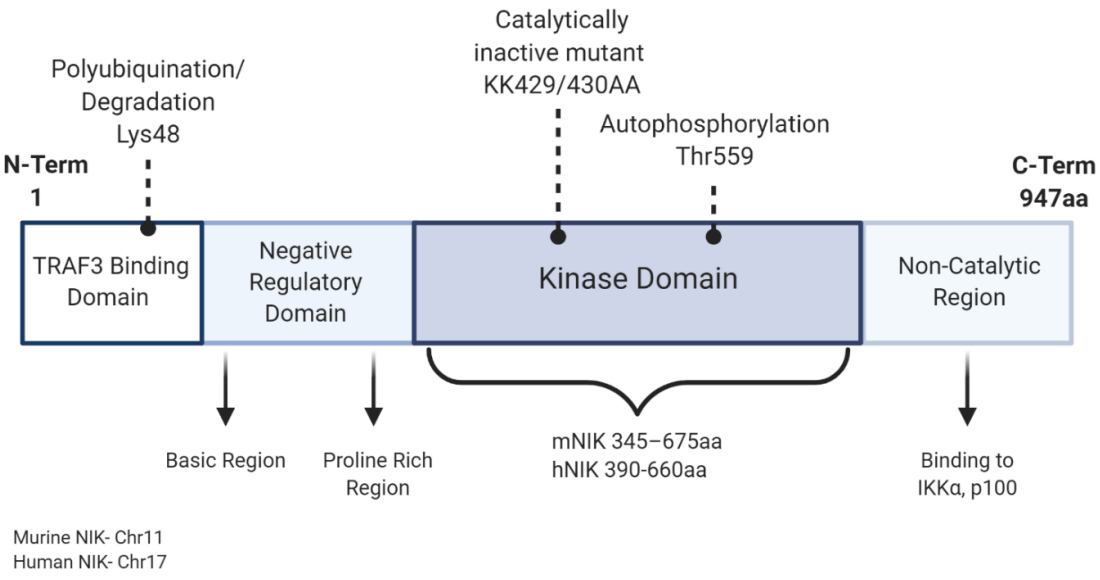

Figure 1: NIK Structure

NIK is 947 amino acids long and consists of four main domains. The *Map3k14* gene is located on chromosome 11 in mice and 17 in humans. The first domain binds NIIK specifically to TRAF3 to hold NIK inactive in the TRAF2/3/cIAPs complex. This first domain also contains a lysine (Lys48) that regulates ubiquitination. The second domain consists of a negative regulatory domain (NRD) that regulates the C-Term domain of NIK and its interaction with other proteins. The NRD consists of a basic leucine zipper and proline rich repeat motifs. The largest domain is the kinase domain, and its size varies from mouse to human orthologs. This domain contains sites for the well characterized catalytically inactive mutant (KK429A/430AA) and autophosphorylation at Thr559. The final domain allows protein binding to IKKα and p100. Adapted with permission from “NF-κB-Inducing Kinase (NIK) in Immunity, Inflammation, and Cancer” by Kathryn M. Pflug and Raquel Sitcheran, 2020. IJMS, Volume 21, 8470, Copyright by Creative Commons Attribution License.

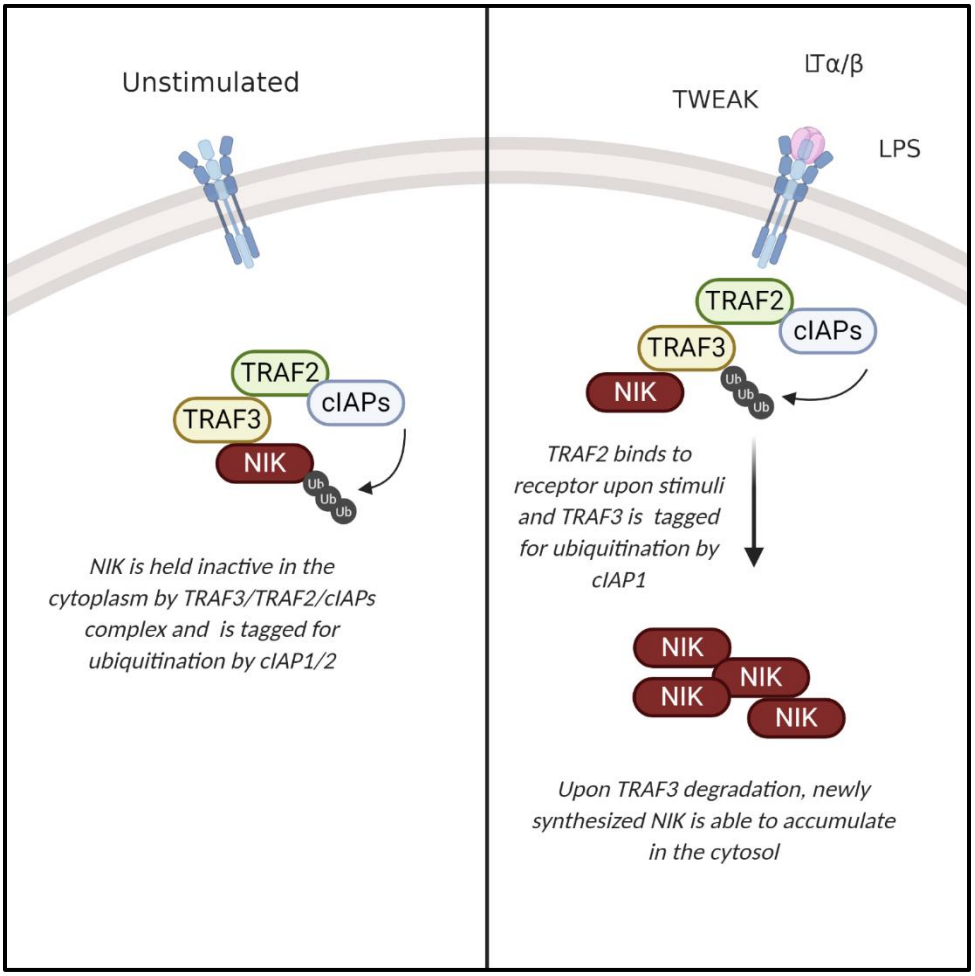

Figure 2: NIK Activation

In an inactivated state NIK is bound in a TRAF2/3/cIAPs complex where it is continuously tagged for ubiquitination. Once a receptor is bound and activated by extracellular stimuli, TRAF2 binds to the receptor and cIAP1 targets TRAF proteins for degradation. With TRAF3 degraded, newly synthesized NIK is able to accumulate in the cytoplasm. (Pflug, K.M.; Sitcheran, R. Targeting NF-κB-Inducing Kinase (NIK) in Immunity, Inflammation, and Cancer. *Int. J. Mol. Sci.* 2020, *21*, 8470. https://doi.org/10.3390/ijms21228470).

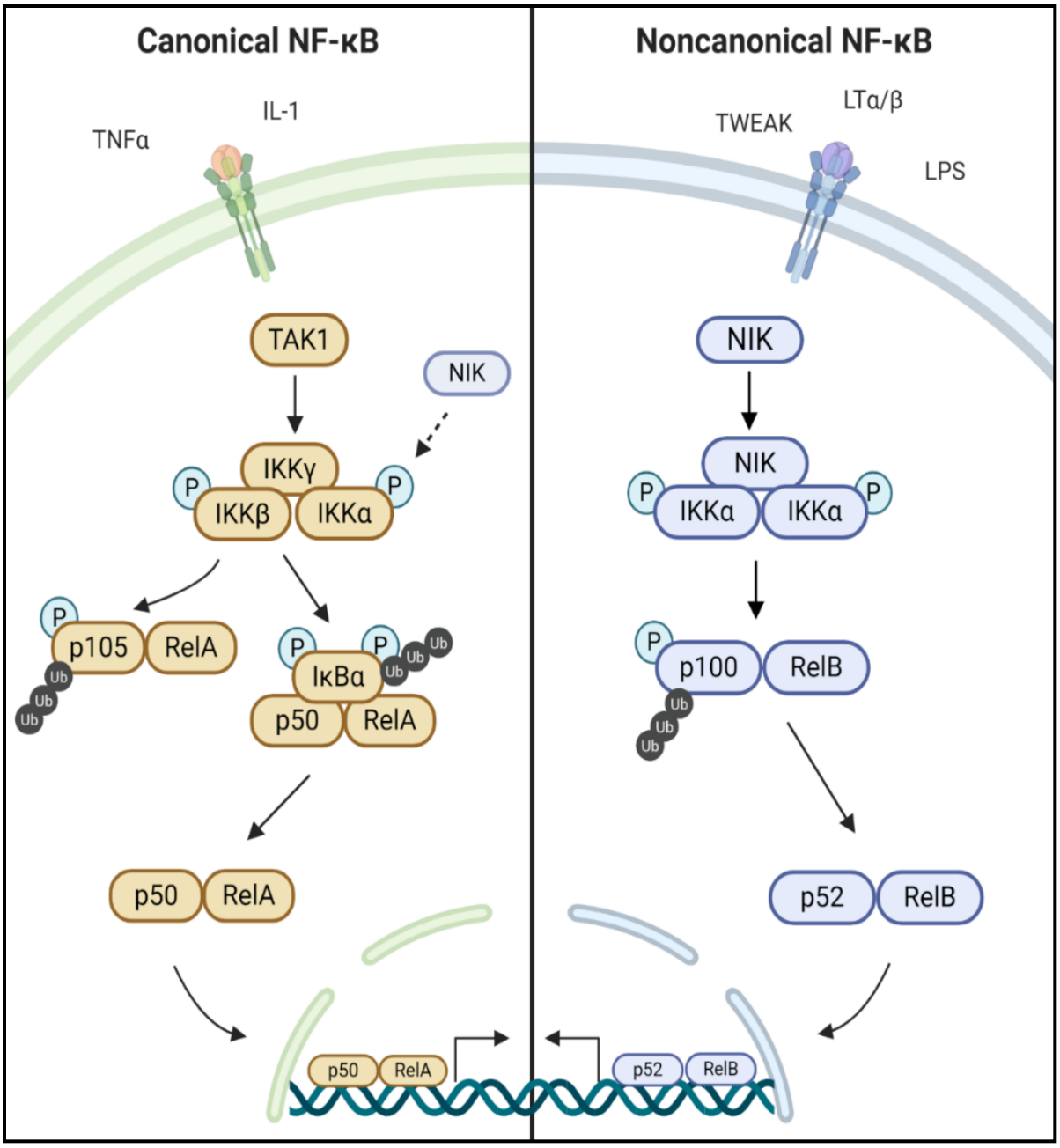

Figure 3: NF-κB Pathways

Figure 3: NF-κB Pathways

NF-κB pathways are stimulated by various cytokines, bacteria, or viruses on different receptors. Activation of the canonical NF-κB pathway leads to various kinases, including TAK1, phosphorylating the IKK complex preferentially activating IKKβ. IKKβ then phosphorylates p105 bound to RelA targeting p105 for partial proteasomal degradation into p50. Additionally, IKKβ phosphorylates IκBα targeting it for proteasomal degradation allowing p50-RelA to translocate to the nucleus. Activation of the noncanonical NF-κB pathway leads to NIK activation and subsequent phosphorylation of IKKα. IKKα then phosphorylates p100 marking it for partial proteasomal degradation into p52. RelB bound p52 is then translocated to the nucleus to regulate gene transcription. NIK is also able to facilitate canonical NF-κB pathway activation through phosphorylation of the IKKα subunit. Reprinted with permission from “NF-κB-Inducing Kinase (NIK) in Immunity, Inflammation, and Cancer” by Kathryn M. Pflug and Raquel Sitcheran, 2020. IJMS, Volume 21, 8470, Copyright by Creative Commons Attribution License.

Normal NF-κB Function

Adaptive Immunity

As the upstream regulator for the noncanonical NF-κB pathway and a kinase that can also activate the canonical NF-κB pathway, NIK has key roles in the development of cells and regulating cell processes. The importance of NIK in a mammalian model was highlighted in the study of alymphoplasia (*aly/aly*) mice which developed without lymph nodes. This phenotype was linked to a point mutation in the *Map3k14* gene that altered the C-term end of NIK, inhibiting its binding to proteins such as IKKα (Figure 4). In addition to lacking lymph nodes including Peyer's patches, these mice displayed abnormal spleen and thymus structure with a reduction in regions of white blood cell housing specifically in the marginal zone of the spleen and medulla/cortex border of the thymus. These findings highlighted a critical role for NIK in adaptive immunity.

Hematopoiesis

Germline deletion of NIK has a severe impact on hematopoiesis. *Aly*/*aly* or complete NIK KO (knockout) mice also exhibited stunted ability to mount an immune response with a reduction in B-cells and immunoglobulin development. Maturation of B-cells, particularly lymphocytes, is hindered contributing to the abnormal thymic and spleen structure as there is a reduction in immune cell viability. Many studies have shown that basal levels of immunoglobulins such as IgM and IgA are found to be reduced in mice lacking NIK. In addition these, mice are unable upregulate immunoglobulins in response to outside stressors [2,3,26,27]. Deletion of NIK in early B-cell development also produced a

phenotype of inactive B-cells particularly in periphery tissues further showing the importance of NIK in all stages of B-cell development. The B-cell phenotype in NIK KO mice mimics that of BAFF or BAFF-R KO mice showing NIK is a critical downstream component of this signaling pathway to regulate B-cell development [27,28]. In addition to regulating B-cells, loss of NIK also impacts T-cell maturation and activation. In T-cell conditional knockout of NIK thymocytes were unhindered, but development of memory and regulatory T-cells were significantly reduced in the lymph nodes and spleen as seen with an increase in naïve T-cells [29]. Furthermore, T-cells lacking NIK were seen to have a reduced antigen response, and cytokine activation compared to wild-type cells [30].

MSC Differentiation

In addition to its critical role in immunity, NIK is also important for the development of other mesenchymal cell types. Most well described is a role for NIK in osteoclast development which occurs through RANK activation, inducing noncanonical NF-κB and RelB gene regulation [31,32]. Other papers have shown that an increase in NIK activity and noncanonical NF-κB activation also increases myogenesis. The myogenic function of NIK and the noncanonical NF-κB pathway opposes the inhibitory role of the canonical NF-κB pathway, highlighting unique roles for the noncanonical pathway [33,34].

Aberrant NF-κB Regulation

As NIK has important roles in cell development, immunity and inflammation it is of no surprise that dysregulation of NIK has an impact on diseases associated with these functions. Similar to other inflammatory diseases, cancer is marked by chronic inflammation and aberrant activation of immune signaling pathways. For example, cancerous cells recruit a variety of immune cells including T-cells and macrophages, resulting in elevated levels of proinflammatory cytokines that stimulate activation of NF-κB, promoting several hallmarks of cancer, including survival, proliferation, and metastasis [35]. Aberrant, constitutive activation of canonical NF-κB signaling is a feature of several cancers [36].

Loss of NIK and Immunodeficiency

As highlighted previously, NIK has a strong role in immune response and the immunodeficient effects have been considerably studied in murine models. Dysregulation of immune function caused by mutations in NIK has also been identified in human patients as well. Patients exhibiting a defective B-cell phenotype and an increased susceptibility to viral and bacterial infections were diagnosed with primary immunodeficiency. Analysis of the patients' genetic background have identified and linked their disorder to homozygous recessive mutations within the NIK gene (*MAP3K14*). Patients with homozygous recessive mutations in NIK (Pro565Arg) displayed B-cell lymphopenia, decreased frequencies of class-switched memory B-cells, and impaired B-cell survival. [37,38]. Additionally, patients exhibited defects in both follicular helper and memory T-cells

populations, as well as natural killer cells. The NIKPro565Arg mutation resulted in impaired IKKα phosphorylation, and similarly, patients with a homozygous recessive NIKVal345Met variant exhibited combined immunodeficiency, resulting from impaired NIK kinase activity [37,38] (Figure 4).

Inflammatory Diseases

Aberrantly high NIK activation has also been linked to several other immune and inflammatory diseases. Recently, inhibition of NIK showed to increase survival in murine models of Lupus. NIK inhibition decreased overactive immune cells through a reduction in OX40, BAFF, and CD40 signaling [39]. Another disease characterized by chronic inflammation is rheumatoid arthritis which has also been linked to an increase in expression of NF-κB. In a GWAS study of two different populations with RA, NIK was found to be a genetic marker for RA susceptibility within certain ethnicities [40]. In another study of RA with tertiary lymphoid structures, surrounding endothelial cells of these structures had significantly higher expression of NIK [41]. Currently, BAFF therapeutics have been effective in treatment of arthritis, and as NIK is the downstream regulator of BAFF signaling, along with several other cytokine activated receptors, NIK is an apt target for RA therapeutics [42,43]. Commonly occurring with rheumatoid arthritis is adjacent bone loss. As NIK and the noncanonical NF-κB pathway have been shown to regulate osteoclast differentiation through RANK activation, it is reasonable that the stable activation of NIK increases osteoporosis. In one study, transgenic mice expressing NIK without its binding domain to TRAF3, allowing constitutive NIK activation, showed a

significant increase in osteoclast formation and increased bone erosion around the joints of the mice [44].

Metabolic Disorders

Parallel to inflammatory diseases, increased NIK expression has also been associated with metabolic disorders. Increased inflammation during obesity can lead to systemic complications including insulin resistance and diabetes. An increase in adipose tissue leads to recruitment or polarization of pro-inflammatory M1 macrophages. These macrophages are classically activated by LPS and INF-γ, and secrete inflammatory cytokines, most commonly TNFα [45]. Thus, stimulation of NF-κB is critical for macrophage activation and leads to subsequent elevation of NF-κB activation in surrounding cells. It is this aberrant activation that leads to insulin resistance and potentially type II diabetes [46]. Studies have shown that NIK is overactivated in several different tissues of obese mice. Mice with an adipocyte specific loss of TBK1, an inhibitor of NIK, had heightened energy expenditure and increased resistance to diet induced obesity, however these mice developed increased inflammation with an accumulation of macrophages in the adipose tissue. The increased macrophage presence and inflammation led to an decrese in insulin sensativity [47]. Overactivation of NIK in the liver of these obese mice lead to glucose intolerance by inducing hyperglycemia through an increase in glucagon activity via CREB [48]. Further investigation demonstrated that the inhibition of NIK protected obese mice from liver inflammation and steatosis in a manner that was dependent on hepatocyte-immune crosstalk, as loss of NIK in hepatocytes or Kupffer cells (liver resident macrophages) alone was not enough to protect against steatosis [49]. A separate study also linked NIK to

liver inflammation and steatosis under an alcoholic liver disease model by suppression of PPARα and fatty acid oxidation in a MEK/ERK dependent manner. This study demonstrated that NIK binds to and phosphorylates MEK and ERK1/2, which in turn phosphorylates PPARα, leading to its inhibition and a reduction in β-oxidation genes. *In vivo* treatment with a NIK inhibitor, B022, ameliorated liver steatosis and inflammation after ethanol feedings by reducing PPARα phosphorylation and inhibition to β-oxidation [50]. Obesity induced glucose intolerance by NIK was also observed in pancreatic β-cells leading to β-cell dysfunction and a decrease in insulin production. This was demonstrated through both use of a SMAC mimetic, that increases NIK stability, and through diet-induced obesity, and highlighting that the overactivation of NIK led to dysregulation of glucose homeostasis in a NF-κB related manner [51]. A study utilizing biopsies from human patients demonstrated that higher protein expression of NIK was found in the muscle of obese patients with metabolic syndrome and that NIK was seen to decrease in the same patients after weight loss by gastric bypass. Further analysis showed that increased NIK activity impaired insulin sensitivity within the muscle samples which could be ameliorated by adiponectin [52]. A separate study though, demonstrated that in mice expressing a muscle-specific super-repressor IκBα, for inhibition of the canonical NF-κB pathway, had improved insulin sensitivity with associated changes in noncanonical NF-κB proteins, including an increase in NIK [53]. In addition to regulation of insulin and glucose signaling, NF-κB was also shown to promote oxidative metabolism in myocytes through direct induction of PGC-1β [54]. Independently of the noncanonical NF-κB pathway, NIK was found to regulate mitochondria dynamics and mitochondria efficiency, by regulation of spare respiratory capacity, through DRP1 phosphorylation in glioma cells. Overall

showing NIK promoted oxidative capacity particularly in response to bioenergetic stressors [55,56]. Regulation of glycolysis by NIK has also been shown in T-cell metabolism. Glycolytic induction in CD8+ effector T-cells was regulated by indirect NIK stabilization of hexokinase 2 (HK2) [57]. Inhibition of NF-κB pathways, including NIK itself, has been advocated as a suitable therapeutic intervention to protect against diet induced metabolic disorders [58].

Cancer

NF-κB regulates many biological functions that are associated with the hallmarks of cancer, including cell proliferation, survival, angiogenesis, inflammation, invasion, and metastasis. Given this dynamic regulation of cellular processes, NF-κB, including NIK is commonly dysregulated in several cancer types to promote pro-tumorigenic environments [59]. In these cases, while NF-κB typically functions as a tumor promoter, it can also function as a tumor suppressor [60]. In contrast to the canonical NF-κB pathway, which has been extensively studied in cancer, roles for NIK and the noncanonical NF-κB pathway in cancer are still emerging. Nevertheless, it is evident that similar to canonical NF-κB signaling, dysregulation of NIK and noncanonical NF-κB can lead to the formation and progression of several types of cancer, while in some cases NIK suppresses tumorigenesis [61]. The initiation and progression of various cancers by NF-κB has been studied by dysregulation of individual subunits or of the pathways as a whole. Cancer models for NIK and the noncanonical NF-κB pathway have been analyzed at various stages from TRAF2/3 or cIAP degradation, to accumulation of NIK itself, to IKKα and its

phosphorylation by NIK, or finally by increased expression or translocation of the downstream transcription factor RelB [62].

Upregulation of NIK mRNA was shown to play an important role in maintaining the population of breast cancer stem cells (CSCs), which possess intrinsic properties of self-renewal and are important for tumor development, recurrence and metastasis, particularly in the context of therapy resistance [63,64]. Knockdown of NIK reduced expression of breast CSC markers, reduced stem cell clonogenicity and impaired tumorigenic potential in xenograft breast cancer mouse models [64]. Furthermore, a separate study demonstrated that specific deletion of RANK or IKKα in mouse mammary epithelial decreased tumorigenesis and invasive carcinoma [65]. In GBM initiating cells (GICs) it was found that NIK accumulation and noncanonical NF-κB activation was induced through epithelial V-like antigen (Eva1) degradation of TRAF2 and cIAP. This study further showed that the knockdown of RelB inhibited the self-renewal properties of human GICs and abolished tumorigenesis of mouse stem cells in vivo [66]. Increased expression of RelA, RelB and IKKα was also observed in ovarian CSCs, and knockdown of IKKα decreased stem cell marker expressions in those cells [67].

Dysregulation of NIK also leads to the formation and progression of several types of cancer. As NIK and the noncanonical NF-κB pathway have a crucial role in hematopoiesis, it is reasonable that the dysregulation of this pathway can lead to various leukemias. One study of Acute Myeloid Leukemia (AML) found the stabilization of NIK and subsequent RelB activation improved myeloid viability through gene regulation and inhibition of the canonical NF-κB pathway [68]. Further proposing NIK activation as a therapeutic target for AML. NIK inhibition has also been shown to be a therapeutic option

for immune derived cancers. One study demonstrated NIK and the noncanonical NF-κB pathway was stably activated in Hodgkin Lymphoma (HL) cell lines and tumors, and treatment with a NIK inhibitor significantly reduced HL cell viability [69].

NIK activation has also been observed in several other cancer types. Once study observed NIK stabilization in various melanoma line and highlighted that NIK/ noncanonical NF-κB activation was mediated through AKT/ERK signaling [70]. In another melanoma study the knockdown of NIK reduced melanoma cell survival through reduction of noncanonical NF-κB pathway activation and subsequent reduction on pro-survival genes [71]. NIK overactivation was also characterized in human pancreatic cancer samples, where TRAF2 degradation increased NIK stabilization [72]. Furthermore, NIK overactivation was observed to have a role in cell survival and proliferation in pancreatic cancer cell lines implicating NIK as therapeutic target to inhibit the cancer cell's growth [73]. In a human study of patients biopsied with gastric cancer, NIK was not only highly expressed in tumor tissue, but it was found to be significantly associated with tumor differentiation and had a higher positive rate in later stages of the cancer [74].

Our work has highlighted mechanisms of NIK regulation of cancer progression by invasion with an emphasis in glioma. Our earlier work identified NIK driven glioma invasion through TWEAK and noncanonical NF-κB activation. MMP9 (matrix metalloprotease 9) upregulation promoted glioma cell invasion in a noncanonical NF-κB dependent manner. Through *in vivo* experiments we showed that overexpression of NIK was substantial to significantly induce tumor cell invasion and increase tumor size [75]. Subsequently, in later studies we showed that NIK also regulates cancer cell invasion by NF-κB independent mechanisms. Within glioma, pancreatic, breast cancer and normal

fibroblast cell lines, we observed a discrete pool of NIK localizing to the mitochondria. We found this pool of NIK to associate with mitochondrial protein, DRP1 (dynamin related protein 1) increasing mitochondria trafficking to the periphery of cancer cells assisting in cell invasion [55].

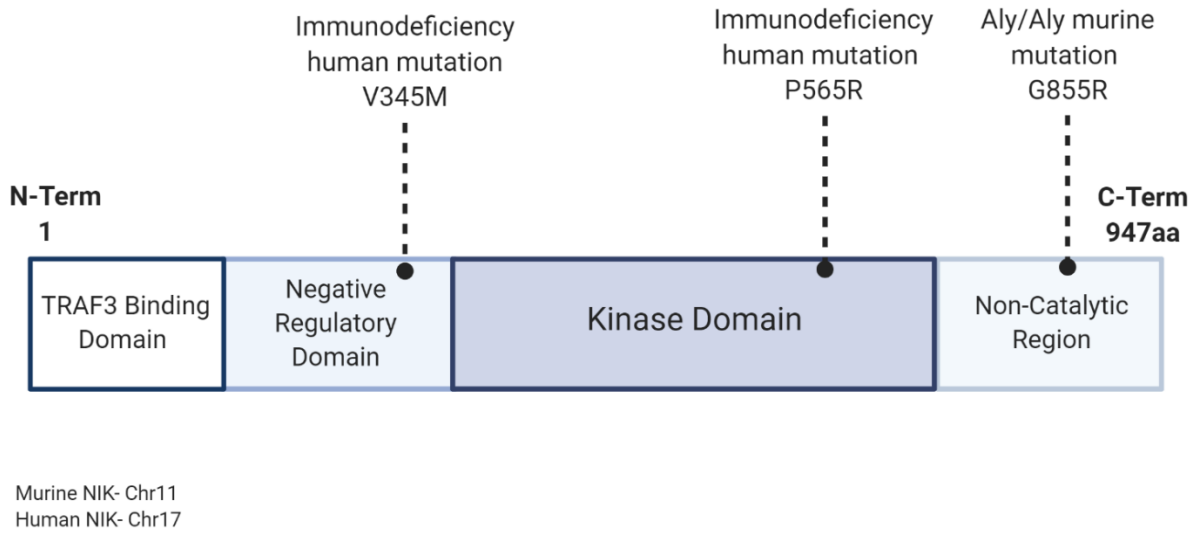

Figure 4: NIK Mutations in Diseases

A novel mutation (V345M) founded in a human immunodeficient patient resides in the negative regulatory domain. Another characterized point mutation found in human immunodeficient patients (P565R) lies in the kinase domain. Point mutation (G855R) found to cause the immunodeficient phenotype in alymphoplasia mice was found in the non-catalytic region of NIK. Adapted with permission from “NF-κB-Inducing Kinase (NIK) in Immunity, Inflammation, and Cancer” by Kathryn M. Pflug and Raquel Sitcheran, 2020. IJMS, Volume 21, 8470, Copyright by Creative Commons Attribution License.

CHAPTER II

NF-κB-INDUCING KINASE REWIRES METABOLIC DEMAND AND PROMOTES DIET-INDUCED OBESITY

Introduction

Metabolic homeostasis relies on a balance between inputs such as glucose and oxygen necessary for energetic processes and utilization of catabolic pathways involving glycolysis and oxidative phosphorylation (OXPHOS) for efficient energy production [76,77]. Utilization of these major metabolic pathways is dynamic and shifts in response to alterations in cellular states or stress [78]. Glycolysis and OXPHOS are interwoven and dysregulation in one can alter the flux or rate of the other [79–81]. Although glycolysis yields low amounts of ATP its utilization is important for feeding into the TCA cycle and electron transport chain, for rapid production of ATP, or for cells under low oxygen availability [82–84]. Oxidative phosphorylation, or aerobic respiration, is more commonly utilized to meet ATP demands. Important to mitochondria respiration is the spare respiratory capacity (SRC) which is a measurable indicator of the mitochondria's ability to upregulate oxygen consumption to ramp up ATP production and meet changes in energetic demand [85–87]. As such, mitochondrial SRC is important indicator of mitochondrial fitness and the ability of a cell to adapt to bioenergetic stress.

Metabolic syndrome is becoming increasingly common through a dysregulation in metabolic homeostasis. Typically, due to an excess energy intake, metabolic syndrome

is characterized by inflammation, insulin resistance, hyperglycemia, lipodystrophy, and obesity. Adipose tissue is an essential organ to assist in this maintenance of metabolic homeostasis [88–90]. Through lipogenesis, adipose tissue acts as a reservoir for glycerol and excess fatty acids, then by lipolysis this organ supplies important fuel for glycolytic and mitochondria respiratory processes to meet energetic demands[91]. Adipose tissue is also a critical organ that is both effected by and attributes to metabolic syndrome. During states of energy excess, such as with diet-induced obesity, adipose tissue depots retain more lipid, increasing local inflammation, which then induces insulin resistance, contributing to a state of hyperglycemia and lipodystrophy [92,93].

Nuclear Factor-κB (NF-κB)-inducing kinase (NIK) is a serine, threonine protein kinase that is essential for activation of the noncanonical NF-κB pathway. NIK phosphorylates Inhibitor of κB-kinase-α (IKKα), to trigger p100 processing to p52 and generation of transcriptionally active p52-RelB complexes [94–97]. As an activator of a conserved immune pathway, NIK has been documented to have critical roles in B-cell, lymphocyte, and lymph node development, along with other immune functions such as immunoglobulin production and T-cell function [27,94,98–101]. Furthermore, more studies have highlighted important NF-κB-independent metabolic functions for NIK including roles in mitochondrial dynamics, metabolic reprograming under nutrient stress in cancer cells, as well as regulation of glycolysis in T-cells [56,57,102]. In response to diet-induced obesity, NIK has been demonstrated to regulate hyperglycemia by increasing glucagon activity and liver steatosis through induction of fatty acid oxidation [103–105]. Interest in understanding immune regulation of metabolic processes, such as in states of immunodeficiency, has considerably increased in recent years.

Here we investigate, a functional and developmental role for NIK in influencing metabolic homeostasis, highlighting regulation of adiposity and mitochondria respiration through SRC and proton leak. We specifically illustrate how NIK deficiency decreases overall adiposity and, in a noncanonical NF-κB-independent manner, mitochondria SRC. NIK deficient cells and tissue work at higher oxygen consumption rates (OCR) to increase basal rates of OXPHOS. This phenotype is accompanied by a significant increase in glycolytic activity in both *in vitro* and *in vivo* data. Consistent with changes in metabolism, NIK deficiency also inhibits adipocyte differentiation in a noncanonical NF-κB-dependent manner through regulation of key adipogenic transcription factors. Strikingly, taken together, NIK deficiency protects mice from developing metabolic syndrome under a high-fat-diet model, as NIK KO mice remain leaner, have increased insulin sensitivity, and higher glucose uptake (Figure 5).

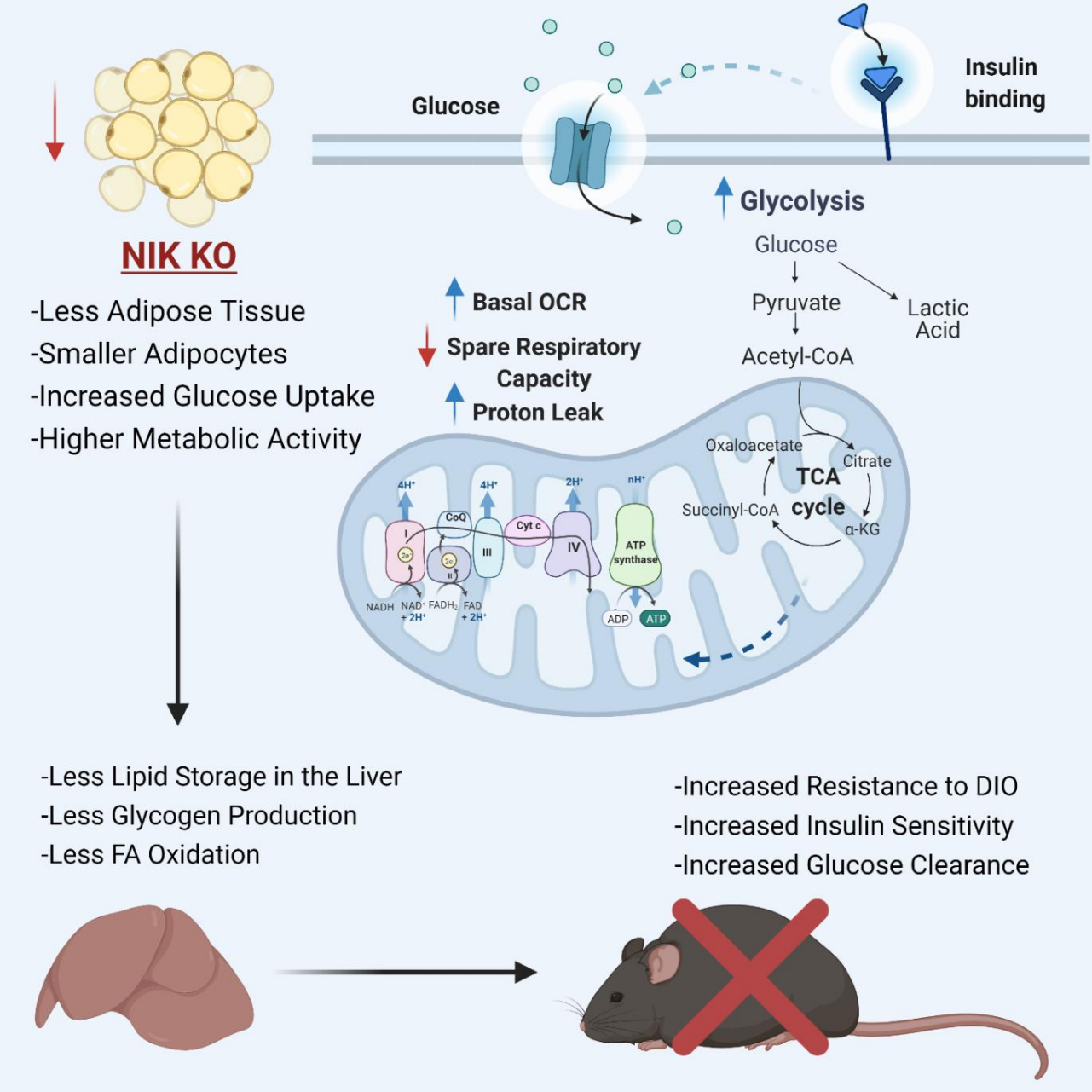

Figure 5: NIK Regulates Metabolic Homeostasis and Susceptibility to Diet-Induced Obesity

Figure 5: NIK Regulates Metabolic Homeostasis and Susceptibility to Diet-Induced Obesity

Schematic showing the effects that NIK-deficiency has on metabolic homeostasis including glucose uptake, glycolytic and oxidative phosphorylation rates, and lipid storage. Loss of NIK increases glucose uptake and basal ECAR (extracellular acidification rate) and OCR (oxygen consumption rate), while decreasing spare respiratory capacity (SRC) and increasing proton leak in mitochondria. Overall, NIK KO store less fat and on a high-fat diet (HFD) NIK KO mice have higher insulin sensitivity, glucose clearance, and increased resistance to diet-induced obesity (DIO).

Results

NIK KO Mice Display a Reduction in Overall Fat Mass

Analysis of visceral adipose tissue revealed that gonadal white adipose tissue (gWAT) deposits were substantially reduced in male and female NIK KO mice compared to WT and HET mice (Figure 6A,B, Appendix A, Supp. Figure 1A). Subcutaneous adipose was also observed to be reduced in NIK KO inguinal depots (ingWAT) (Appendix A, Supp. Figure 1B). Consistent with individual fat depot analysis, whole body composition assessment of live animals using EchoMRI^{TM}, demonstrated that male and female NIK KO mice had significantly less total fat mass, coupled with a higher lean mass ratio relative to body weight (Figure 6C,D). Moreover, while WT mice exhibited an increase in fat mass as they aged from 2 to 4 months, NIK KO mice maintained a reduced fat mass ratio (Figure 6E, Appendix A, Supp. Figure 1C,D). Although NIK KO mice gained less fat, they did not consume less food or water, nor were they more physically active than their littermates. On the contrary NIK KO mice ate and drank more than their WT littermates (Figure 7A-C). Also, NIK KO mice did not significantly differ in weight compared to WT mice until 15 weeks of age in males (Figure 6F), at which point the rate of fat mass development in WT mice surpassed the rate of body growth and adipose development of NIK KO mice. While adipocyte size was observed to be heterogeneous in NIK KO mice, they were generally smaller compared to WT mice, particularly in male mice (Figure 6G,H). This reduction in adipocyte size is to a lesser extent than the overall reduction in adipose mass, which was confirmed after comparing the ratio (noted on figure) between WT and NIK KO in the reduction of adipose mass and the ratio reduction in adipocyte size, suggesting that the observed reduction in adiposity in NIK KO mice is due to a

decrease in both adipocyte size and number (Figure 6H,I). Having observed reductions in adipocyte size and adipose mass, livers were examined for exogenous lipid accumulation which can occur due to defects in adipocyte function [106,107]. Oil Red O staining of liver sections revealed no differences in lipid accumulation between WT and NIK KO mice (Figure 7D). Taken together, these data suggest a role for NIK in the development of adipose tissue *in vivo*.

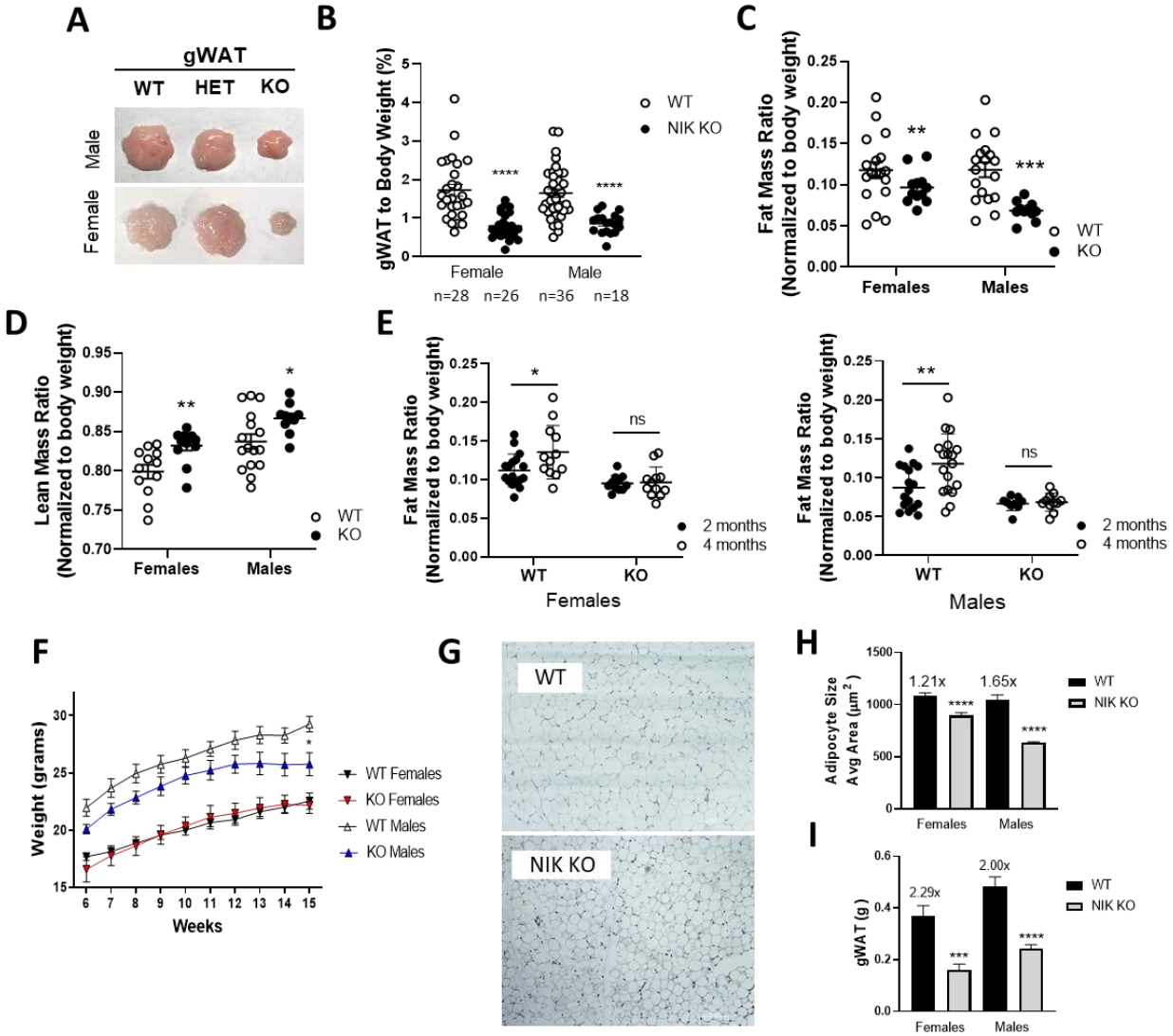

Figure 6: NIK KO Mice Display a Reduction in Overall Fat Mass

Figure 6: NIK KO Mice Display a Reduction in Overall Fat Mass

(A) Gonadal adipose tissue from male or female *Map3k14* littermates at 4 months of age. **(B)** Weight of gonadal fat between WT and NIK KO male and female *Map3k14* mice normalized to mouse weight. Data are represented as mean ± SD, Unpaired Student t-test. **(C)** EchoMRI^{TM} measurements of overall fat and lean mass **(D)** of 4-month-old male and female mice normalized to body weight (Female *Map3k14* mice; WT n= 12 and KO n=12, Male *Map3k14* 4 mice; WT n=17 and KO n=10. Data represented at mean ± SEM, Unpaired Student t-test). **(E)** Fat mass ratio from body composition data of WT and NIK KO mice at 2 and 4 months of age. (Female *Map3k14* mice; WT at 2 months n=17, WT at 4 months n=12, KO at 2 months n=11 and KO at 4 months n=12. Male *Map3k14* mice; WT at 2 months n=17, WT at 4 months n=18, KO at 2 months n=9 and KO at 4 months n=11. Data represented at mean ± SD, Sidak's Multiple Comparisons Test). **(F)** Average weights of WT and NIK KO mice between males and females from 6-15 weeks (Female *Map3k14* mice; WT n= 9 and KO n=7, Male Map3k14 mice; WT n=6 and KO n=5). Data represented at mean ± SEM, Sidak's Multiple Comparisons Test. **(G)** Hematoxylin and Eosin staining of gonadal white adipose tissue from WT and NIK KO female mice. **(H)** Image J quantification of the gonadal histology comparing adipocyte size between WT and NIK KO mice. **(I)** Weight of gonadal fat between WT and NIK KO male and female *Map3k14* mice. Data represented as mean ± SEM **(H,I)** Unpaired Student t-test.

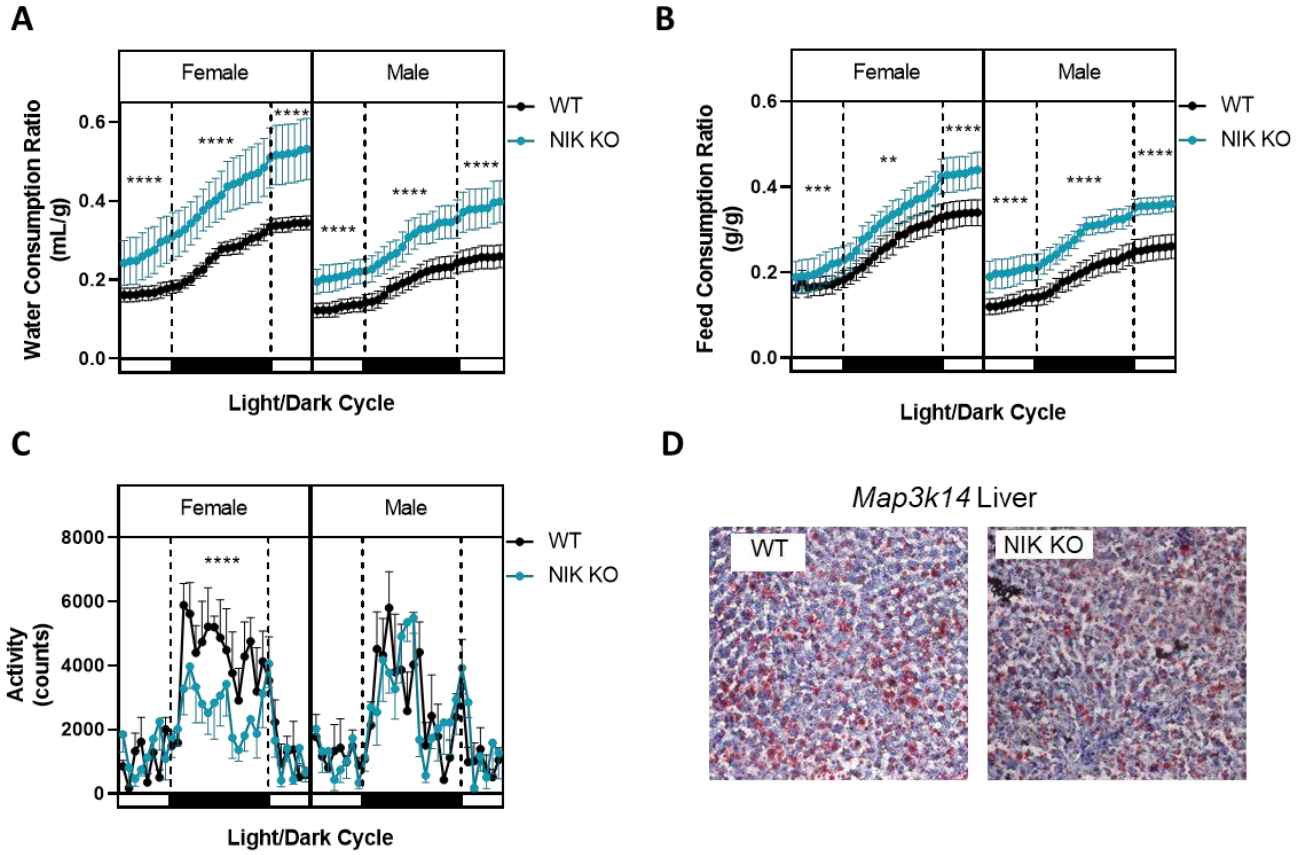

Figure 7: Map3k14 Mouse Behavior

Metabolic cage data of male and female WT, HET, NIK KO mice at 4 months of age for food consumption **(A)**, water consumption **(B)**, and activity **(C).** Data are represented as mean ± SEM, *p≤.05, ** p ≤.01, **** p ≤.0001, Unpaired Student t-test (Females WT n=5, NIK KO n=6; Males WT n=4, NIK KO n=4). **(D)** Oil Red O and hematoxylin staining of liver sections from chow fed WT and NIK KO mice (representative image of n=3 from male mice).

NIK Regulates Mitochondria Efficiency and Metabolic Activity

We previously demonstrated that NIK regulates mitochondrial dynamics in glioblastoma cells by promoting mitochondria fission [102]. Similarly, C3H10T1/2 cells, a multipotent stem cell line capable of differentiating into adipocytes, exhibited larger, more fused mitochondria in the absence of NIK (Figure 8A,B), suggesting that NIK also regulates mitochondrial dynamics in adipocyte precursor cell lines. Elongated mitochondria have also been associated in increased OXPHOS activity in several cell types including MSCs[108]. Given the reduction in adipocyte size and changes in mitochondria morphology in NIK KO cells, we sought to determine whether adipocyte metabolism was also altered in absence of NIK. Compared to WT cells, preadipocytes lacking NIK (3T3-L1 NIK-KO) displayed increased basal oxygen consumption rate (OCR) and ATP production. NIK KO cells exhibited an even more striking reduction of mitochondrial spare respiratory capacity (SRC), which is the difference between basal and maximal respiration rates and an indicator of mitochondrial fitness. Additionally, NIK KO cells also exhibited an increase in the proton leak, quantified by the OCR rate after oligomycin treatment. Ectopic expression of human wild-type NIK in NIK KO cells (NIK KO-hNIK) restored OCR and SRC, demonstrating that the observed mitochondrial defects are NIK-dependent. Overall, these data indicate that mitochondria in cells lacking NIK are functional and more oxidative, consistent with their fused phenotype, but are incapable of at efficiently upregulating OXPHOS to meet changes in energy demand. NIK-dependent regulation of OXPHOS does not require noncanonical NF-κB signaling, as cells lacking RelB, which is activated downstream of NIK, do not have impaired OCR/SRC (Figure 8C).

Next, we evaluated whether NIK regulates glycolysis in addition to OXPHOS in preadipocytes. Similar to OCR, 3T3-L1 NIK KO cells exhibited significantly higher basal extracellular acidification rate (ECAR). NIK KO cells also exhibited the most robust increase in glycolysis after glucose treatment. Further analysis of the glycolytic stress test highlighted a higher capacity in 3T3-L1 NIK KO cells to upregulate glycolysis with considerable increases in maximum glycolytic rate, glycolytic capacity, and glycolytic reserve (Figure 8D). Together, our results demonstrated that while adipose cells lacking NIK have decreased mitochondrial SRC, overall, they exhibit a significantly higher metabolic demand, with increased glycolysis and basal OXPHOS.

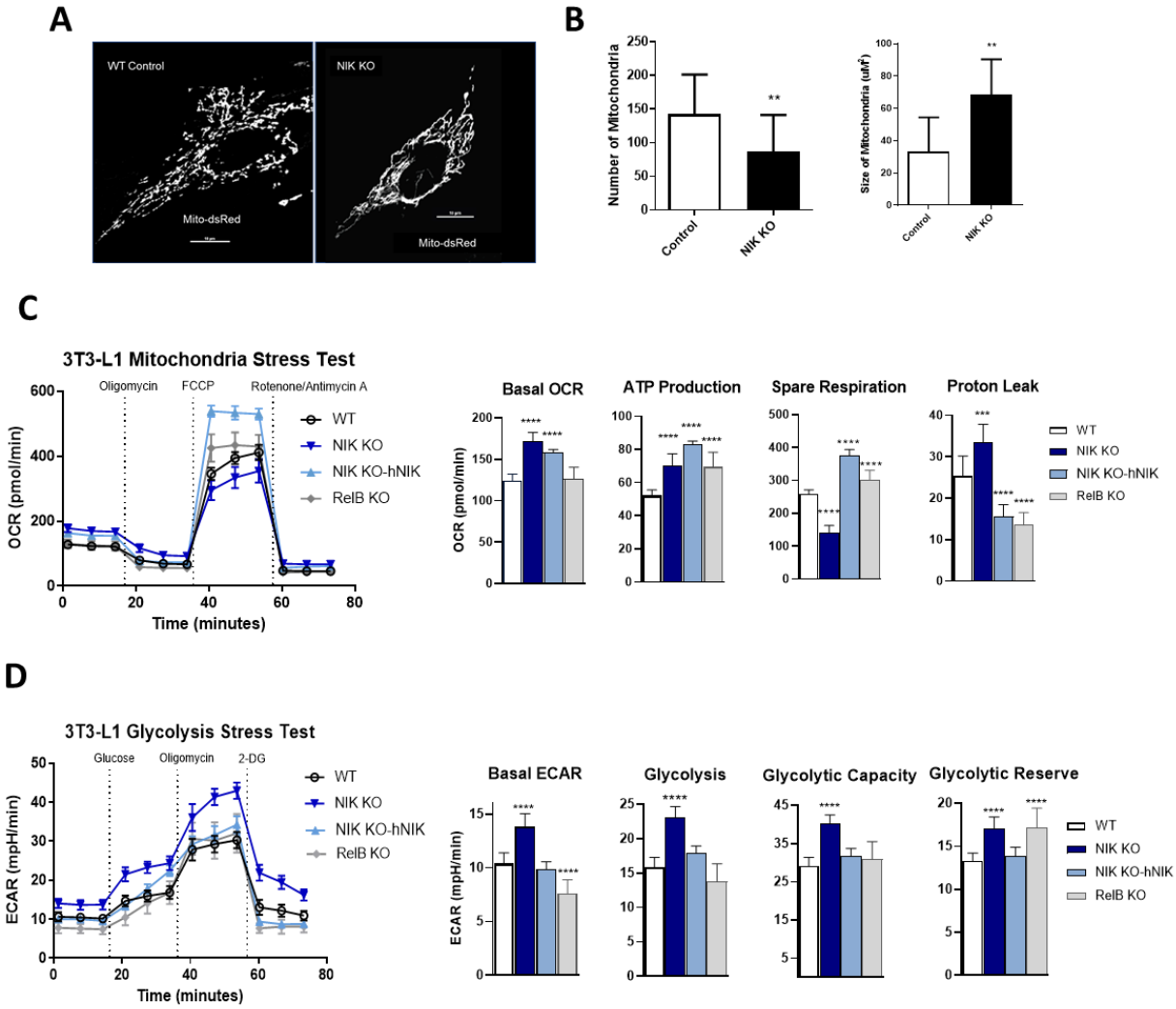

Figure 8: NIK Regulates Mitochondria Efficiency and Metabolic Activity

(A) C3H10T1/2, mouse stem cells, transfected and stained with Mito-dsRed. **(B)** Image J quantification of Mito-dsRed transfected WT and NIK KO C3H10T1/2 cells. Data represented as mean ± SD, Unpaired Student t-test. **(C)** Seahorse extracellular flux analysis of 3T3-L1 preadipocytes with either oxidative stress test (mitochondria stress test) or with **(D)** glycolysis stress test. **(C,D)** Data represented as mean ± SEM, Unpaired Student t-test (n=8 technical replicates).

Metabolic Demand Increases in NIK KO Adipose Tissue

In order to determine if the metabolic differences we saw NIK KO preadipocytes were translational to NIK KO mice, we analyzed OXPHOS and glycolytic rates on *ex vivo* adipose tissue. Similar to *in vitro* data, NIK KO adipose tissue samples displayed higher basal OCR rates and ATP production. Both NIK KO adipose tissue types also displayed a decrease in SRC and an increase in proton leak, with greater differences seen in the inguinal adipose depot than the gonadal. (Figure 9A). More characteristic of the metabolic phenotype with the loss of NIK is the robust increase in glycolysis which is emulated between both adipose types (Figure 9B). Extracellular flux analysis between both *in vitro* and *in vivo* samples clearly demonstrated an increase in energetic demand with the loss of NIK, resulting in higher metabolic rates, more so with glycolysis. Total ATP measurements also indicated higher energy output from NIK KO inguinal WAT, about 1.5x more than WT, and similar ATP levels in the gonadal WAT compared to WT (Figure 9C). Related to the considerable increase in glycolysis, we also saw an increase in glucose uptake in the NIK KO adipose tissue with ingWAT and gWAT being 1.4x and 1.3x higher than WT respectively (Figure 9D). NIK KO tissue also responded to the β-agonist and lipolytic stimulant, isoproterenol, more so in the gWAT compared to WT, indicating functional adipocytes with an ability for lipid turnover (Figure 9E). Overall, *in vitro* and *in vivo* data with the loss of NIK display similar metabolic dynamics, exhibiting a higher energy demand with a greater increase in glycolysis, and a regulation of mitochondria function through SRC and proton leak by noncanonical NF-κB-independent NIK roles.

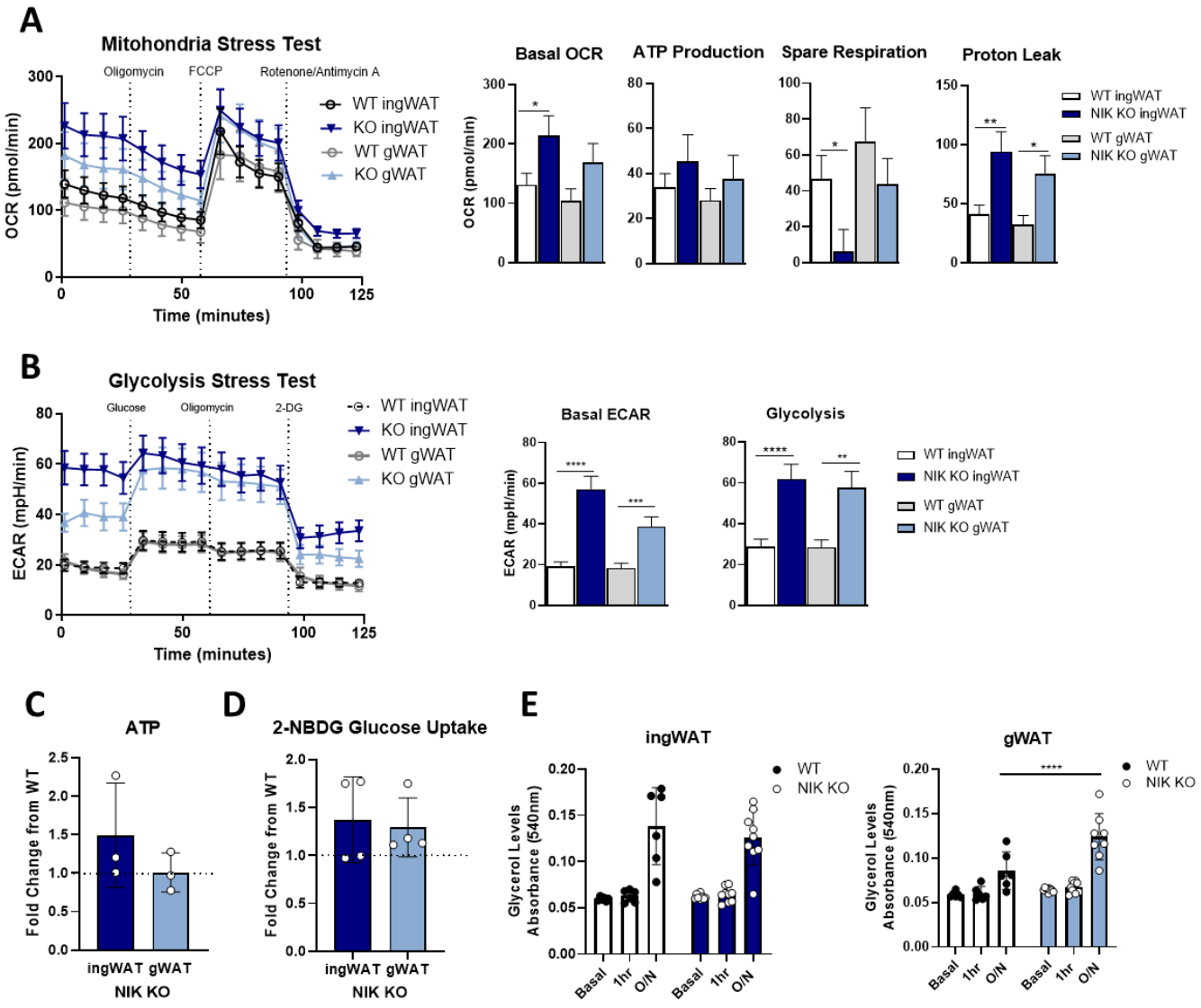

Figure 9: Metabolic Demand Increases in NIK KO Adipose Tissue

Figure 9: Metabolic Demand Increases in NIK KO Adipose Tissue

(A) Seahorse extracellular flux analysis of mouse gonadal or inguinal WAT with either oxidative stress test (Mitochondria Stress Test) or with **(B)** Glycolysis Stress Test. **(A,B)** WT n=5, KO n=4 male mice. **(C)** Overall ATP analysis of mouse gonadal or inguinal WAT by luminescence from ATPlite kit. NIK KO tissue fold change compared to WT tissue. WT base line represented at 1. Data represented as mean ± SEM, Unpaired Student t-test. **(D)** Analysis of glucose uptake by fluorescent 2-NBDG of mouse gonadal or inguinal WAT. NIK KO tissue fold change compared to WT tissue. WT base line represented at 1. **(E)** Glycerol levels of gonadal or inguinal WAT with lipolysis stimulated with isoproterenol and measured at 1 hour and then after overnight incubation. Sidak's Multiple Comparison Test. **(C-E)** Data represented as mean ± SD.

NIK KO Mice Exhibit Systemic Sex Specific Metabolic Differences

With observed differences in cellular and whole tissue analysis with the loss of NIK, we then examined NIK KO mice for systemic differences in metabolism. Whole body metabolism was measured across light and dark cycles using metabolic cages to analyze respiratory rates and energy expenditure of individual mice along with feed and water intake and activity. Overall, female NIK KO mice displayed a higher oxygen consumption and carbon dioxide production rate throughout both periods of the day, than their WT counterparts, while NIK KO males displayed rates similar to WT (Figure 10 A, B). Consequentially, NIK KO mice had a higher trend for respiratory exchange rate, indicative of greater glucose oxidation over fatty acid oxidation (Figure 10C) [109]. Moreover, this data revealed that NIK KO mice at 4 months of age displayed a higher overall energy expenditure, exhibited more so in females than males (Figure 10D). In addition to increased metabolic outputs, NIK KO mice also maintained higher temperatures at 2 months of age, with female mice maintaining elevated temperatures as seen at 4 months (Figure 10E,F). While male mice displayed adipose specific increases in metabolism from extracellular flux analysis, only female mice exhibited systemic differences. This trend for an overall increase in whole body metabolic activity in the NIK KO mice is observable in aging mice, indicating a potential for compounding immune development effects on systemic metabolism (Appendix A, Supp. Figure 3).

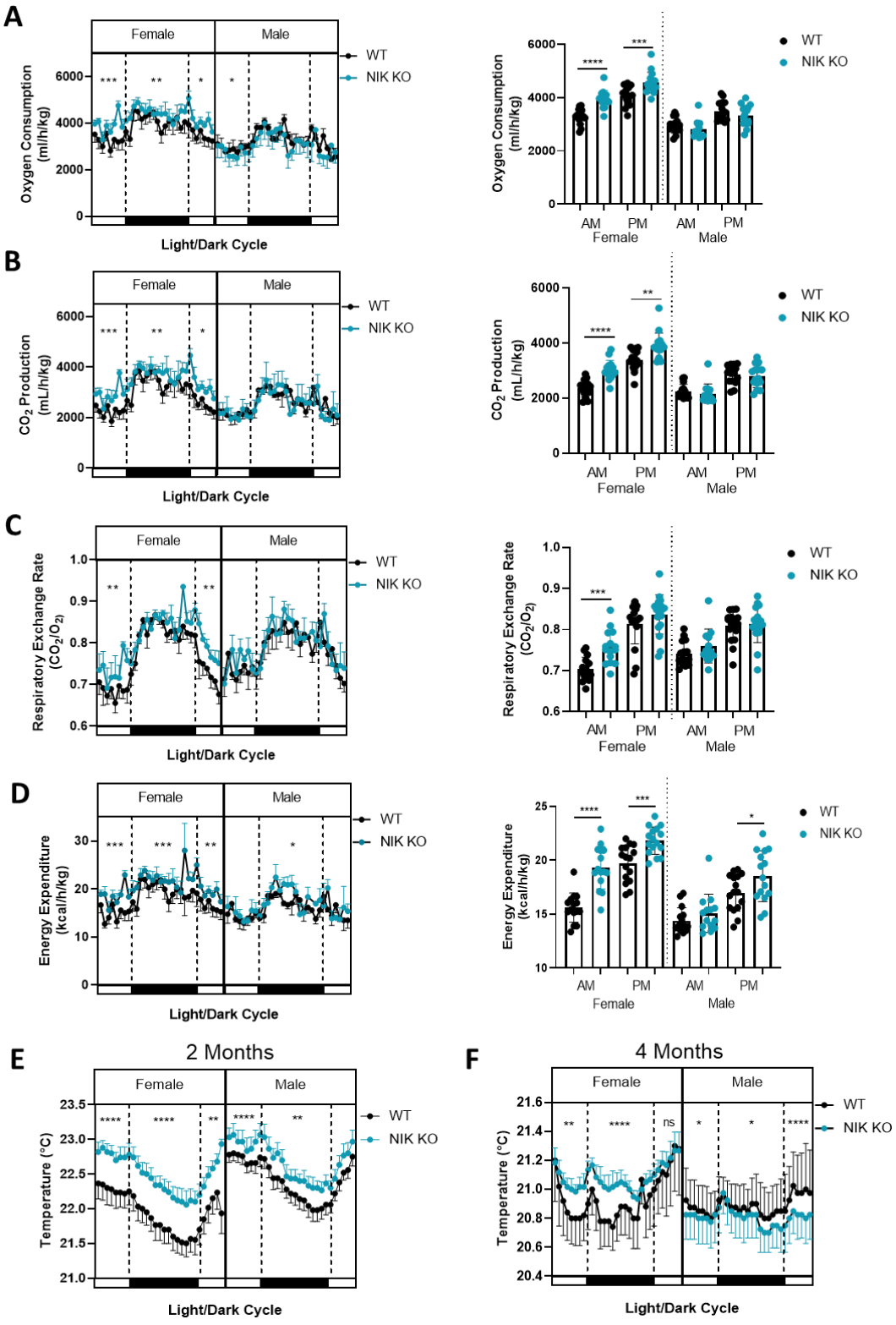

Figure 10: NIK KO Mice Exhibit Systemic Sex Specific Metabolic Differences

Figure 10: NIK KO Mice Exhibit Systemic Sex Specific Metabolic Differences

(A-D) Data collected from 4-month-old male and female *Map3k14* mice individually housed in metabolic cages (Females WT n=5, NIK KO n=6; Males WT n=4, NIK KO n=4). Morning and night analysis from a 24-hour time period of **(A)** oxygen consumption, **(B)** CO_2 production, **(C)** respiratory exchange rate (CO_2/ O_2), and **(D)** caloric energy expenditure **(E)** cage temperature with mice at 2 months of age (Females WT n=6, NIK KO n=5, Males WT n=5, NIK KO n=3) and at **(F)** 4 months of age. Line graphs represented as mean ± SEM, bar graphs represented as mean ± SD.

A Role for Noncanonical NF-κB-Dependent Signaling in Promoting Adiposity

Given that the reduction in NIK KO adipose tissue was due to a reduction in adipocyte size and number, we utilized C3H10T1/2 and 3T3-L1 cells to investigate changes in adipogenic potential with the loss of NIK. Strikingly, NIK KO cells were severely impaired in their ability to form mature adipocytes, as demonstrated by staining of lipid droplets that form in mature adipocytes. Ectopic expression of a wild-type human NIK construct in NIK KO cells (NIK KO-hNIK) restored adipogenesis to the same extent as control cells, confirming the crucial role of NIK in adipocyte development (Figure 11A, Figure 12A,B). Importantly, primary bone marrow-derived stem cells isolated from NIK KO mice were also impaired in their ability to differentiate into mature adipocytes compared to MSCs isolated from WT mice (Figure 12C). Furthermore, treatment of WT cells with a NIK specific inhibitor, B022[110], impeded adipocyte differentiation similar to cells lacking NIK (Figure 12D,E).

To evaluate if the effects the loss of NIK had on adipogenesis were dependent on NF-κB, we analyzed adipogenic differentiation of 3T3-L1 cells with genetic modifications of NF-κB proteins. RelB KO cells mimicked NIK KO cells and exhibited impaired adipocyte differentiation. Moreover, overexpression of IKKα and RelB in NIK KO cells (NIK KO-IKKα, NIK KO-RelB) substantially rescued adipocyte differentiation similar to the re-expression of NIK (NIK KO-hNIK). In contrast, overexpression of RelA, a canonical NF-κB transcription factor, in NIK KO or RelB KO cells was unable to restore adipocyte differentiation, and the loss of RelA did not impair adipogenesis (Figure 11B, Figure 13A). In addition to the observed effects of altered NF-κB expression on adipogenesis, immunoblot assays further demonstrated that transcription factor activation and induction

of the canonical NF-κB pathway (p-RelA-S536) decreased significantly by 4-6 days after induction of adipocyte differentiation. Conversely, expression of the noncanonical NF-κB protein RelB, increased throughout adipocyte differentiation (Figure 13B). Furthermore, activation of the canonical NF-κB pathway with TNFα inhibited adipocyte differentiation in WT C3H10T1/2 cells, whereas preferential activation of the noncanonical NF-κB pathway with TWEAK did not inhibit adipogenesis (Figure 13C,D). These findings indicate that NIK promotes adipocyte differentiation through the noncanonical NF-κB pathway, while the canonical NF-κB pathway maintains an inhibitory effect.

Interestingly, NIK and RelB were required for the induction of the essential adipogenic transcription factors PPARγ and one of its targets, C/EBPα 38 (Figure 11C, Figure 13E). Ectopic expression of NIK or RelB rescued the ability of NIK KO cells to respond to the PPARγ agonist ETYA (eicosatetraynoic acid), and increased PPARγ and C/EBPα expression (Figure 11D, Figure 13F). PPARγ was also observed to be decreased in NIK KO liver extracts (Figure 13G). In addition to lower expression of PPARγ, expression of the PPARγ-regulated, adipocyte-specific genes adiponectin (ADIPOQ), glucose transporter 4 (GLUT4, SLC2A4), and glycerol-3-phosphate dehydrogenase (GPD1), were significantly impaired in NIK KO and RelB KO cells even when treated with a PPARγ agonist. The ability of these cells to induce PPARγ activity and increase adipogenic genes to form functional adipocytes was restored by re-expression of NIK or RelB (Figure 11E). Additionally, the overexpression of PPARγ or C/EBPα rescued adipocyte differentiation in NIK KO C3H10T1/2 and 3T3-L1 cells, further demonstrating that the deficiency for NIK KO cells to undergo adipogenesis lies in their inability to increase levels of these key adipogenic transcription factors (Figure 11F). These data

suggest that NIK and the noncanonical NF-κB pathway are required for regulating the expression and activity of PPARγ and C/EBPα to promote adipogenesis.

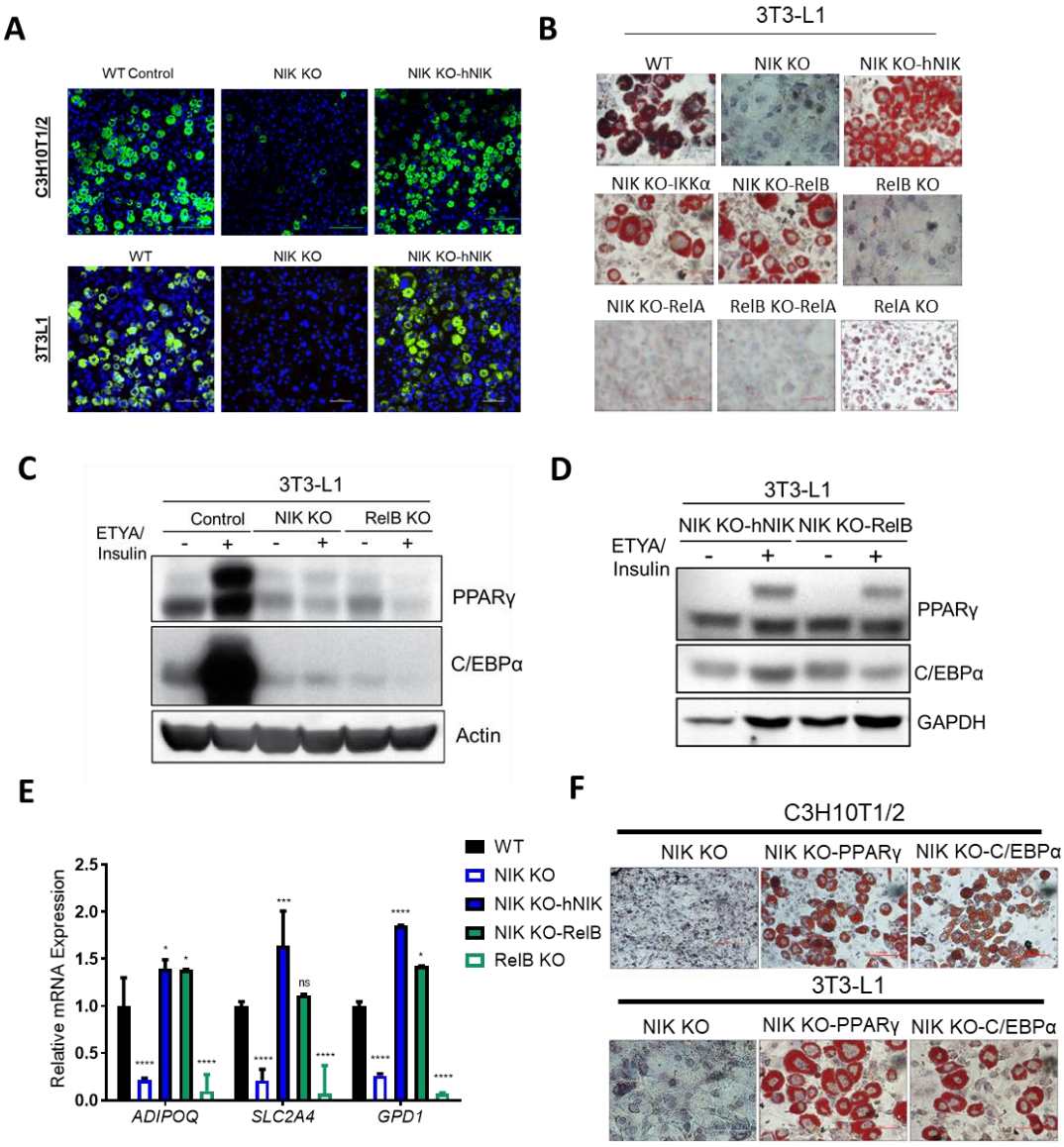

Figure 11: A Role for Noncanonical NF-κB-Dependent Signaling in Promoting Adiposity

Figure 11: A Role for Noncanonical NF-κB-Dependent Signaling in Promoting Adiposity

(A) Fluorescent BODIPY lipid staining of C3H10T1/2 and 3T3-L1 cells showing a significant reduction in adipogenesis with the loss of NIK which is rescued in NIK KO-hNIK cells (representative imaging from n=+3 biological replicates). **(B)** Oil Red O staining of differentiated 3T3-L1 cells lacking or over expressing various noncanonical/canonical NF-κB proteins (representative imaging from n=+3 biological replicates). **(C)** PPARγ and C/EBPα expression in undifferentiated vs adipogenic treated in NIK KO and RelB KO 3T3-L1 cells compared to WT control cells. **(D)** PPARγ and C/EBPα expression in undifferentiated vs adipogenic treated 3T3-L1 cells with re-expression of human NIK or overexpression of RelB in NIK KO cells (NIK KO-hNIK, NIK KO-RelB). **(E)** qPCR analysis of adipocyte genes (*ADIPOQ, SLC2A4, GPD1*) in ETYA/insulin treated C3H10T1/2 cells. Data represented as mean ± SD, Tukey's Multiple Comparison Test (n=3). **(F)** Oil Red O staining of differentiated NIK KO or NIK KO with overexpression of PPARγ or C/EBPα in C3H10T1/2 and 3T3-L1 cells.

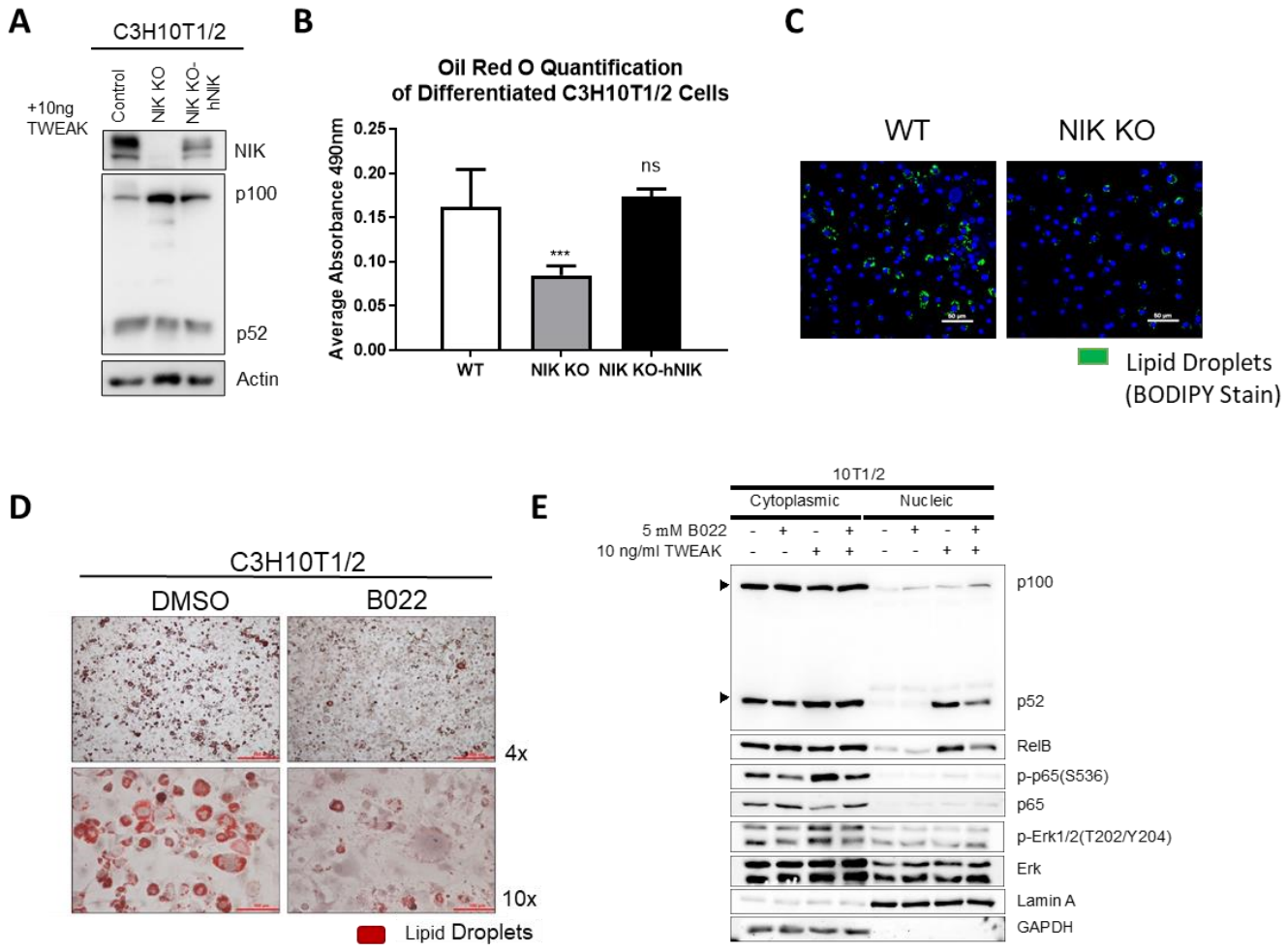

Figure 12: NIK Inhibition Perturbs Adipogenesis

Figure 12: NIK Inhibition Perturbs Adipogenesis

(A) Immuno-blot of C3H10T1/2 cells confirming the loss of NIK (NIK KO) and the rescue of noncanonical NF-κB functionality (p100-p52 processing) with ectopic expression of human NIK (NIK KO-hNIK). **(B)** Quantification of oil red o staining of differentiated C3H10T1/2 cells. Data represented from n=3 independent experiments, as mean ± SD, * p≤.05, ** p ≤.01, *** p ≤.001, **** p ≤.0001, Tukey's Multiple Comparison Test. **(C)** Adipocyte differentiation of primary bone marrow cells from WT and NIK KO mice stained with BODIPY (lipid droplets; green) and Hoechst (blue). **(D)** C3H10T1/2 cells treated with DMSO or the NIK inhibitor (B022), induced for adipocyte differentiation, and then stained with Oil Red O. **(E)** Cytoplasmic/ nuclear fractionation of C3H10T1/2 cells treated with B022 (NIK inhibitor) or TWEAK (activator of the noncanonical NF-κB pathway), showing inhibition of p100-p52 processing (induction of noncanonical protein processing by NIK) with B022 treatment.

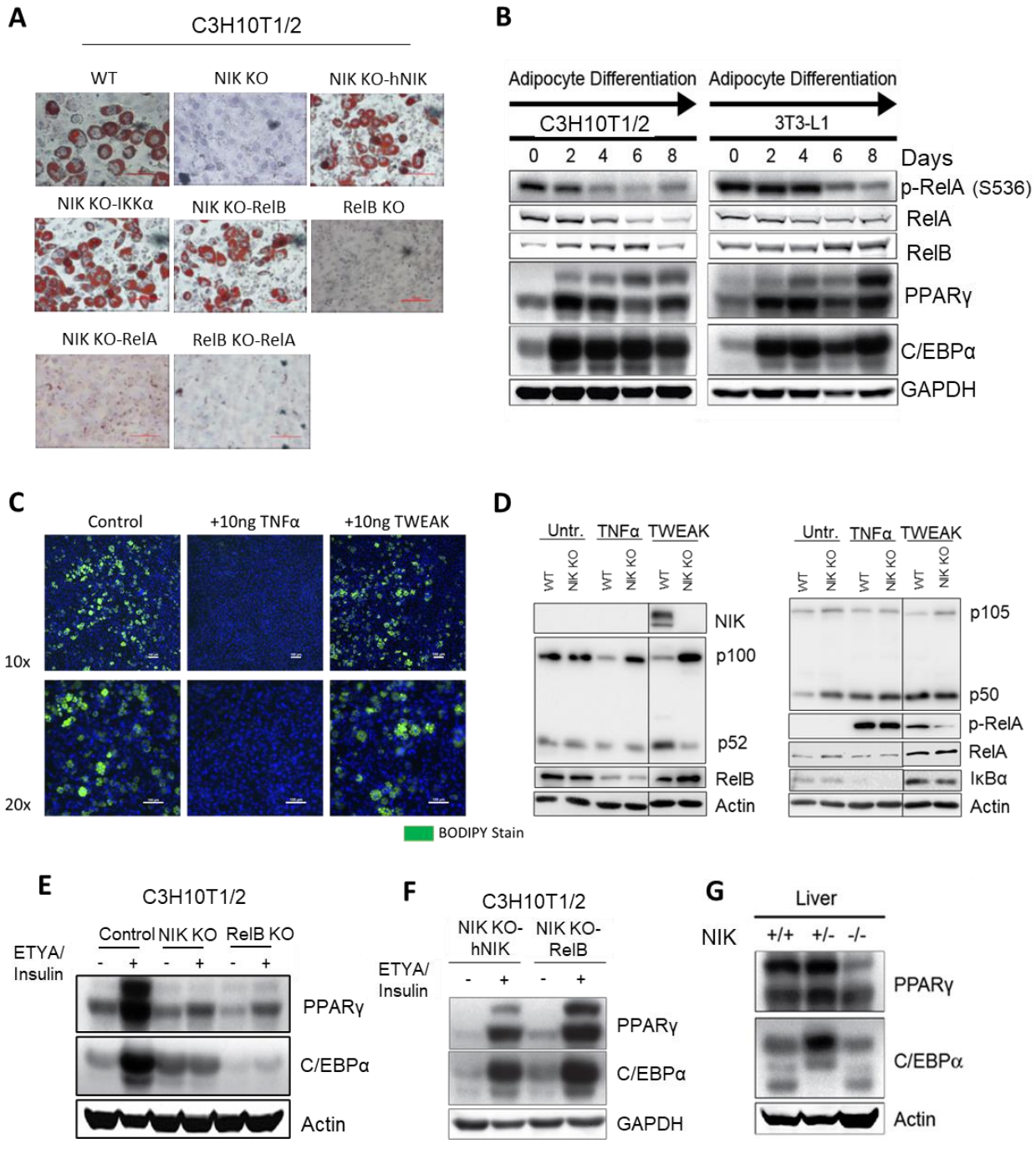

Figure 13: NF-κB Pathway Influences on Adipogenesis

Figure 13: NF-κB Pathway Influences on Adipogenesis

(A) Oil Red O staining of C3H10T1/2 cells after induction of adipocyte differentiation with ETYA and insulin (representative imaging from n=+3 biological replicates). **(B)** Immunoblot of adipocyte induction in C3H10T1/2 and 3T3-L1 cells with ETYA/Insulin(representative of n=3 independent experiments). **(C)** BODIPY staining of lipid droplets (green) and Hoechst staining (blue) in differentiated C3H10T1/2 treated with TNFα (tumor necrosis factor alpha; activator of canonical NF-κB pathway) or TWEAK (tumor necrosis weak life factor; activator of noncanonical NF-κB pathway). Representative image of n=3 independent experiments. **(D)** Immunoblots confirming activation of the noncanonical or canonical NF-κB pathway after induction with TWEAK or TNFα, respectively. Immunoblot of transcriptional activators of adipogenesis, PPARγ and C/EBPα expression in undifferentiated and differentiated **(E)** NIK KO, RelB KO, **(F)** NIK KO-hNIK and NIK KO-RelB C3H10T1/2 cells, **(G)** and mouse liver samples.

NIK Regulates Susceptibility to Diet-Induced Obesity

Having observed the effects of NIK on adiposity, metabolism, and adipogenesis we next sought to investigate if NIK played a role in adipose tissue expansion in response to a high-fat diet (HFD). After 2-3 months on a HFD both male and female NIK KO mice showed significantly less weight gain than their wild-type counterparts (Figure 14A,B). Specifically, NIK KO mice exhibited a 50% decrease in gWAT tissue compared to mice (Figure 14C). Under a HFD male and female NIK KO mice also displayed a reduction in the subcutaneous depot (ingWAT) compared to WT littermates (Figure 6D). In addition to a significant reduction in fat mass, *ex vivo* analysis of gonadal adipose tissue revealed that similar to mice on a chow diet, NIK KO mice on a HFD exhibited smaller adipocytes (Figure 14E, F). However, the decrease in adipocyte size was to a lesser extent than the overall reduction in gWAT mass, which was confirmed after comparing the ratio (noted on figure) between WT and NIK KO in the reduction of adipose mass and the ratio reduction in adipocyte size (Figure 14F, G). Therefore, the reduction in NIK KO adipose tissue is likely due to a decrease in both adipocyte size and number. Whole body composition analysis demonstrated that on a HFD, NIK KO mice maintained a lower fat mass overall and a higher lean mass ratio by body weight compared to WT mice (Figure 14H). Notably, NIK KO mice gained about 3x less fat than WT mice on a HFD compared with standard chow (Figure 14I). In addition to maintaining a reduction in adiposity, glucose tolerance testing demonstrated that NIK KO mice were more efficient at clearing glucose than WT littermates, suggesting an increase in insulin sensitivity (Figure 14J). This was confirmed with insulin tolerance testing where NIK KO mice cleared glucose more rapidly than WT mice after an administration of insulin (Figure 14K).

Similar to mice on a chow diet, NIK KO mice on a HFD exhibited higher metabolic activity with increases in basal OCR, ECAR and ATP production as analyzed by extracellular flux assays. In addition, NIK KO on a HFD still exhibited deficiencies in SRC and a heightened proton leak. One observed difference between HFD and chow mice is significant differences in glycolysis are only observable in ingWAT versus gWAT (Figure 15A,B). Though mitochondrial ATP was significantly increased in both gWAT and ingWAT of NIK KO mice, overall ATP was not significantly increased in the adipose tissue of HFD mice (Figure 16A). Similar to the increase in glycolysis, gWAT from NIK KO mice on a HFD exhibited a significant increase in glucose uptake, as well as a significant increase in lipolysis ability (Figure 16B,C).

Analysis of adipogenic genes from the inguinal WAT of HFD mice also revealed a reduction in fatty acid binding protein 4 (*FABP4*; Ap2), and an increase in GLUT4 and *GPD1* (Figure 17A,B). Increased GLUT4 gene expression complements both an increase in glucose clearance of NIK KO mice and higher glycolytic demands of NIK KO adipose tissue. Further evidence supports the uptake of glucose by the whole mouse to fuel glycolytic demands as gene expression for glycogen synthase is significantly down regulated in NIK KO livers and thus glucose is not being stored (Figure 17C,D). Reduction in lipid storage of NIK KO adipocytes does not seem to be associated with adipocyte dysfunction as NIK KO mice do not have exogenous lipid storage in their livers even on a HFD as seen by Oil Red O staining which is accompanied by lower gene expression of fatty acid binding protein (*FABP1*) and fatty acid oxidation genes (*MCAD, CPT1α*) (Figure 17D,E). Overall, the data show NIK has a previously unrecognized role in mediation of

adipocyte development and adipose expansion, with its inhibition acting as a preventative of metabolic disorders including diet-induced obesity and diabetes.

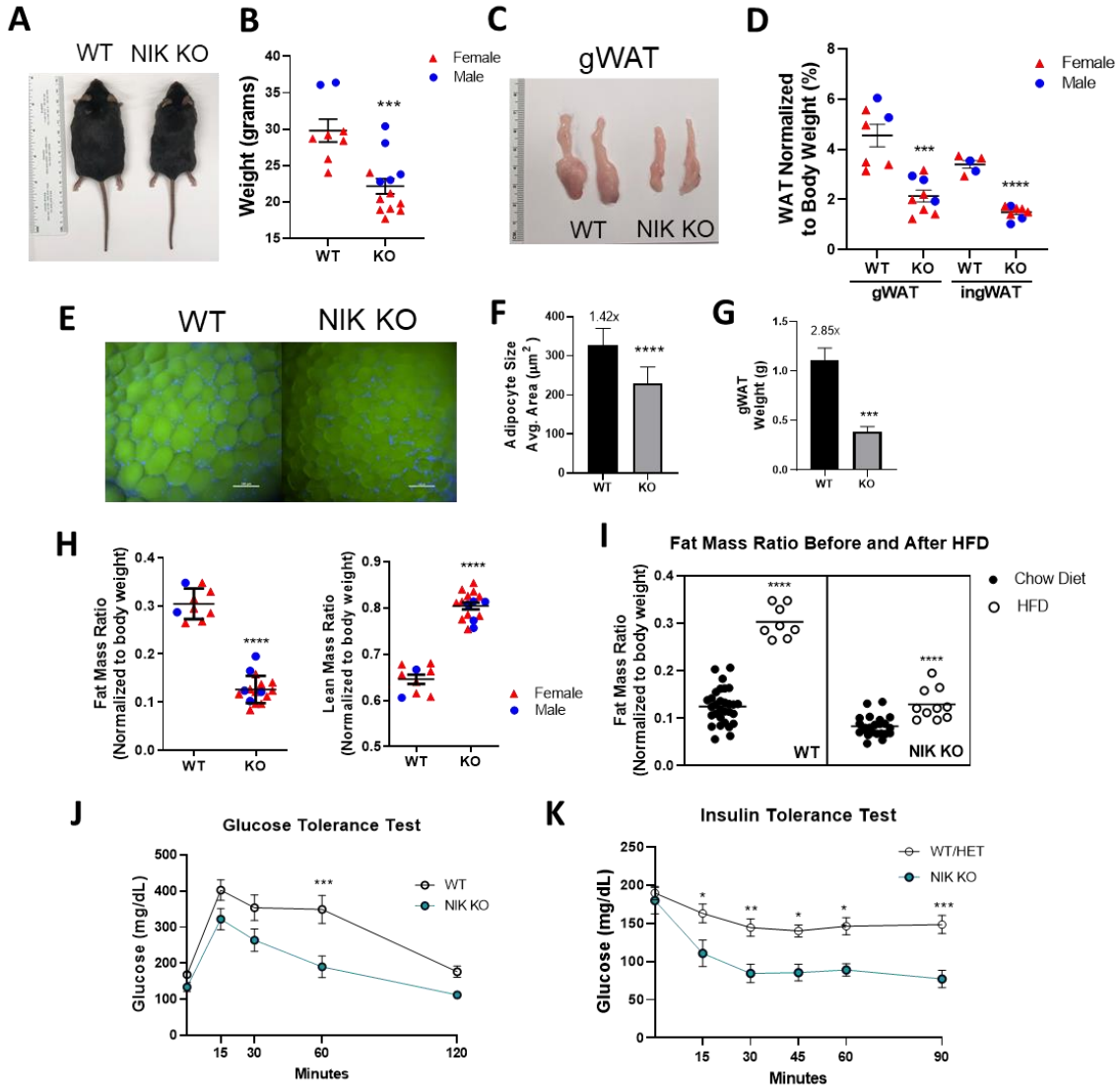

Figure 14: NIK Regulates Susceptibility to Diet-Induced Obesity

Figure 14: NIK Regulates Susceptibility to Diet-Induced Obesity

(A) Images of male WT and NIK KO mice on HFD. **(B)** Weights of WT and NIK KO male and female mice exposed to a HFD for about 3 months (mice exposed to a HFD in utero up until weaning and then 8-10 weeks after weaning). Data represented as mean ± SEM, Unpaired Student t-test. **(C)** Gonadal white adipose tissue from male mice on a HFD. **(D)** Weights of gonadal and inguinal white adipose tissue from male and female mice normalized to body weight. Data represented as mean ± SEM, Unpaired Student t-test. **(E)** Whole mount staining of gonadal white adipose tissue from WT and NIK KO female mice on a HFD with BODIPY (green) and Hoechst (blue). **(F)** Image J quantification of adipocyte size from female mice on a HFD for about 10 weeks. Data represented as mean ± SD, WT n=100 cells from 5 different images across 3 different mice and NIK KO n=120 cells from 6 different images across 3 different mice. **(G)** Weights of gonadal adipose tissue from female WT and NIK KO mice on HFD. **(H)** EchoMRITM data of fat and lean mass from female and male WT and NIK KO mice on a HFD normalized to weight. Data represented as mean ± SEM, Unpaired Student t-test. **(I)** Fat mass data from EchoMRITM analysis comparing fat mass ratios from a chow diet to a HFD between WT and NIK KO mice. **(J)** Glucose tolerance test on WT and NIK KO mice on a HFD. Data represented at mean ± SEM, Sidak's Multiple Comparisons Test. WT n=8, NIK KO n=12. **(K)** Insulin tolerance test on WT, HET and NIK KO mice on a HFD. Data represented at mean ± SEM, Sidak's Multiple Comparisons Test. WT/HET n=10, NIK KO n=6.

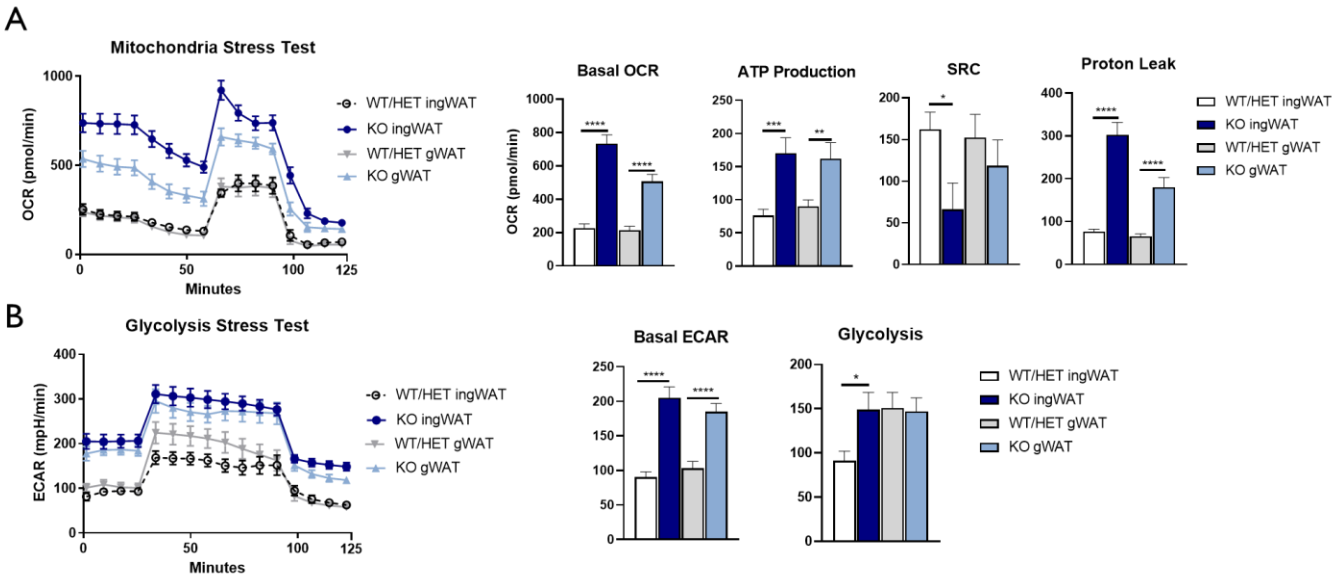

Figure 15:NIK KO Mice on a HFD Maintain Higher Metabolic Activity in Adipose Tissue

(A) Mitochondria stress test done by extracellular flux analysis of oxygen consumption rates (OCR). Subcutaneous inguinal WAT (ingWAT) and visceral gonadal WAT (gWAT) were compared between WT/HET (n=2WT, 1HET) and NIK KO (n=3) mice (all females, with n=8 technical replicates per mouse). Basal OCR, ATP production, Spare respiratory capacity (SRC), and Proton leak were analyzed from the assay. **(B)** Glycolysis stress test done by extracellular flux analysis of the pH to measure extracellular acidification rate (ECAR). IngWAT and gWAT from same mice were analyzed and basal ECAR and glycolysis rates were analyzed from the assay.

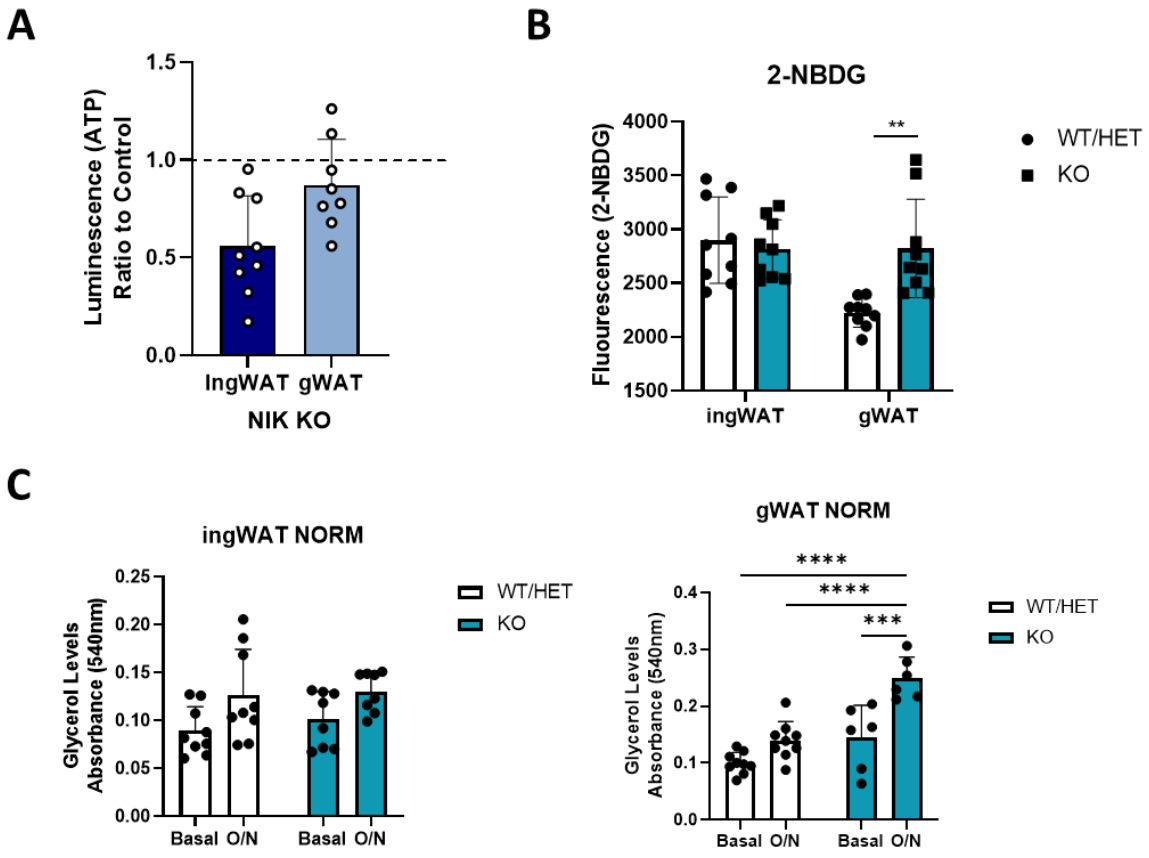

Figure 16: NIK KO Visceral WAT Has Higher Glucose Uptake and Lipolysis

(A) Total ATP, from ATPlite, measurement from same mice measuring between ingWAT and gWAT. **(B)** 2-NBDG, fluorescent glucose, uptake assay between WT/Het (n=2WT/1HET) and NIK KO (n=3) ingWAT ang gWAT (all females). **(C)** ingWAT and gWAT from same mice stimulated with isoproterenol to induce lipolysis.

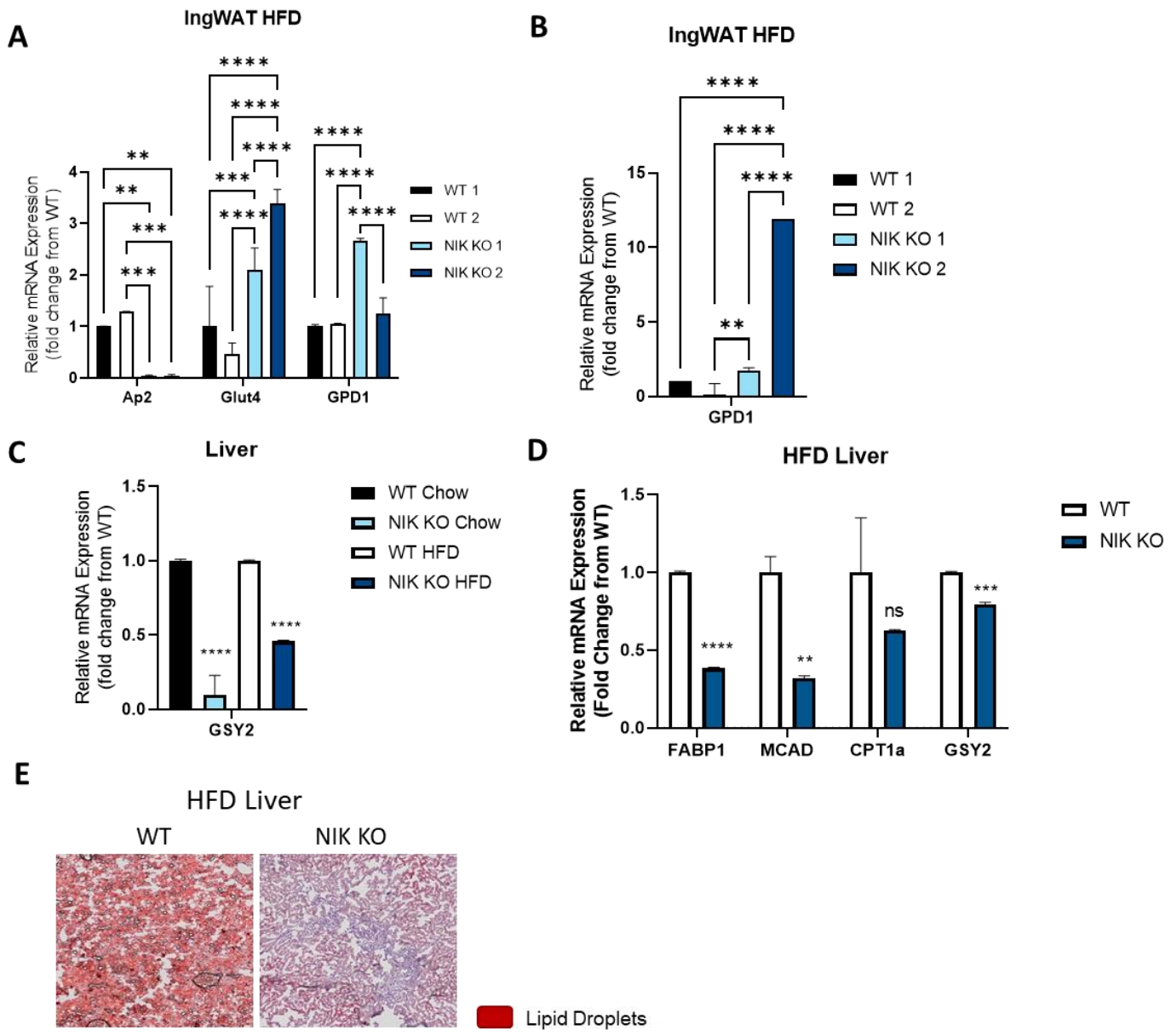

Figure 17: Map3k14 Adipose and Liver Functionality on a HFD

Figure 17: *Map3k14* Adipose and Liver Functionality on a HFD

(A) qPCR analysis of adipocyte genes Ap2 (adipocyte specific protein 2; FABP4), GLUT4 (glucose transporter 4, SLC2A4), GPD1 (glucose-3-phosphate dehydrogenase 1) of inguinal WAT from male HFD mice (WT/ NIK KO n=2 each). **(B)** GPD1 mRNA analysis of inguinal WAT from HFD female mice (WT/ NIK KO n=2 each). **(C)** GSY2 (glycogen synthase 2) relative mRNA expression from chow and HFD liver samples (WT/ NIK KO n=2 females). **(D)** qPCR analysis of fatty acid oxidation genes (FAB1; fatty acid binding protein, MCAD; medium chain acyl-CoA dehydrogenase, CPT1α; carnitine protein transferase) and glycogen synthase 2 from HFD female liver samples (N=2 biological replicates ran in triplicate). **(A-D)** Data represented as mean ± SD, Unpaired Student t-test. **(E)** Oil Red O and hematoxylin staining for lipid accumulation in liver samples of HFD mice.

Discussion

Maintenance of energy balance is critical for the normal function of physiological processes and is a potent indicator of health status. In this study, we demonstrate for the first time that mice lacking NIK exhibit higher metabolic output and energy expenditure resulting in decreased adiposity and increased resistance to obesity. NIK KO mice maintained a leaner deposition, even under a high-fat diet, despite their decreased physical activity and increased eating (see Figs. 1 & 6 and Supp. Figs. 2 & 3). Consistent with these *in vivo* findings, *in vitro* and *ex vivo* analysis revealed that aerobic respiration and glycolysis are elevated in NIK KO preadipocytes and adipose tissue. However, NIK KO preadipocytes and tissue also exhibited significantly impaired spare respiratory capacity and elevated proton leak, suggesting that in the absence of NIK, mitochondria work at higher, but inefficient, metabolic rates while triggering a compensatory upregulation of glycolysis (see Figs. 2 & 3). This compensatory upregulation of aerobic glycolysis has parallels to the Warburg effect in cancer cells[111], which has been hypothesized facilitate rapid generation of ATP using glucose as carbon source for anabolic pathways, while controlling ROS production and redox homeostasis [112].

While NIK KO mice overall exhibited a reduced adipose phenotype and *in vitro* and *ex vivo* data demonstrated changes in metabolic demands with the loss of NIK, only females exhibited whole body metabolic changes, including increased energy expenditure and temperature (see Fig. 4). Observed elevated thermogenesis may be a result of increased mitochondria proton uncoupling which is consistent with the higher proton leak observed in NIK KO cells. Increased proton uncoupling is highly associated with brown adipose tissue where there is an increased expression of uncoupling protein

1 (UCP1) that is utilized for increased thermogenesis. Changes in overall temperature and increased proton leak in the adipose tissue could imply a role for NIK in he development and function of brown adipose tissue or in the formation of beige adipocytes (browning in white adipose tissue) [113].

These sex differences could also be attributed to distinct metabolic or immune changes between genders. For example, although females are more apt to adipose deposition than males, estrogen increases insulin sensitivity and protects female mice from diet-induced obesity [114–116]. Furthermore, there are known sex differences in the development and function of immunity between genders that could have systemic metabolic effects [117]. In this context, ablation of NIK increases susceptibility to viral and bacterial infections, consistent with well-established roles for NIK in regulating immunity[94,98]. Changes in bacterial flora or viral infection have been shown to alter host metabolism in order to support replication [118,119]. Furthermore, as a regulator of immune cell development, the loss of NIK can have effects on the metabolic status and recruitment of adipose tissue immune cells that can play critical roles in regulating tissue homeostasis. Nevertheless, we note that *in vitro* differentiated pre-adipocytes exhibited metabolic phenotypes similar to *ex vivo* adipose tissue (see Figs. 2 & 3), demonstrating that NIK has adipose cell-intrinsic metabolic functions. Use of a systemic knockout mouse model provided insight into the metabolic ramifications associated with NIK loss-of-function immunodeficiency.

Our findings also revealed opposing effects of canonical and noncanonical NF-κB signaling in regulating adipogenesis (see Fig. 5 and Supp. Fig. 5). These observations are consistent with previous data showing that activation or overexpression of the

canonical NF-κB/RelA pathway inhibits adipogenesis, and that RelA itself is inhibited by adipogenic-promoting PPARγ agonists *in vitro* and *in vivo* [120,121]. Additionally, an increase of RelB and p52 during adipocyte differentiation was similarly seen in a separate study analyzing 3T3-L1 cells [122]. However, a cooperative role for the canonical and noncanonical NF-κB pathways in promoting adipocyte differentiation was previously reported in a study of adipose-specific RelB knockout mice in response to lymphotoxin-β-receptor (LTβR) activation [123]. Additionally, a separate study demonstrated that mice with adipose-specific knockout of Tank-binding kinase 1 (TBK1), a repressor of NIK stability, exhibited a slight reduction in adipose tissue and adipocyte size under a prolonged HFD, which was accompanied by increased noncanonical, as well as canonical NF-κB signaling, which were linked to hyper-inflammation [47]. Our results suggest that there are likely signal-specific roles for RelB in regulating PPARγ expression and adipogenesis. Moreover, NIK may have RelB-independent, or non-cell autonomous effects on adipogenesis and adipose development. In the context of these findings, the signals responsible for activating NIK during adipocyte development and expansion under a HFD warrant further study.

A key finding reported here is our observation that NIK KO mice displayed increased resistance to HFD-induced obesity by maintaining reduced weight and overall fat mass (see Fig. 6). This phenotype was accompanied by increased metabolic fitness seen in the NIK KO mice with greater insulin sensitivity and glucose clearance than WT mice. Our data are consistent with a previous report demonstrating that NIK activity is increased in the livers of genetic (*ob/ob)* or HFD-fed obese mice, and liver-specific loss of NIK increases glucose metabolism [103,104]. Finally, we have established that NIK KO

mice maintained smaller adipocytes even under a prolonged HFD (>1 month), and NIK KO primary mesenchymal stem cells exhibit reduced adipocyte differentiation (see Figs. 1 & 6 and Supp. Fig. 4). These results suggest that NIK mediates adipose hyperplasia as well as hypertrophy. Taken together, our data suggest that systemic NIK inhibition may have efficacy in treating or preventing metabolic syndrome caused by diet-induced obesity through inhibition of hyperglycemia, insulin resistance and adipose tissue expansion, as well as increased metabolic output and energy expenditure.

CHAPTER III

GLIOBLASTOMA TREATMENT WITH CYANINE CONJUGATED KINASE INHIBITORS*

Introduction

Glioblastoma multiforme (GBM) is a rare, malignant form of brain cancer that is characterized as a grade four glioma, or the most aggressive form of gliomas [124]. Outlook of GBM prognosis is bleak, with a median survival of 12.6 months and a 5 year survival rate of about 4-5% [125]. The main form of treatments for this deadly disease consists of traditional approaches including surgical resection, radiation, and chemotherapy most commonly with temozolomide (TMZ). Unfortunately even with use of conventional cancer treatments, prognosis remains grim [126].

Given the need to improve chemotherapeutics, not only for extremely aggressive cancers like GBM, but for other cancers as well, research has looked to the use of heptamethine cyanine dyes (HMCDs). HMCDs are near-infrared fluorescence (NIRF), cyanine-7 dyes that have been shown to not only target but also accumulate in solid tumors. More importantly these dyes preferentially localize to tumor sites over healthy

.

tissue [127–129]. Preferential uptake of HMCDs by tumor cells has been identified to be responsible due to organic anion-transporting polypeptides (OATPs). OATPs regulate cellular uptake of salts, bile acids, hormones, toxins, and drugs. It has been demonstrated that while OATPs are expressed on various cell types, cancers exhibit an increase in these transmembrane transporters [130]. The antitumor properties of HMCDs are not the only benefit of these dyes, due to their fluorescent properties they have been utilized in identification of tumors for resection before surgery, and tracing of chemotherapeutics [131,132]. Use of HMCDs in conjugation with FDA approved chemotherapeutics has been the focal point of certain cancer research areas, in order to improve drug delivery and efficacy of traditional cancer treatments, especially in regard to cancers that are resistant to conventional therapeutics. While a main drawback of using certain chemotherapeutics in treatment of GBM is their ability to cross the blood brain barrier (BBB), HMCDs have been shown to overcome this limitation [133,134].

Here we investigate the use of FDA approved chemotherapeutics such as Gemcitabine, Dasatinib, and Crizotinib in treatment of GBM. Gemcitabine is a deoxycytidine analog that incorporates into the DNA of replicating cells and slows or inhibits growth at the S phase [135,136]. Gemcitabine is approved for treatment of breast cancer, pancreatic cancer, non-small cell lung cancer, and bladder cancer [137]. Dasatinib is a tyrosine kinase inhibitor that preferentially targets Src kinases with approved treatment for chronic myeloid leukemia (CML) and acute lymphoblastic leukemia (ALL) [138,139]. The final chemotherapeutic used in this study was another tyrosine kinase inhibitor, Crizotinib, which targets anaplastic lymphoma kinase (ALK). Though Crizotinib can also inhibit *MET* (Mesenchymal-epithelial transition), *ROS1* (ROS proto-oncogene 1), and

other tyrosine growth receptors, it has been shown to have efficacy in treating *ALK*+ non-small cell lung cancers [140].

Other studies have investigated the use of these chemotherapeutics in treatment of GBM and have found promising results in efficacy of these drugs against GBM. Gemcitabine was investigated for GBM treatment since 1999, and while it was found to have efficacy against GBM in vitro, clinical trials with the use of gemcitabine failed to pass phase II [141]. Both Crizotinib and Dasatinib have been shown to reduce migration and invasion of GBM cells [142]. Dasatinib alone or in combination with another chemotherapeutic was shown to have efficacy on intracranial mouse GBMs that were generated by intrauterine electroporation of plasmids with TP53, PDGFRA, and H3K27M mutations [143]. Other studies have also highlighted the potential of Crizotinib as a treatment for GBM. One study investigated the heterogeneity of glioblastoma stem cells (GSCs) and found increased expression of ALK, ROS1, and MET in various cell lines, hypothesized to regulate cell stemness. Given the expression of these various proteins, Crizotinib was proposed as an ideal therapeutic to target GSCs [144]. Indeed, a later study demonstrated that Crizotinib alone and in combination with other chemotherapeutics, inhibited neurosphere formation, a phenotype of stemness in cancer cells, of patient derived GBM cells with high expression of c-MET and EGFR [145]. While past clinical trials have proven Dasatinib as unsuccessful for GBM treatment alone, current trials are looking at combination therapies. In addition Crizotinib is undergoing phase I clinical trials for GBM treatment (NCT02270034) [146,147]. Given the potential of these chemotherapeutics to also treat GBM, improvement of efficacy is sought by conjugating these drugs to a

heptamethine cyanine dye to increase penetration of the blood brain barrier and utilize the tumor targeting benefits of the dye.

Results

Gemcitabine

Conjugation of a heptamethine dye, specifically MHI-148, to Gemcitabine (Gem) was generated by binding of the parent drug to the meso-chloride of the dye (Cy-Gem) (Appendix B Supp. Figure 8). Utilization of this binding strategy inhibited binding of the dye to albumin, increasing clearance time and limiting targeting to healthy tissue [148]. To investigate efficacy of Cy-Gem *in vivo* on GBM, we utilized a xenograft model with human U87 GBM cells expressing red fluorescence protein (RFP) and luciferase (Luc) (U87-RFP-LUC), subcutaneously injected into the flank of immunocompromised mice. Efficacy of Cy-Gem was compared to tumors treated with either vehicle or Gemcitabine alone after weekly IV injections (10mg/kg). Drug localization and clearance was monitored by the far red fluorescence of the dye. Tumor progression was monitored weekly by luminescence and by physical caliper measurements. After 5 weeks of treatment Cy-Gem tumor growth was less than vehicle and comparable to that of Gemcitabine alone (Figure 18 A-C). More importantly, the efficacy of Cy-Gem was achieved at a third of that Gemcitabine alone due to differences in molecular weight. In monitoring drug localization and clearance of Cy-Gem by fluorescence, we observed that the conjugated compound localized to the tumor site and the liver for metabolization. Cy-Gem was actively cleared and was mostly cleared from the mouse by one week (Figure 19 A,B). Localization and clearance of Cy-

Gem was further validated by postmortem analysis of mice after an IV injection. Fluorescence analysis showed compound throughout the circulatory system of the mouse with accumulation at the tumor site, liver, and kidneys (Figure 20 A,B). Furthermore, monitoring of mouse weights showed no significant reduction between treatments and control indicating no deleterious effects of the parent drug or cyanine conjugated drug on the overall health status of the mice (Appendix B Supp. Figure 9). Overall, conjugation of Gemcitabine to a cyanine dye not only improved compound tracing, but tumor targeting and efficacy at a third of the parent drug.

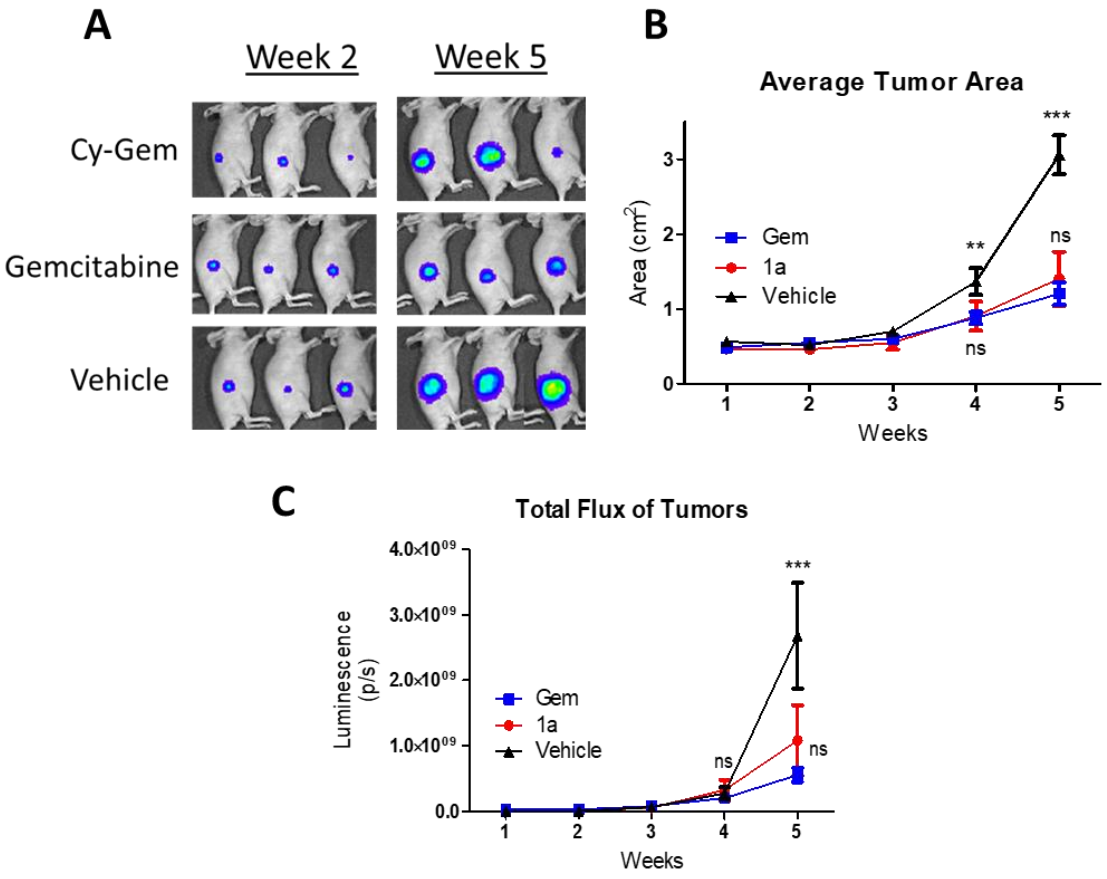

Figure 18: Therapeutic Effect of Cy-Gemcitabine

Figure 18: Therapeutic Effect of Cy-Gemcitabine

(A) Luminescence images acquired with an IVIS Spectrum in vivo imaging system (Perkin Elmer). **(B)** Mean tumor size (cm^2) with SEM over a 5 week period post drug administration (n=3). Two-way ANOVA with Bonferroni posttest shows statistically significant differences between Cy-Gem (1a) or unconjugated Gemcitabine (Gem) compared with vehicle control group at 4 weeks (**p<0.01) and 5 weeks (***p<0.001). **(C)** Mean tumor luminescence (photons per second, p/s) with SEM over a week period (n=3). Two-way ANOVA with Bonferroni posttest shows statistically significant differences between Cy-Gem (1a) or Gem and the vehicle group at 5 weeks (p<0.001)**.** Reprinted with permission from “Cyanine-Gemcitabine Conjugates as Targeted Theranostics Agents for Glioblastoma Tumor Cells” by Jiang *et al*., 2019, *J. Med. Chem*., 62, 20, 9236–9245. Copyright 2019 American Chemical Society.

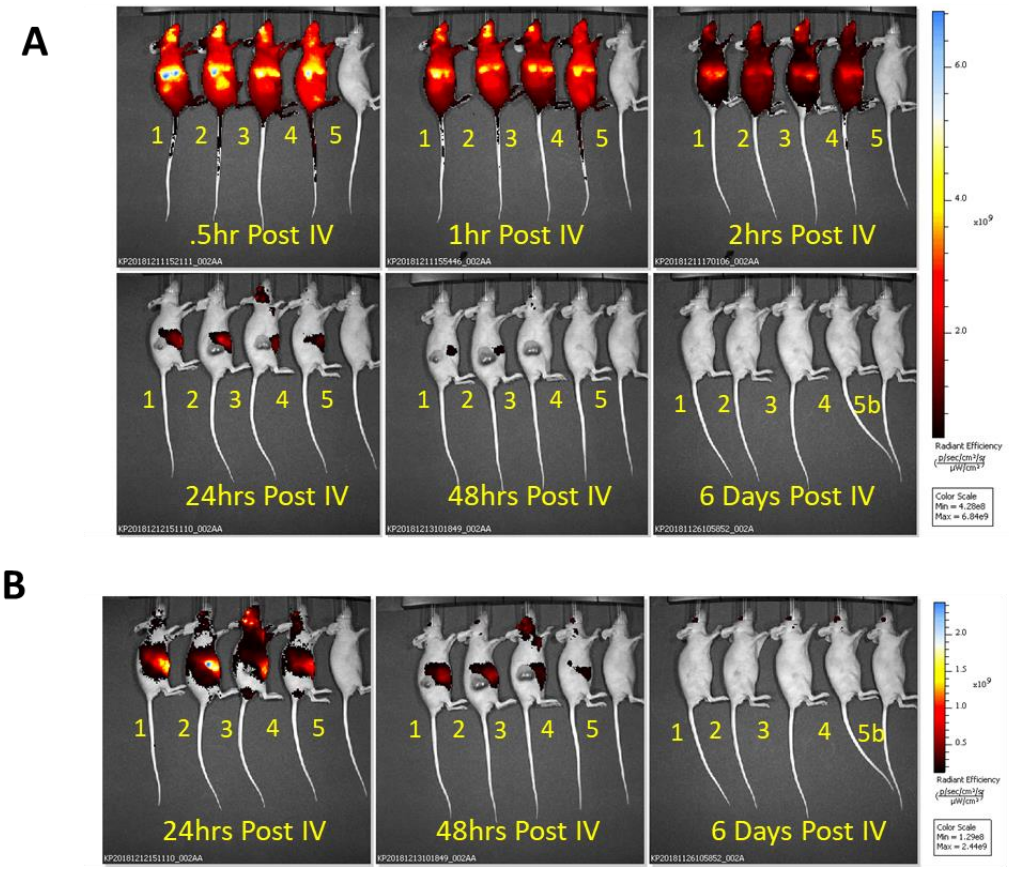

Figure19: Cy-Gemcitabine Localization and Clearance in vivo

(A) Mice were injected with 10mg/Kg Cy-Gemcitabine (mice 1-4; same throughout time course) with an uninjected control (mouse 5). Images were taken at half hour, 1 hour, 2 hours, 24 hours, 48 hours, and 144 hours/6 days after intravenous injection. Mouse 5b was also injected with Cy-Gemcitabine. Fluorescence intensities of all images normalized and represented on the same scale. **(B)** Fluorescence of Cy-Gemcitabine mice normalized at 24hrs, 48hrs, and day 6 are shown at 10x lower scale to show residual drug localization *in vivo***.** Reprinted with permission from "Cyanine-Gemcitabine Conjugates as Targeted Theranostics Agents for Glioblastoma Tumor Cells" by Jiang *et al*., 2019, *J. Med. Chem*., 62, 20, 9236–9245. Copyright 2019 American Chemical Society.

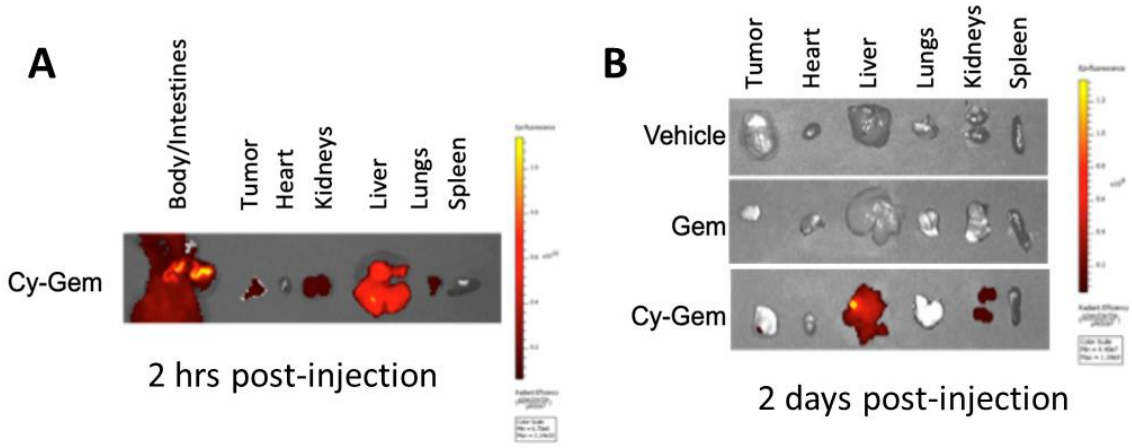

Figure 20: Cy-Gemcitabine Localization with Postmortem Analysis

(A) Fluorescence imaging was performed on the indicated tissues, which were dissected 2 hours after intravenous injection of Cy-Gemcitabine**. (B)** Comparison of fluorescence signal in indicated tissues from vehicle, Gem and Cy-Gem-injected mice 2 days after intravenous injection. Reprinted with permission from “Cyanine-Gemcitabine Conjugates as Targeted Theranostics Agents for Glioblastoma Tumor Cells” by Jiang *et al*., 2019, *J. Med. Chem*., 62, 20, 9236–9245. Copyright 2019 American Chemical Society.

Dasatinib

Also under investigation to improve efficacy for GBM treatment is the tyrosine kinase inhibitor, Dasatinib, that preferentially targets Src family kinases. This FDA approved compound is used to treat leukemias including CML and ALL. Dasatinib was also conjugated to the heptamethine cyanine dye, MHI-148, but at the end of the cyanine dye replacing a hydroxy group versus at the meso-chloride as with Gemcitabine (Appendix B, Supp. Figure 10). For tumor engraftment, mouse GBM, U87-RFP-LUC cells were also injected subcutaneously into the flank of immunocompromised mice. Cy-Das injections were compared to that of a DMSO control as the vehicle. Tracing of Cy-Das by far red fluorescence from the dye demonstrated preferential tumor targeting over healthy tissue. Unlike Cy-Gem, penetration and accumulation of Cy-Das persisted for several days after injection (Figure 21 A-C). Tumor targeting of Cy-Das was further verified after postmortem analysis which also demonstrated preferential accumulation of Cy-Das at the tumor site over healthy tissue such as in the liver or kidneys (Figure 21 D-G). RFP expression of GBM cells allowed for visualization of tumors and monitoring of their growth. After incremental compound injections, it was observed that Cy-Das had modest efficacy on perturbing GBM growth (Figure 22A). Tumor response to the chemotherapeutic was variable and may be dependent on the starting size of tumors. Overall, conjugation of Dasatinib to a cyanine dye not only allowed compound tracing but proved preferential tumor targeting. Further optimization of compound dosage, route and frequency of administration will be needed to enhance GBM efficacy.

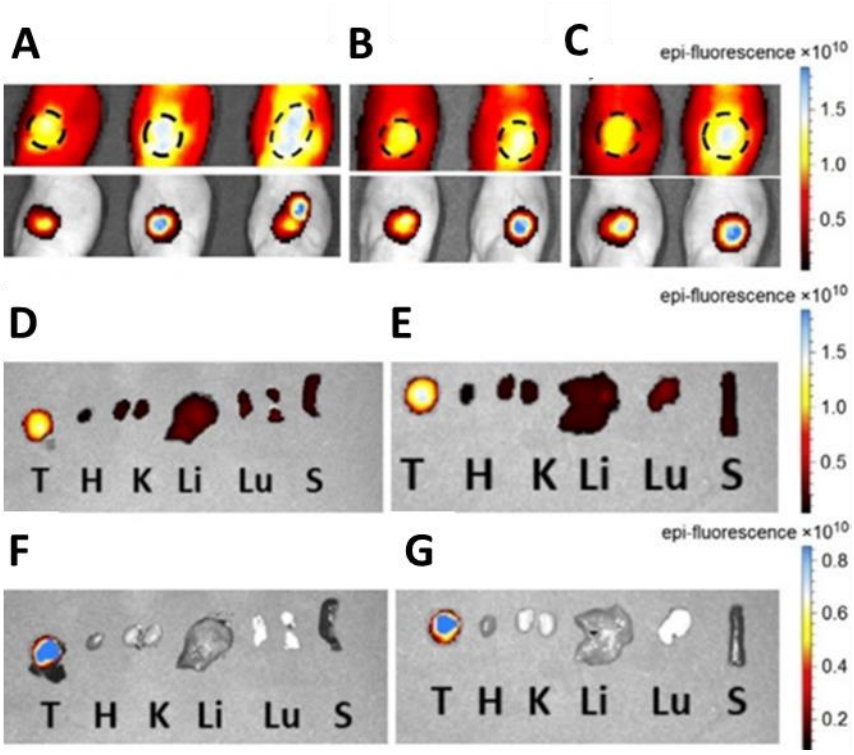

Figure 21: Localization of Cy-Dasatinib to Tumor Site

Near infrared from cyanine dye conjugated to Dasatinib and fluorescence of RFP in tumor tissue showing the region of interest after retroorbital IV injections (10 mg/kg) at : **(A)** 24, **(B)** 48, and **C)** 72 h. Postmortem fluorescence of organs after sacrifice at 72 h: **(D)** near-IR for mouse 1; **(E)** near-IR for mouse 2; F) RFP from tumor from mouse 1; **(G)** RFP from tumor from mouse 2. Color bars indicate radiant efficiency (RE), which $RE = \frac{p/sec/cm^2/sr}{\mu W/cm^2}$. Reprinted with permission from “Conjugation of Dasatinib with MHI-148 Has a Significant Advantageous Effect in Viability Assays for Glioblastoma Cells” by Usama *et al*., 2019, *ChemMedChem*, 14, 17, 1575-1579. Copyright 2021 Wiley.

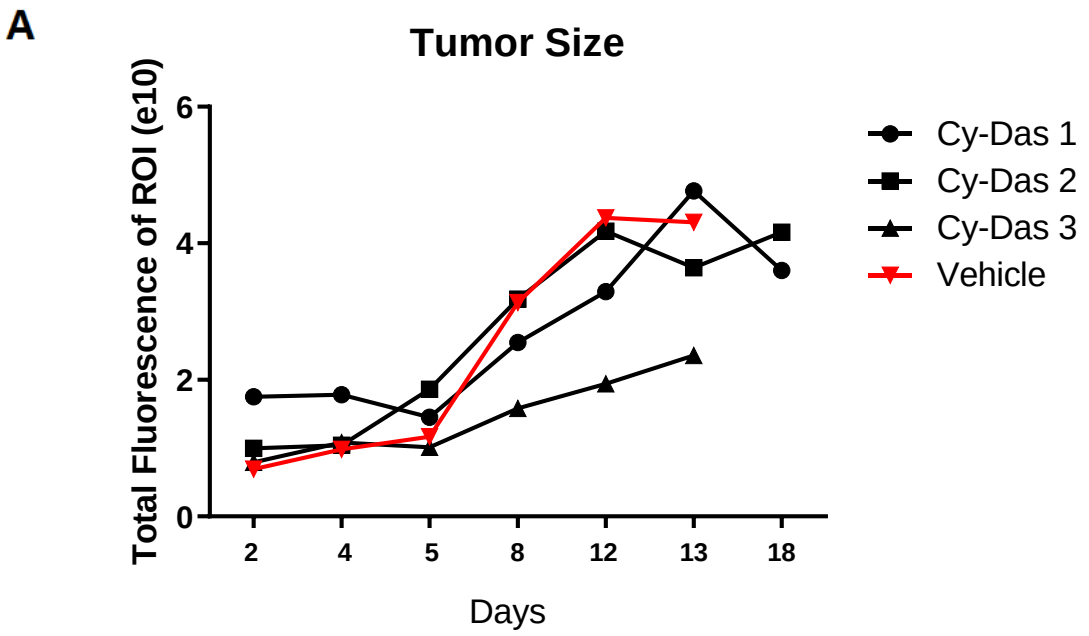

Figure 22: Cy-Dasatinib Efficacy on Subcutaneous GBM Tumors

(A) Size of subcutaneous U87-RFP-LUC tumors measured by fluorescence from RFP signaling in cancer cells. Individual tumor growth represented from mouse replicates (1-3) compared to vehicle control.

Crizotinib

The final compound under investigation for GBM treatment was another tyrosine kinase inhibitor, Crizotinib, which has been shown to inhibit ALK, MET, and ROS1 and is FDA approved to treat non-small cell lung carcinoma. Furthermore, we show that Crizotinib is efficacious in inhibiting NIK with an IC50 of 2.85μM unconjugated and 3.88μM conjugated to the cyanine dye (Appendix B, Supp. Figure 11). Unlike Gemcitabine and Dasatinib, Crizotinib was conjugated to cyanine dye, IR-786, but the conjugation strategy was done in a similar manner to Gemcitabine with Crizotinib being bound to the center of the dye, replacing the meso-chloride. *In vitro* experimentation demonstrated that the IR-786 dye, Crizotinib, and the dye conjugated Crizotinib were efficient in inhibiting proliferation, invasion on a sphere growth of human glioma cells (Figure 23A-C). Initial xenograft experiments with a form of the dye conjugated Crizotinib demonstrated that IR-Criz localizes to the tumor site of subcutaneous U87 gliomas as seen *in vivo* and with postmortem analysis (Figure 24 A,B). More importantly, IR-Criz also showed efficacy in inhibiting tumor growth (Figure 24C). Further xenograft experimentation with intracranial engraftment of human glioma cells (BT25 and U87) showed that, post IV injection, IR-Criz is also capable of crossing the blood brain barrier and localizing to intracranial tumors (Figure 25A,B). Similar to the other compounds conjugated to the different cyanine dye, both IR-Criz and dye alone localized to tumor sites, but more importantly, IR-Criz remained at the intracranial tumor site days post injection. Though dye and IR-Criz were observed in healthy tissue too, it appears that the conjugation of Crizotinib to the dye induces proper clearance as seen with higher signal in the kidneys whereas dye alone accumulates in the heart, most likely due to the affinity of cyanine dyes to form an adduct

with albumin (Figure 26 A,B). Tumor growth was monitored by luminescence and after 5 weeks of IV treatment with the various compounds it was observed that though dye alone seemed to have efficacy on GBM progression, IR-Criz had improved efficacy than Crizotinib alone (Figure 27 A,B). Histology analysis of intracranial tumors also demonstrated IR-Criz having reduced tumor size than Criz alone (Figure 28A). These results complement previously published data demonstrating that Crizotinib conjugated to IR-786 improved efficacy on GBM treatment *in vitro* than Crizotinib alone [151]. Furthermore, weights did not significantly differ among mice receiving chemotherapeutics or to those without tumors or treatment (Appendix B, Supp. Figure 12A). In addition to monitoring weights of mice undergoing treatment, alanine transferase levels were also measured in the plasma of mice. ALT is an active enzyme in the liver and during liver damage becomes secreted, increasing levels in the blood. No significant difference was observed between treatment groups indicating no differences in liver toxicity among the different treatments (Appendix B, Supp. Figure 12B). Dissimilarity in weight coupled with no significant difference in ALT levels indicates low toxicity of the chemotherapeutics at the given dosage. Overall, the heptamethine cyanine dye, IR-786, and IR-Criz are seen to be able to pass the blood brain barrier and localize to tumor sites up to a few days with IR-Criz have better clearance than dye alone, and more importantly have increased efficacy than Crizotinib alone.

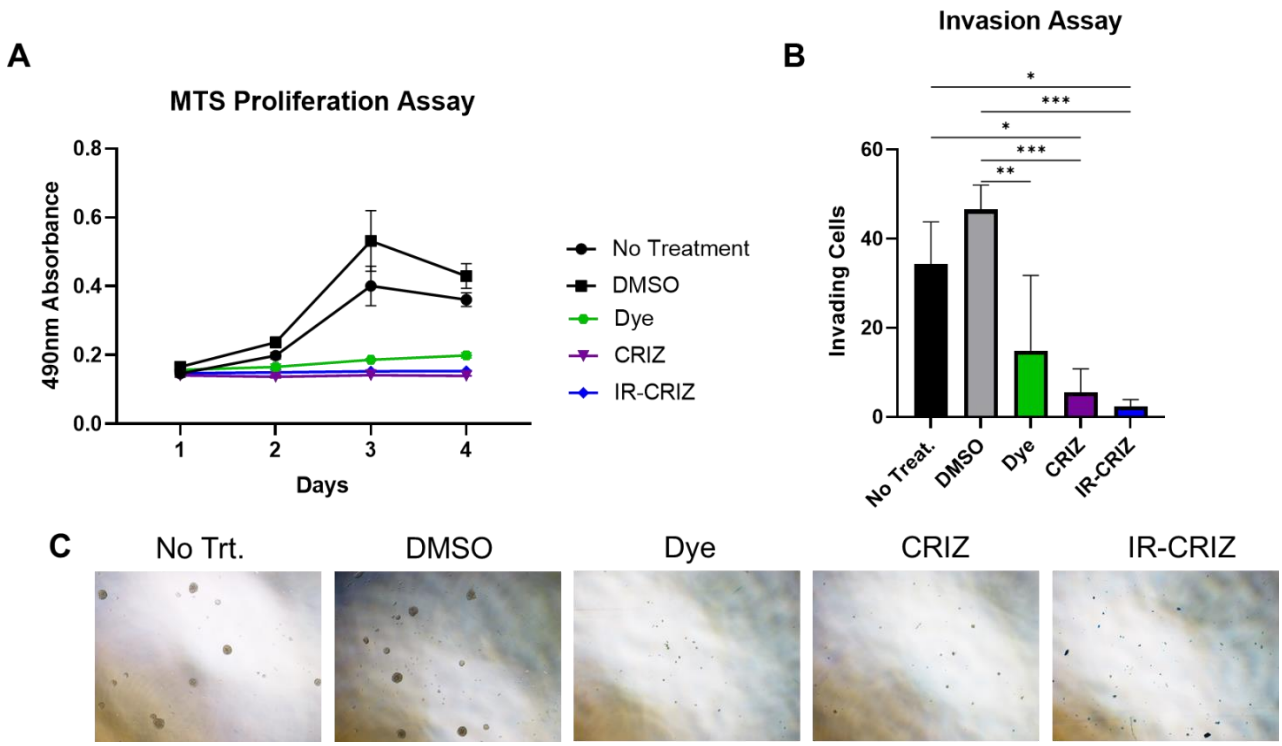

Figure 23: Cyanine Dye and Crizotinib Inhibit Proliferation of Glioma Cells

(A) MTS proliferation assay of BT25 human glioma cells over a four day period, treated with 5μM of individual compounds on day 0. **(B)** Invasion assay of BT25 human glioma cells after 48hrs treatment with respective compounds. **(C)** Sphere assay of BT25 human glioma cells grown non-adherently and treated with 5μM of individual compounds.

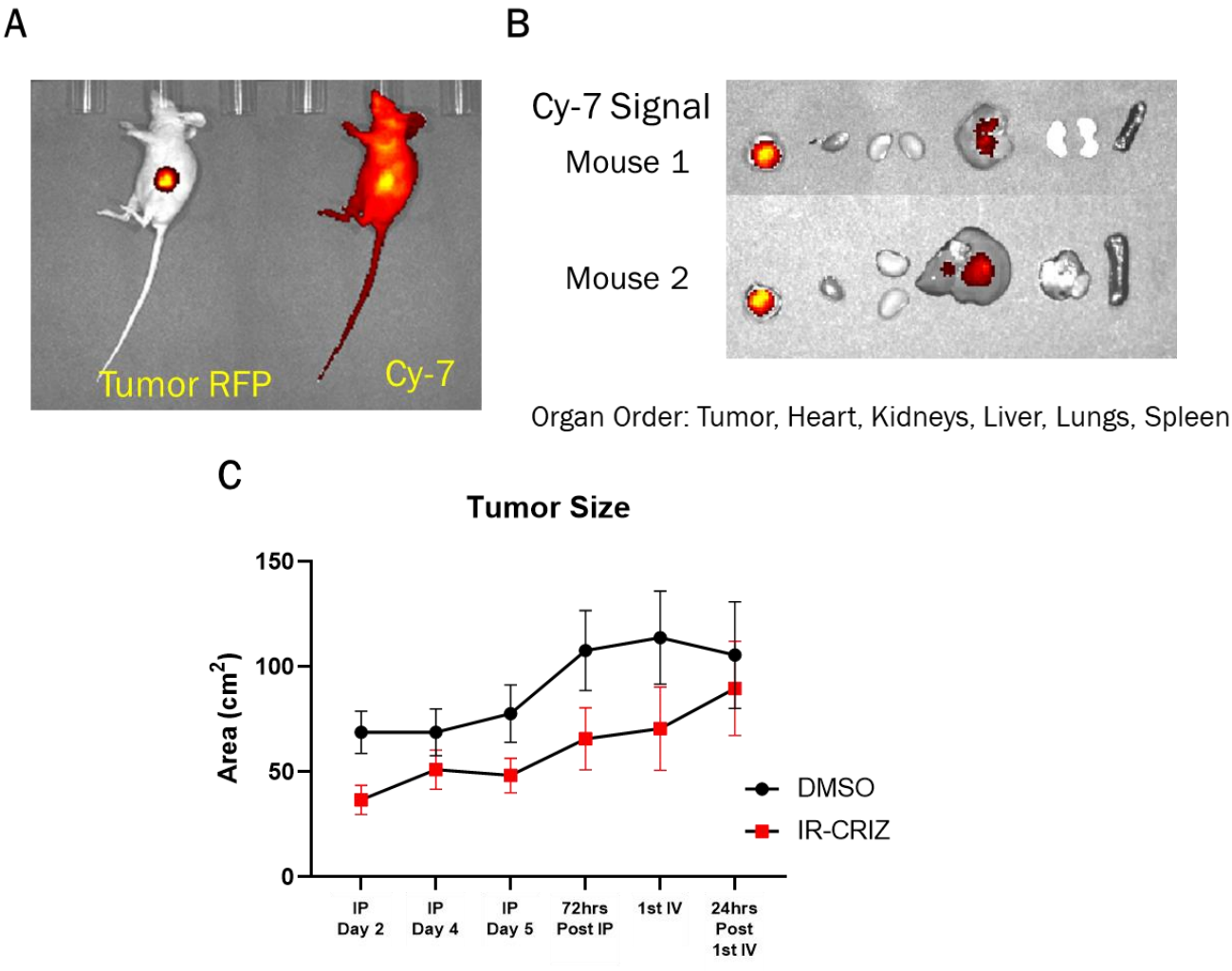

Figure 24: Cyanine Dye and Conjugated Crizotinib Localize to Subcutaneous Glioblastomas

(A) Fluorescence (RFP) from U87 cells at the subcutaneous tumor site and the near infrared fluorescence of cyanine conjugated crizotinib after injection. **(B)** Near infrared fluorescence of cyanine conjugated crizotinib at dissected tumor, heart, liver, kidneys, and spleen post IV injection. **(C)** Tumor size of DMSO or IR-CRIZ treated mice by caliper measurements.

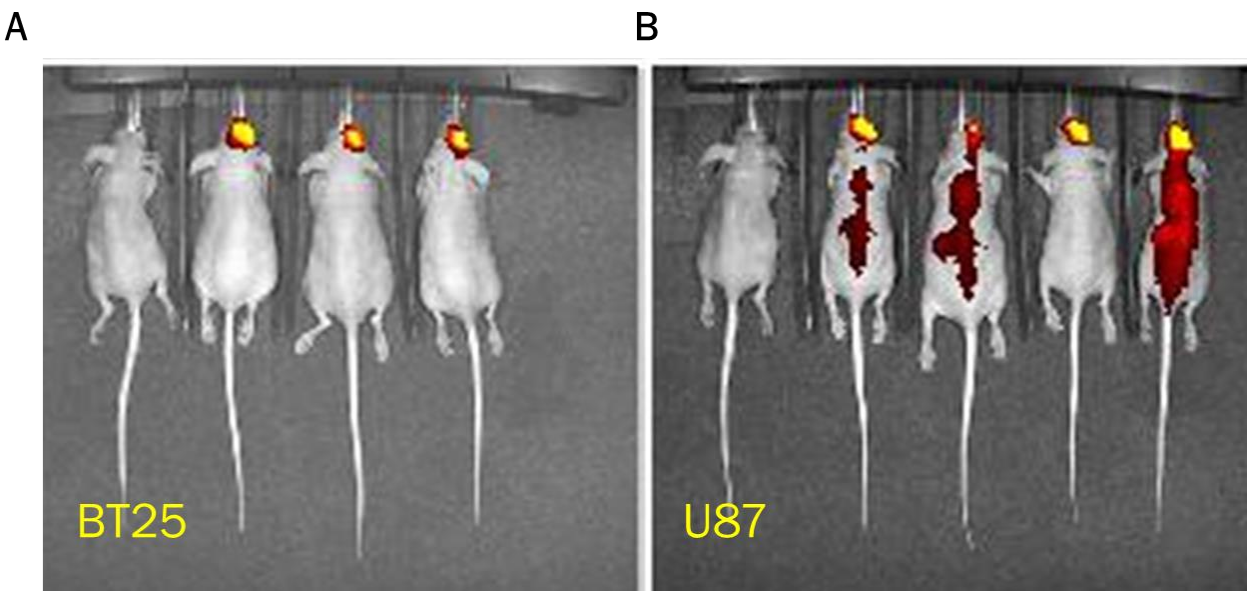

Figure 25: Cyanine Dye and Conjugated Compounds Cross the Blood Brain Barrier and Localize to Intracranial Glioblastomas

Near infrared fluorescence of cyanine conjugated crizotinib after IV injection **(A)** localizing to intracranial site of BT25 (human derived) glioma cells and **(B)** U87 gliomas.

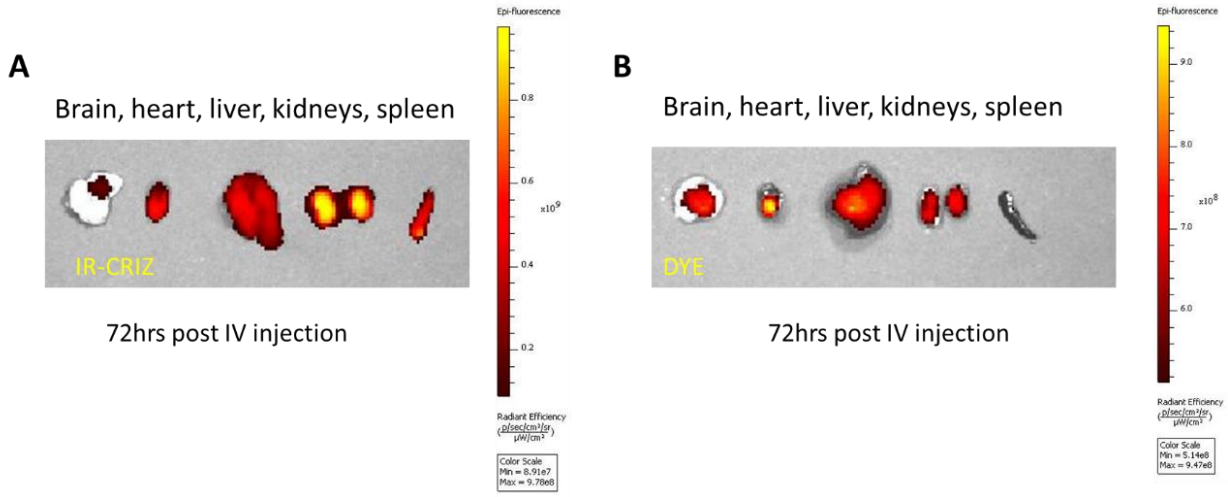

Figure 26: Cyanine Dye and Conjugated Crizotinib Remain at Intracranial Tumor for Extended Time

Near infrared fluorescence of **(A)** cyanine conjugated crizotinib or **(B)** dye alone at dissected intracranial tumor, heart, liver, kidneys, and spleen at 72 hours post IV injection.

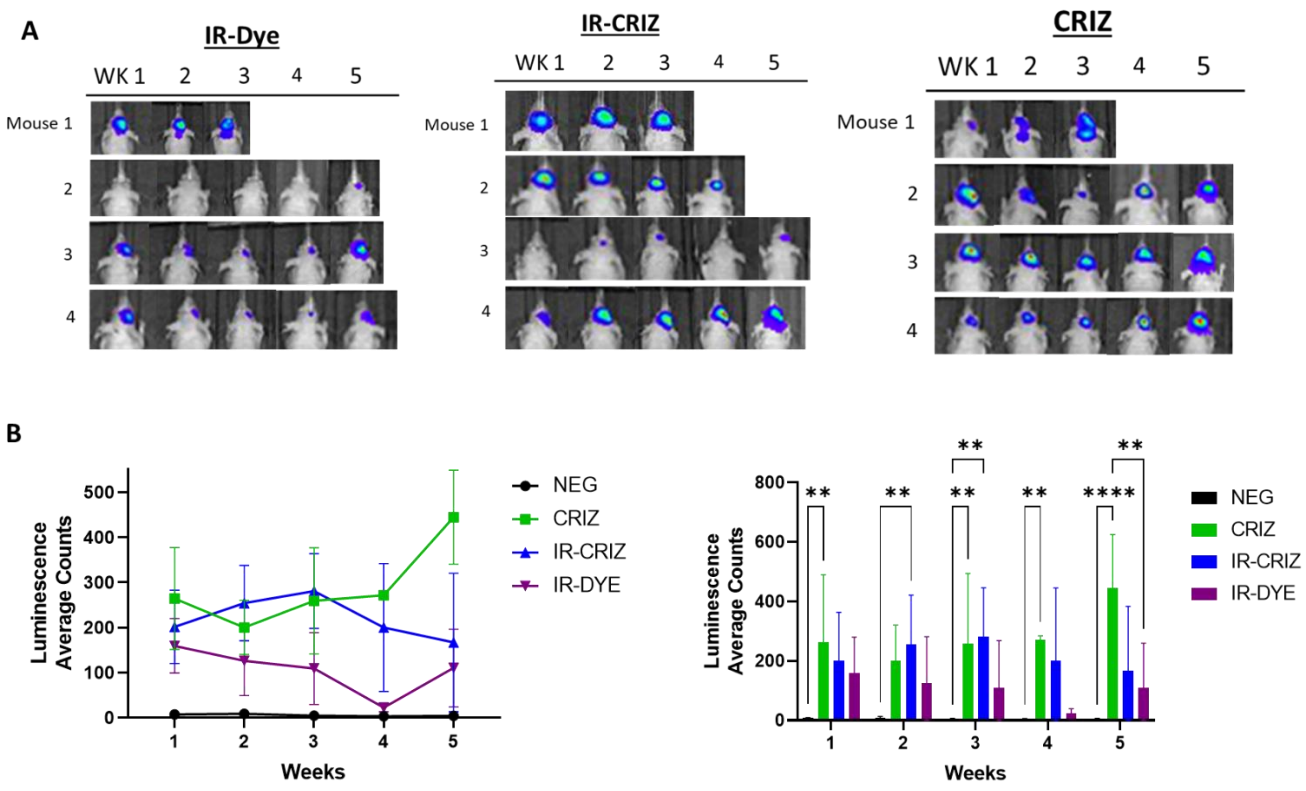

Figure 27: Conjugation of Cyanine Dyes Improves Efficacy of Crizotinib on Glioblastoma Treatment

(A) Luminescence from intracranial U87-LUC-RFP glioblastoma treated with IV injections of cyanine dye, cyanine-crizotinib, or crizotinib. **(B)** Average luminescence counts over 5 week period from n=3,4 mice from treatment groups.

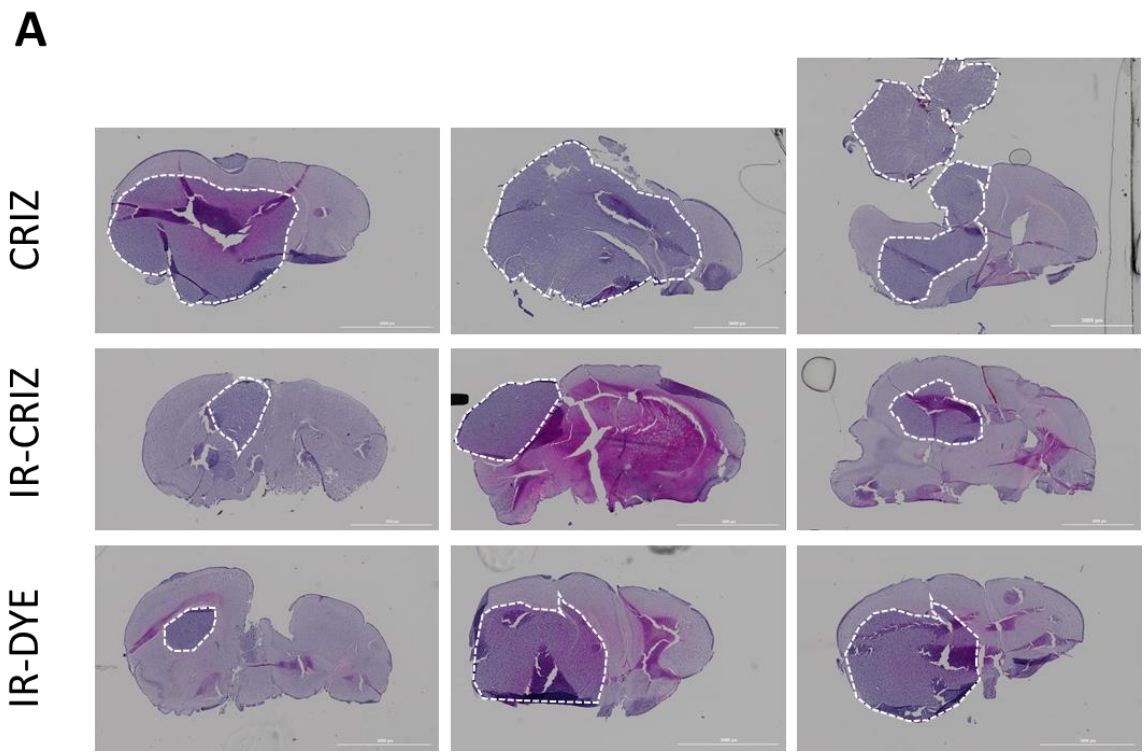

Figure 28: Postmortem Analysis of IR-CRIZ/CRIZ/IR-Dye Treated Intracranial GBM

(A) Hematoxylin and Eosin staining of mouse brains injected with U87-RFP-Luc glioblastoma cells after 5 weeks of weekly IV chemotherapeutic treatment of crizotinib (CRIZ), dye conjugated crizotinib (IR-CRIZ), or dye alone (IR-dye).

CHAPTER IV

SUMMARY & CONCLUSION *

Though NIK is well established for being critical in inducing the noncanonical NF-κB pathway, several studies have highlighted NF-κB-independent NIK functions in regulating cellular processes and disease (Figure 26). Previously published roles for NIK demonstrated induction of liver steatosis through regulation of PPARα phosphorylation and recruitment of ERK1/2 and MEK1/2, regulating beta oxidation and inflammation in the liver [50]. Another study also showed that liver specific deletion of NIK inhibited liver steatosis even under a HFD though synergism between hepatocytes and Kupffer cells [49]. Additionally, NIK was shown to independently regulate glucose homeostasis by direct phosphorylation of CREB, increasing CREB stabilization to regulate glucagon activity [48]. NIK was also observed to induce apoptosis independent of the noncanonical NF-κB pathway through phosphorylation of RIP1 [152]. In cancer models, increased NIK activity has been linked to cell survival and tumorigenesis through association with β-catenin and upregulation of pro-survival genes [71]. Furthermore, NIK can regulate mitochondrial function through dynamin-related protein 1 (DRP1) activity, in a manner that is independent of downstream IKK/NF-κB signaling, resulting in amplification of tumorigenic effects and deregulated cancer metabolism [56,102].

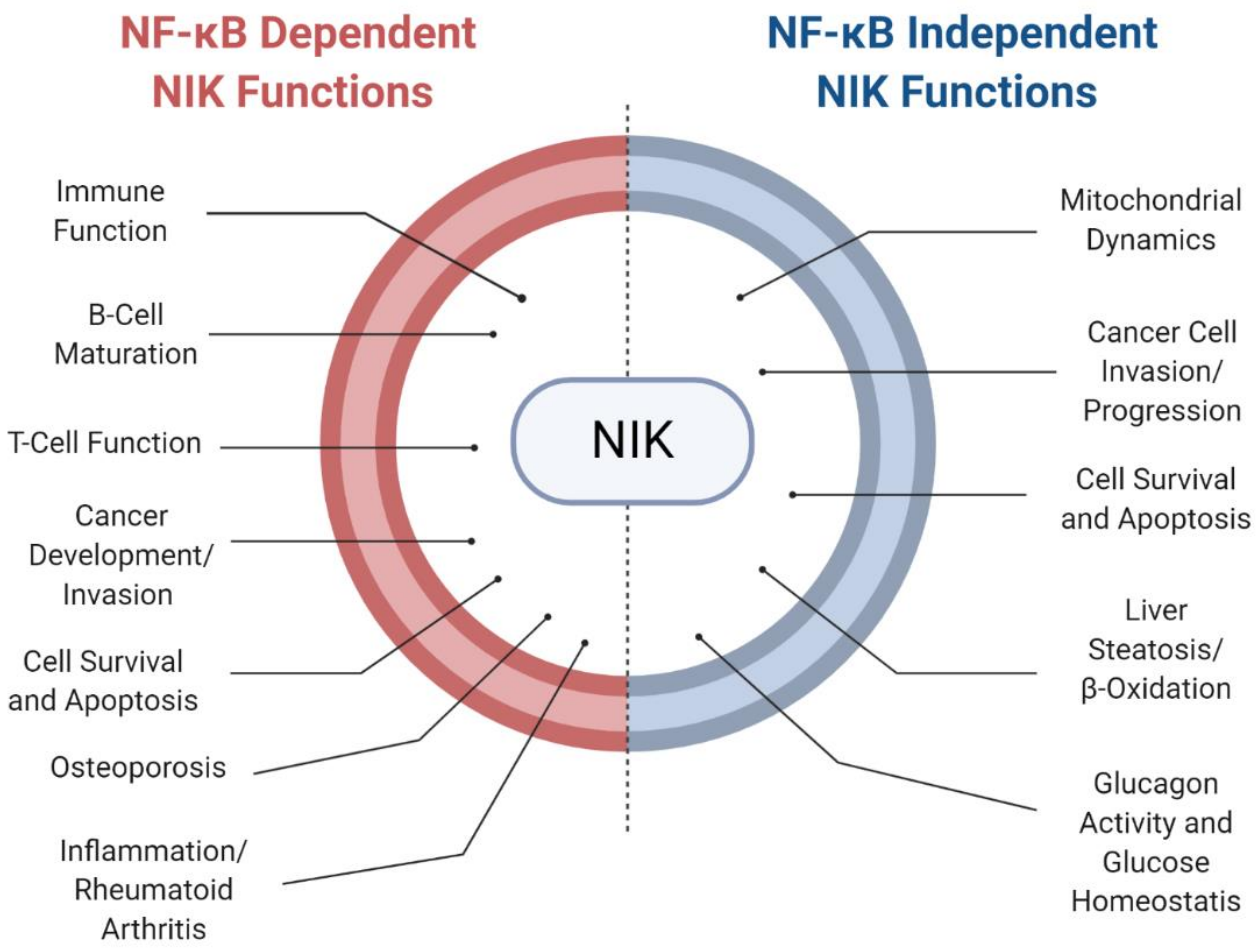

Figure 29: NIK mediation of health and disease. NF-κB-dependent and -independent NIK regulation of cellular processes and disease. Reprinted with permission from "NF-κB-Inducing Kinase (NIK) in Immunity, Inflammation, and Cancer" by Kathryn M. Pflug and Raquel Sitcheran, 2020. IJMS, Volume 21, 8470, Copyright by Creative Commons Attribution License.

Data presented here further establishes NF-κB-independent and -dependent roles for NIK. Having demonstrated that systemic NIK KO mice develop less fat, we show that this phenotype is due to metabolic regulation by NIK independently of the noncanonical NF-κB pathway and adipocyte development that is dependent on the noncanonical NF-κB pathway. Loss of NIK increases metabolic demand seen with increases in both basal oxidative phosphorylation and glycolysis. NIK was shown to regulate mitochondria efficiency through SRC and proton leak as seen in preadipocytes and *ex vivo* adipose tissue. Though this metabolic phenotype persisted from cells to isolated tissue, systemically female NIK KO mice demonstrated to have higher metabolism and greater differences from WT than their male counterparts. Developmentally we show the loss of NIK severely inhibited cells *in vitro* from undergoing adipogenesis which was mirrored in RelB knockout cells, and this phenotype was not altered by the overexpression of RelA nor did the loss of RelA impact adipogenesis, demonstrating NIK regulates adipogenesis through the noncanonical NF-κB pathway without impact from the canonical NF-κB pathway. More importantly, after a regimen of a HFD, NIK KO mice remained leaner while improving insulin sensitivity, glucose clearance, and showed less lipid accumulation in the liver than WT mice. Given these roles for NIK in regulating metabolism and adipose tissue, we show that the loss of NIK protects mice from developing diet-induced obesity and accompanying complications associated with metabolic syndrome.

While much remains to be learned about the full spectrum of the functions of NIK in health and disease, particularly with regard to NF-κB-independent signaling, it is evident that NIK and noncanonical NF-κB signaling are important for many diverse functions of immune cells, inflammatory disease pathogenesis, and malignancies. Given

the importance and relevance NIK and the NF-κB pathway has on regulating cellular process many studies had sought to investigate the use of inhibitors to attenuate the effects of aberrant regulation of NF-κB in diseased states, including the use of NIK inhibitors (see Table 1). Studies using NIK specific inhibitors have demonstrated efficient treatment against a range of disorders including liver steatosis and inflammation [50,110,153], rheumatoid arthritis [154] , osteoporosis [155], lupus [39], and cancers including pancreatic [156], melanoma [157], and lymphoma [69]. Here we also demonstrate that Crizotinib is also a NIK inhibitor and has efficacy in deterring GBM growth. In improvement of chemotherapeutics, we demonstrate, as with previously published data, that the use cyanine dyes conjugation improves such aspects as drug delivery and preferential targeting to the tumor site. Use of this approach in chemotherapeutics can also be applicable to NIK inhibitors in the treatments of various cancers including GBM, where HMCDs are shown to improve compound crossing of the blood brain barrier. Although the dual roles that NIK plays in promoting or attenuating cell survival depending on cell context must be an important consideration in therapeutic approaches targeting NIK, small-molecule pharmacological inhibitors of NIK have tremendous potential to be potent stand-alone or combinatorial therapeutics in a wider range of diseases than previously appreciated.

Table 1. Nuclear factor kappa-light-chain-enhancer of activated B cells-inducing kinase (NIK) inhibitors. Brief list of small molecule and natural NIK inhibitors and correlating disease treatment. Reprinted with permission from "NF-κB-Inducing Kinase (NIK) in Immunity, Inflammation, and Cancer" by Kathryn M. Pflug and Raquel Sitcheran, 2020. IJMS, Volume 21, 8470, Copyright by Creative Commons Attribution License.

Disease	NIK Inhibitor	Therapeutic Effect
Inflammatory/ Immune diseases: • Liver inflammation/ steatosis • Rheumatoid arthritis • Osteoporosis • Lupus	**B022**	Inhibitor of NIK and subsequent liver inflammation and steatosis under alcoholic liver model [158]. Reduction in liver inflammation and damage due to toxin treatment of carbon tetrachloride [153].
	XT2	NIK inhibitor that suppresses hepatocyte inflammation generated by toxin-induced liver injury by carbon tetrachloride, but to a lesser extent than B022 [159].
	NIK SMI1 (small molecule inhibitor 1)	Favorable to inhibition of BAFF-induced B-cell survival [154]. Inhibits NIK in immune cells with improved survival rate in murine model of lupus [160].
	Cpd33 (NIK Specific Inhibitor Compound 33)	Specifically inhibits noncanonical NF-κB pathway. Studied with in vitro RANKL activation and inhibition of downstream transcription factor NFATc1. Treatment with Cpd33 inhibits osteoclastogenesis in vitro and in murine OVX model. Cpd33

Table 1 Continued

Disease	NIK Inhibitor	Therapeutic Effect
		treatment also inhibited bone absorption ability in mature osteoclasts and overall prevented bone loss in murine model [155].
Cancer: • Leukemias • Lymphomas • Pancreatic cancer • Breast cancer • Melanoma	**N-(3-(6-benzamido-3a,7a-dihydrobenzo[d]oxazol-2-yl)-phenyl)benzamide**	NIK inhibitor with general IC_{50} of 48.9 μM and inhibition rate of about 56%. This is inhibitor was less efficient than B022 that had an IC_{50} of 9.9 nM. In SW1990 (pancreatic cancer cells), inhibitor had IC_{50} of 20.1 μM [161].
	4H-isoquinoline-1,3-dione	Inhibits NIK activity by insertion to ATP-binding site. Has an IC_{50} of 51 μM and analogs are inhibitors for CDK4 and IGF-1R [162]. Treatment of Hodgkin lymphoma through inhibition of NIK/RelB [163].
	N-Acetyl-3-aminopyrazoles	Selective inhibitor of NIK with IC_{50} of about 8.4 μM. Over 80% NF-κB inhibition in multiple myeloma cells at 25 μM, but low inhibition in MDA-MB-231 and SKBr3 cells even at 100 μM [164].
	Mangiferin	A natural inhibitor of NF-κB kinases including NIK in a dose-dependent manner. Treatment with 100–200 mg/kg of mangiferin significantly inhibited melanoma tumor growth and metastasis [157].

REFERENCES

1. Akemi Matsushima, T. K. Essential role of nuclear factor (NF)-κB-inducing kinase and inhibitor of κB (IκB) kinase α in NF-κB activation through lymphotoxin β receptor, but not through tumor necrosis factor receptor I. *Journal of Experimental Medicine* **193**, 631–636 (2001).
2. Li Yin1, L. W. Defective lymphotoxin-beta receptor-induced NF-kappaB transcriptional activity in NIK-deficient mice. *Science* (2001).
3. Shinkura, R. *et al.* Alymphoplasia is caused by a point mutation in the mouse gene encoding Nf-κb-inducing kinase. *Nat Genet* **22**, 74–77 (1999).
4. Liu, J. *et al.* Structure of the nuclear factor kappaB-inducing kinase (NIK) kinase domain reveals a constitutively active conformation. *J Biol Chem* **287**, 27326–34 (2012).
5. Qing, G., Qu, Z. & Xiao, G. Stabilization of basally translated NF-kappaB-inducing kinase (NIK) protein functions as a molecular switch of processing of NF-kappaB2 p100. *J Biol Chem* **280**, 40578–82 (2005).
6. Sanjo, H., Zajonc, D. M., Braden, R., Norris, P. S. & Ware, C. F. Allosteric regulation of the ubiquitin:NIK and ubiquitin:TRAF3 E3 ligases by the lymphotoxin-beta receptor. *J Biol Chem* **285**, 17148–55 (2010).
7. Zarnegar, B. J. *et al.* Noncanonical NF-kappaB activation requires coordinated assembly of a regulatory complex of the adaptors cIAP1, cIAP2, TRAF2 and TRAF3 and the kinase NIK. *Nat Immunol* **9**, 1371–8 (2008).
8. Zhang, Q., Lenardo, M. J. & Baltimore, D. 30 Years of NF-κB: A Blossoming of Relevance to Human Pathobiology. *Cell* **168**, 37–57 (2017).
9. Baldwin, A. S. The NF-κB and IκB Proteins: New Discoveries and Insights. *Annual Review of Immunology* **14**, 649–681 (1996).

10. Oeckinghaus, A. & Ghosh, S. The NF-kappaB family of transcription factors and its regulation. *Cold Spring Harb Perspect Biol* **1**, a000034 (2009).

11. Gray, C. M. *et al.* Noncanonical NF-κB signaling is limited by classical NF-κB activity. *Sci Signal* **7**, ra13 (2014).

12. Jin, J. *et al.* The kinase TBK1 controls IgA class switching by negatively regulating noncanonical NF-κB signaling. *Nat. Immunol.* **13**, 1101–1109 (2012).

13. Razani, B., Reichardt, A. D. & Cheng, G. Non-canonical NF-κB signaling activation and regulation: principles and perspectives. *Immunological Reviews* **244**, 44–54 (2011).

14. Huang, T. *et al.* CRL4DCAF2 negatively regulates IL-23 production in dendritic cells and limits the development of psoriasis. *J. Exp. Med.* **215**, 1999–2017 (2018).

15. Sun, S. C. Non-canonical NF-kappaB signaling pathway. *Cell Res* **21**, 71–85 (2011).

16. Lin, X. *et al.* Molecular Determinants of NF-κB-Inducing Kinase Action. *Mol Cell Biol* **18**, 5899–5907 (1998).

17. LEI LING, Z. C. NF-kB-inducing kinase activates IKK-a by phosphorylation of ser-176. *Immunology* **95**, 3792–3797 (1998).

18. Xiao, G., Fong, A. & Sun, S. C. Induction of p100 processing by NF-kappaB-inducing kinase involves docking IkappaB kinase alpha (IKKalpha) to p100 and IKKalpha-mediated phosphorylation. *J Biol Chem* **279**, 30099–105 (2004).

19. M Heusch 1, L. L. The generation of nfkb2 p52: mechanism and efficiency. *Oncogene* 6201–6208 (1999).

20. Liang, C., Zhang, M. & Sun, S. C. beta-TrCP binding and processing of NF-kappaB2/p100 involve its phosphorylation at serines 866 and 870. *Cell Signal* **18**, 1309–17 (2006).

21. Malinin, N. L., Boldin, M. P., Kovalenko, A. V. & Wallach, D. MAP3K-related kinase involved in NF-KB induction by TNF, CD95 and IL-1. *Nature* **385**, 540–544 (1997).

22. Oeckinghaus, A., Hayden, M. S. & Ghosh, S. Crosstalk in NF-kappaB signaling pathways. *Nat Immunol* **12**, 695–708 (2011).

23. Salmeron, A. *et al.* Direct phosphorylation of NF-kappaB1 p105 by the IkappaB kinase complex on serine 927 is essential for signal-induced p105 proteolysis. *J Biol Chem* **276**, 22215–22 (2001).

24. Orian, A. *et al.* SCF(beta)(-TrCP) ubiquitin ligase-mediated processing of NF-kappaB p105 requires phosphorylation of its C-terminus by IkappaB kinase. *EMBO J.* **19**, 2580–2591 (2000).

25. Lin, L., DeMartino, G. N. & Greene, W. C. Cotranslational biogenesis of NF-kappaB p50 by the 26S proteasome. *Cell* **92**, 819–828 (1998).

26. Gonzalez-Murillo, A. *et al.* The NFKB Inducing Kinase Modulates Hematopoiesis During Stress. *Stem Cells* **33**, 2825–37 (2015).

27. Brightbill, H. D. *et al.* Conditional Deletion of NF-kappaB-Inducing Kinase (NIK) in Adult Mice Disrupts Mature B Cell Survival and Activation. *J Immunol* **195**, 953–64 (2015).

28. Myles, A. & Cancro, M. P. The NIK of time for B cells. *Eur. J. Immunol.* **46**, 547–551 (2016).

29. Li, Y. *et al.* Cell intrinsic role of NF-κB-inducing kinase in regulating T cell-mediated immune and autoimmune responses. *Sci Rep* **6**, 22115 (2016).

30. Lacher, S. M. *et al.* NF-κB inducing kinase (NIK) is an essential post-transcriptional regulator of T-cell activation affecting F-actin dynamics and TCR signaling. *Journal of Autoimmunity* **94**, 110–121 (2018).

31. Zeng, R., Faccio, R. & Novack, D. V. Alternative NF-κB Regulates RANKL-Induced Osteoclast Differentiation and Mitochondrial Biogenesis via Independent Mechanisms: ALTERNATIVE NF-κB CONTROLS MITOCHONDRIA AND DEVELOPMENT IN OSTEOCLASTS. *J Bone Miner Res* **30**, 2287–2299 (2015).

32. Sergio Vaira, T. J. & Julie O'Neal, W. Z. RelB is the NF-κB subunit downstream of NIK responsible for osteoclast differentiation. *PNAS* (2008).

33. Bakkar, N. *et al.* IKK/NF-kappaB regulates skeletal myogenesis via a signaling switch to inhibit differentiation and promote mitochondrial biogenesis. *J Cell Biol* **180**, 787–802 (2008).

34. Canicio, J. *et al.* Nuclear Factor κB-inducing Kinase and IκB Kinase-α Signal Skeletal Muscle Cell Differentiation. *J. Biol. Chem.* **276**, 20228–20233 (2001).

35. Hoesel, B. & Schmid, J. A. The complexity of NF-κB signaling in inflammation and cancer. *Molecular Cancer* **12**, 86 (2013).

36. Taniguchi, K. & Karin, M. NF-κB, inflammation, immunity and cancer: coming of age. *Nature Reviews Immunology* **18**, 309–324 (2018).

37. Willmann, K. L. *et al.* Biallelic loss-of-function mutation in NIK causes a primary immunodeficiency with multifaceted aberrant lymphoid immunity. *Nat Commun* **5**, 5360 (2014).

38. Schlechter, N. *et al.* Exome Sequencing Identifies a Novel MAP3K14 Mutation in Recessive Atypical Combined Immunodeficiency. *Frontiers in immunology* **8**, 48–15 (2017).

39. Brightbill, H. D. *et al.* NF-κB inducing kinase is a therapeutic target for systemic lupus erythematosus. *Nat Commun* **9**, 179 (2018).

40. Arya, R. *et al.* Genetic Variants Influencing Joint Damage in Mexican Americans and European Americans With Rheumatoid Arthritis: Genetic Variants Influencing Joint Damage. *Genet. Epidemiol.* **39**, 678–688 (2015).

41. Noort, A. R. *et al.* Tertiary Lymphoid Structures in Rheumatoid Arthritis. *The American Journal of Pathology* **185**, 1935–1943 (2015).

42. Noort, A. R., Tak, P. P. & Tas, S. W. Non-canonical NF-κB signaling in rheumatoid arthritis: Dr Jekyll and Mr Hyde? *Arthritis Res Ther* **17**, 15 (2015).

43. Zhou, B. *et al.* Therapeutic effects of a novel BAFF blocker on arthritis. *Sig Transduct Target Ther* **4**, 19 (2019).

44. Yang, C. *et al.* NIK stabilization in osteoclasts results in osteoporosis and enhanced inflammatory osteolysis. *PLoS One* **5**, e15383 (2010).

45. Russo, L. & Lumeng, C. N. Properties and functions of adipose tissue macrophages in obesity. *Immunology* **155**, 407–417 (2018).

46. Dorrington, M. G. & Fraser, I. D. C. NF-κB Signaling in Macrophages: Dynamics, Crosstalk, and Signal Integration. *Front. Immunol.* **10**, 705 (2019).

47. Zhao, P. *et al.* TBK1 at the Crossroads of Inflammation and Energy Homeostasis in Adipose Tissue. *Cell* **172**, 731-743.e12 (2018).

48. Sheng, L. *et al.* NF-κB–inducing kinase (NIK) promotes hyperglycemia and glucose intolerance in obesity by augmenting glucagon action. *Nat Med* **18**, 943–949 (2012).

49. Liu, Y. *et al.* Liver NF-κB-Inducing Kinase Promotes Liver Steatosis and Glucose Counterregulation in Male Mice With Obesity. *Endocrinology* **158**, 1207–1216 (2017).

50. Li, Y. *et al.* NIK links inflammation to hepatic steatosis by suppressing PPARα in alcoholic liver disease. *Theranostics* **10**, 3579–3593 (2020).

51. Malle, E. K. *et al.* Nuclear factor κB–inducing kinase activation as a mechanism of pancreatic β cell failure in obesity. *Journal of Experimental Medicine* **212**, 1239–1254 (2015).

52. Choudhary, S. *et al.* NF-κB-Inducing Kinase (NIK) Mediates Skeletal Muscle Insulin Resistance: Blockade by Adiponectin. *Endocrinology* **152**, 3622–3627 (2011).

53. Zhang, N. *et al.* Sustained NFκB inhibition improves insulin sensitivity but is detrimental to muscle health. *Aging Cell* **16**, 847–858 (2017).

54. Bakkar, N. *et al.* IKKα and alternative NF-κB regulate PGC-1β to promote oxidative muscle metabolism. *The Journal of Cell Biology* **196**, 497–511 (2012).

55. Jung, J. U. *et al.* NIK/MAP3K14 Regulates Mitochondrial Dynamics and Trafficking to Promote Cell Invasion. *Curr Biol* **26**, 3288–3302 (2016).

56. Kamradt, M. L. *et al.* NIK promotes metabolic adaptation of glioblastoma cells to bioenergetic stress. *Cell Death & Disease* **12**, 1–18 (2021).

57. Gu, M. *et al.* NF-κB-inducing kinase maintains T cell metabolic fitness in antitumor immunity. *Nat Immunol* **22**, 193–204 (2021).

58. Zeng, T. *et al.* Blocking Nuclear Factor-Kappa B Protects against Diet-Induced Hepatic Steatosis and Insulin Resistance in Mice. *PLoS One* **11**, e0149677 (2016).

59. Park, M. & Hong, J. Roles of NF-κB in Cancer and Inflammatory Diseases and Their Therapeutic Approaches. *Cells* **5**, 15 (2016).

60. Xia, Y., Shen, S. & Verma, I. M. NF-κB, an active player in human cancers. *Cancer Immunol Res* **2**, 823–830 (2014).

61. Maubach, G., Feige, M. H., Lim, M. C. C. & Naumann, M. NF-kappaB-inducing kinase in cancer. *Biochimica et Biophysica Acta (BBA) - Reviews on Cancer* **1871**, 40–49 (2019).

62. Kaltschmidt, B., Greiner, J. F. W., Kadhim, H. M. & Kaltschmidt, C. Subunit-Specific Role of NF-κB in Cancer. *Biomedicines* **6**, 44 (2018).

63. Pattabiraman, D. R. & Weinberg, R. A. Tackling the cancer stem cells — what challenges do they pose? *Nature Reviews Drug Discovery* **13**, 497–512 (2014).

64. Vazquez-Santillan, K. *et al.* NF-kappaB-inducing kinase regulates stem cell phenotype in breast cancer. *Sci Rep* **6**, 37340 (2016).

65. Schramek, D. *et al.* Osteoclast differentiation factor RANKL controls development of progestin-driven mammary cancer. *Nature* **468**, 98–102 (2010).

66. Ohtsu, N. *et al.* Eva1 Maintains the Stem-like Character of Glioblastoma-Initiating Cells by Activating the Noncanonical NF- B Signaling Pathway. *Cancer Research* **76**, 171–181 (2016).

67. Gonzalez-Torres, C. *et al.* NF-κB Participates in the Stem Cell Phenotype of Ovarian Cancer Cells. *Archives of Medical Research* **48**, 343–351 (2017).

68. Xiu, Y. *et al.* Stabilization of NF-κB-Inducing Kinase Suppresses MLL-AF9-Induced Acute Myeloid Leukemia. *Cell Reports* **22**, 350–358 (2018).

69. Ranuncolo, S. M., Pittaluga, S., Evbuomwan, M. O., Jaffe, E. S. & Lewis, B. A. Hodgkin lymphoma requires stabilized NIK and constitutive RelB expression for survival. *Blood* **120**, 3756–63 (2012).

70. Dhawan, P. & Richmond, A. A Novel NF-κB-inducing Kinase-MAPK Signaling Pathway Up-regulates NF-κB Activity in Melanoma Cells. *J. Biol. Chem.* **277**, 7920–7928 (2002).

71. Thu, Y. M. *et al.* NF-κB inducing kinase (NIK) modulates melanoma tumorigenesis by regulating expression of pro-survival factors through the β-catenin pathway. *Oncogene* **31**, 2580–2592 (2012).

72. Doppler, H., Liou, G. Y. & Storz, P. Downregulation of TRAF2 mediates NIK-induced pancreatic cancer cell proliferation and tumorigenicity. *PLoS One* **8**, e53676 (2013).

73. Nishina, T., Yamaguchi, N., Gohda, J., Semba, K. & Inoue, J. NIK is involved in constitutive activation of the alternative NF-κB pathway and proliferation of pancreatic cancer cells. *Biochemical and Biophysical Research Communications* **388**, 96–101 (2009).

74. Teng, H., Xue, L., Wang, Y., Ding, X. & Li, J. Nuclear factor κB -inducing kinase is a diagnostic marker of gastric cancer. *Medicine* **99**, e18864 (2020).

75. Cherry, E. M., Lee, D. W., Jung, J.-U. & Sitcheran, R. Tumor necrosis factor-like weak inducer of apoptosis (TWEAK) promotes glioma cell invasion through induction of NF-κB-inducing kinase (NIK) and noncanonical NF-κB signaling. *Mol Cancer* **14**, 9 (2015).

76. Pang, G., Xie, J., Chen, Q. & Hu, Z. Energy intake, metabolic homeostasis, and human health. *Food Science and Human Wellness* **3**, 89–103 (2014).

77. O'Brien, C. M., Mulukutla, B. C., Mashek, D. G. & Hu, W.-S. Regulation of Metabolic Homeostasis in Cell Culture Bioprocesses. *Trends in Biotechnology* **38**, 1113–1127 (2020).

78. Ma, Y. & Li, J. Metabolic Shifts during Aging and Pathology. *Compr Physiol* **5**, 667–686 (2015).

79. Li, T. *et al.* PKM2 coordinates glycolysis with mitochondrial fusion and oxidative phosphorylation. *Protein Cell* **10**, 583–594 (2019).

80. Yuan, X. *et al.* NAD + /NADH redox alterations reconfigure metabolism and rejuvenate senescent human mesenchymal stem cells in vitro. *Communications Biology* **3**, 1–15 (2020).

81. Duan, K. *et al.* Lactic acid induces lactate transport and glycolysis/OXPHOS interconversion in glioblastoma. *Biochem Biophys Res Commun* **503**, 888–894 (2018).

82. Bar-Even, A., Flamholz, A., Noor, E. & Milo, R. Rethinking glycolysis: on the biochemical logic of metabolic pathways. *Nature Chemical Biology* **8**, 509–517 (2012).

83. Rodic, S. & Vincent, M. D. Reactive oxygen species (ROS) are a key determinant of cancer's metabolic phenotype. *International Journal of Cancer* **142**, 440–448 (2018).

84. Li, X. *et al.* Mitochondria-Translocated PGK1 Functions as a Protein Kinase to Coordinate Glycolysis and the TCA Cycle in Tumorigenesis. *Mol Cell* **61**, 705–719 (2016).

85. Marchetti, P., Fovez, Q., Germain, N., Khamari, R. & Kluza, J. Mitochondrial spare respiratory capacity: Mechanisms, regulation, and significance in non-transformed and cancer cells. *The FASEB Journal* **34**, 13106–13124 (2020).

86. Sriskanthadevan, S. *et al.* AML cells have low spare reserve capacity in their respiratory chain that renders them susceptible to oxidative metabolic stress. *Blood* **125**, 2120–2130 (2015).

87. van der Windt, G. J. W. *et al.* Mitochondrial Respiratory Capacity Is a Critical Regulator of CD8+ T Cell Memory Development. *Immunity* **36**, 68–78 (2012).

88. Huang, P. L. A comprehensive definition for metabolic syndrome. *Dis Model Mech* **2**, 231–237 (2009).

89. Prasun, P. Mitochondrial dysfunction in metabolic syndrome. *Biochimica et Biophysica Acta (BBA) - Molecular Basis of Disease* **1866**, 165838 (2020).

90. Rosen, E. D. & Spiegelman, B. M. Adipocytes as regulators of energy balance and glucose homeostasis. *Nature* **444**, 847–853 (2006).

91. Stern, J. H., Rutkowski, J. M. & Scherer, P. E. Adiponectin, Leptin, and Fatty Acids in the Maintenance of Metabolic Homeostasis through Adipose Tissue Crosstalk. *Cell Metab* **23**, 770–84 (2016).

92. Choe, S. S., Huh, J. Y., Hwang, I. J., Kim, J. I. & Kim, J. B. Adipose Tissue Remodeling: Its Role in Energy Metabolism and Metabolic Disorders. *Front Endocrinol (Lausanne)* **7**, 30 (2016).

93. Lee, B. C. & Lee, J. Cellular and molecular players in adipose tissue inflammation in the development of obesity-induced insulin resistance. *Biochim Biophys Acta* **1842**, 446–62 (2014).

94. Yin, L. *et al.* Defective lymphotoxin-beta receptor-induced NF-kappaB transcriptional activity in NIK-deficient mice. *Science* **291**, 2162–2165 (2001).

95. Akemi Matsushima, T. K. Essential role of nuclear factor (NF)-κB-inducing kinase and inhibitor of κB (IκB) kinase α in NF-κB activation through lymphotoxin β receptor, but not through tumor necrosis factor receptor I. *Journal of Experimental Medicine* **193**, 631–636 (2001).

96. Xiao, G., Fong, A. & Sun, S. C. Induction of p100 processing by NF-kappaB-inducing kinase involves docking IkappaB kinase alpha (IKKalpha) to p100 and IKKalpha-mediated phosphorylation. *J Biol Chem* **279**, 30099–105 (2004).

97. Sun, S. C. Non-canonical NF-kappaB signaling pathway. *Cell Res* **21**, 71–85 (2011).

98. Shinkura, R. *et al.* Alymphoplasia is caused by a point mutation in the mouse gene encoding Nf-κb-inducing kinase. *Nature Genetics* **22**, 74–77 (1999).

99. Li, Y. *et al.* Cell intrinsic role of NF-kappaB-inducing kinase in regulating T cell-mediated immune and autoimmune responses. *Sci Rep* **6**, 22115 (2016).

100. Lacher, S. M. *et al.* NF-κB inducing kinase (NIK) is an essential post-transcriptional regulator of T-cell activation affecting F-actin dynamics and TCR signaling. *Journal of Autoimmunity* **94**, 110–121 (2018).

101. Hamdan, T. A. *et al.* Map3k14 as a Regulator of Innate and Adaptive Immune Response during Acute Viral Infection. *Pathogens* **9**, (2020).

102. Jung, J. U. *et al.* NIK/MAP3K14 Regulates Mitochondrial Dynamics and Trafficking to Promote Cell Invasion. *Curr Biol* **26**, 3288–3302 (2016).

103. Sheng, L. *et al.* NF-kappaB-inducing kinase (NIK) promotes hyperglycemia and glucose intolerance in obesity by augmenting glucagon action. *Nat Med* **18**, 943–9 (2012).

104. Liu, Y. *et al.* Liver NF-κB-Inducing Kinase Promotes Liver Steatosis and Glucose Counterregulation in Male Mice With Obesity. *Endocrinology* **158**, 1207–1216 (2017).

105. Li, Y. *et al.* NIK links inflammation to hepatic steatosis by suppressing PPARα in alcoholic liver disease. *Theranostics* **10**, 3579–3593 (2020).

106. Mota, M., Banini, B. A., Cazanave, S. C. & Sanyal, A. J. Molecular mechanisms of lipotoxicity and glucotoxicity in nonalcoholic fatty liver disease. *Metabolism* **65**, 1049–61 (2016).

107. Pan, X. *et al.* Adipogenic changes of hepatocytes in a high-fat diet-induced fatty liver mice model and non-alcoholic fatty liver disease patients. *Endocrine* **48**, 834–47 (2015).

108. Ren, L. *et al.* Mitochondrial Dynamics: Fission and Fusion in Fate Determination of Mesenchymal Stem Cells. *Frontiers in Cell and Developmental Biology* **8**, 1133 (2020).

109. Even, P. C. & Nadkarni, N. A. Indirect calorimetry in laboratory mice and rats: principles, practical considerations, interpretation and perspectives. *American Journal of Physiology-Regulatory, Integrative and Comparative Physiology* **303**, R459–R476 (2012).

110. Li, Z. *et al.* Discovery of a Potent and Selective NF-κB-Inducing Kinase (NIK) Inhibitor That Has Anti-inflammatory Effects in Vitro and in Vivo. *J. Med. Chem.* **63**, 4388–4407 (2020).

111. Calabrese, C. *et al.* Respiratory complex I is essential to induce a Warburg profile in mitochondria-defective tumor cells. *Cancer & Metabolism* **1**, 11 (2013).

112. Liberti, M. V. & Locasale, J. W. The Warburg Effect: How Does it Benefit Cancer Cells? *Trends Biochem Sci* **41**, 211–218 (2016).

113. Fedorenko, A., Lishko, P. V. & Kirichok, Y. Mechanism of Fatty-Acid-Dependent UCP1 Uncoupling in Brown Fat Mitochondria. *Cell* **151**, 400–413 (2012).

114. Mauvais-Jarvis, F. Sex differences in metabolic homeostasis, diabetes, and obesity. *Biol Sex Differ* **6**, (2015).

115. Riant, E. *et al.* Estrogens Protect against High-Fat Diet-Induced Insulin Resistance and Glucose Intolerance in Mice. *Endocrinology* **150**, 2109–2117 (2009).

116. Handgraaf, S. *et al.* Prevention of Obesity and Insulin Resistance by Estrogens Requires ER Activation Function-2 (ER AF-2), Whereas ER AF-1 Is Dispensable. *Diabetes* **62**, 4098–4108 (2013).

117. Klein, S. L. & Flanagan, K. L. Sex differences in immune responses. *Nature Reviews Immunology* **16**, 626–638 (2016).

118. Eisenreich, W., Rudel, T., Heesemann, J. & Goebel, W. How Viral and Intracellular Bacterial Pathogens Reprogram the Metabolism of Host Cells to Allow Their Intracellular Replication. *Front. Cell. Infect. Microbiol.* **9**, (2019).

119. Sanchez, E. L. & Lagunoff, M. Viral activation of cellular metabolism. *Virology* **479–480**, 609–618 (2015).

120. Tang, T. *et al.* Uncoupling of inflammation and insulin resistance by NF-kappaB in transgenic mice through elevated energy expenditure. *J Biol Chem* **285**, 4637–44 (2010).

121. Pascal Peraldi, M. X. Thiazolidinediones Block Tumor Necrosis Factor-a-induced Inhibition of insulin signaling. *J. Clin. Invest.* **Volume 100**, 1863–1869 (1997).

122. Berg, A. H., Lin, Y., Lisanti, M. P. & Scherer, P. E. Adipocyte differentiation induces dynamic changes in NF-κB expression and activity. *American Journal of Physiology-Endocrinology and Metabolism* **287**, E1178–E1188 (2004).

123. Weidemann, A. *et al.* Classical and alternative NF-kappaB signaling cooperate in regulating adipocyte differentiation and function. *Int J Obes (Lond)* **40**, 452–9 (2016).

124. Louis, D. N. *et al.* The 2007 WHO Classification of Tumours of the Central Nervous System. *Acta Neuropathol* **114**, 97–109 (2007).

125. McLendon, R. E. & Halperin, E. C. Is the long-term survival of patients with intracranial glioblastoma multiforme overstated? *Cancer* **98**, 1745–1748 (2003).

126. Holland, E. C. Glioblastoma multiforme: The terminator. *Proc Natl Acad Sci U S A* **97**, 6242–6244 (2000).

127. Yang, X. *et al.* Optical Imaging of Kidney Cancer with Novel Near Infrared Heptamethine Carbocyanine Fluorescent Dyes. *Journal of Urology* **189**, 702–710 (2013).

128. Yuan, J. *et al.* Near-infrared fluorescence imaging of prostate cancer using heptamethine carbocyanine dyes. *Molecular Medicine Reports* **11**, 821–828 (2015).

129. Zhao, N. *et al.* Optical imaging of gastric cancer with near-infrared heptamethine carbocyanine fluorescence dyes. *Oncotarget* **7**, 57277–57289 (2016).

130. Organic anion transporting polypeptides (OATPs): regulation of expression and function - PubMed. https://pubmed.ncbi.nlm.nih.gov/21395542/.

131. Gibbs, S. L. Near infrared fluorescence for image-guided surgery. *Quant Imaging Med Surg* **2**, 177–187 (2012).

132. Vahrmeijer, A. L., Hutteman, M., van der Vorst, J. R., van de Velde, C. J. H. & Frangioni, J. V. Image-guided cancer surgery using near-infrared fluorescence. *Nat Rev Clin Oncol* **10**, 507–518 (2013).

133. Cooper, E. *et al.* The Use of Heptamethine Cyanine Dyes as Drug-Conjugate Systems in the Treatment of Primary and Metastatic Brain Tumors. *Front Oncol* **11**, 654921 (2021).

134. Wu, J. B. *et al.* Near-infrared fluorescence heptamethine carbocyanine dyes mediate imaging and targeted drug delivery for human brain tumor. *Biomaterials* **67**, 1–10 (2015).

135. Lund, B., Kristjansen, P. E. G. & Hansen, H. H. Clinical and preclinical activity of 2′,2′-difluorodeoxycytidine (gemcitabine). *Cancer Treatment Reviews* **19**, 45–55 (1993).

136. Montano, R. *et al.* Cell cycle perturbation induced by gemcitabine in human tumor cells in cell culture, xenografts and bladder cancer patients: implications for clinical trial designs combining gemcitabine with a Chk1 inhibitor. *Oncotarget* **8**, 67754–67768 (2017).

137. Toschi, L., Finocchiaro, G., Bartolini, S., Gioia, V. & Cappuzzo, F. Role of gemcitabine in cancer therapy. *Future Oncology* **1**, 7–17 (2005).

138. Araujo, J. & Logothetis, C. Dasatinib: a potent SRC inhibitor in clinical development for the treatment of solid tumors. *Cancer Treat Rev* **36**, 492–500 (2010).

139. Faderl, S. *et al.* Outcome of Philadelphia Chromosome-Positive Adult Acute Lymphoblastic Leukemia. *Leukemia & Lymphoma* **36**, 263–273 (2000).

140. Sahu, A., Prabhash, K., Noronha, V., Joshi, A. & Desai, S. Crizotinib: A comprehensive review. *South Asian J Cancer* **2**, 91–97 (2013).

141. Bastiancich, C., Bastiat, G. & Lagarce, F. Gemcitabine and glioblastoma: challenges and current perspectives. *Drug Discovery Today* **23**, 416–423 (2018).

142. Nehoff, H., Parayath, N. N., McConnell, M. J., Taurin, S. & Greish, K. A combination of tyrosine kinase inhibitors, crizotinib and dasatinib for the treatment of glioblastoma multiforme. *Oncotarget* **6**, 37948–37964 (2015).

143. Miklja, Z. *et al.* Everolimus improves the efficacy of dasatinib in PDGFRα-driven glioma. *Journal of Clinical Investigation* **130**, 5313–5325 (2020).

144. Junca, A. *et al.* Crizotinib targets in glioblastoma stem cells. *Cancer Med* **6**, 2625–2634 (2017).

145. Goodwin, C. R. *et al.* Crizotinib and erlotinib inhibits growth of c-Met+/EGFRvIII+ primary human glioblastoma xenografts. *Clinical Neurology and Neurosurgery* **171**, 26–33 (2018).

146. Schiff, D. & Sarkaria, J. Dasatinib in recurrent glioblastoma: failure as a teacher. *Neuro-Oncology* **17**, 910–911 (2015).

147. Grupo Español de Investigación en Neurooncología. *Phase Ib, Open-label, Multicenter, Dose-escalation Study Followed by an Extension Phase to Evaluate the Safety and Activity of the Combination of Crizotinib With Temozolomide and Radiotherapy in Patients With Newly Diagnosed Glioblastoma*. https://clinicaltrials.gov/ct2/show/study/NCT02270034 (2021).

148. Usama, S. M., Lin, C.-M. & Burgess, K. On the Mechanisms of Uptake of Tumor-Seeking Cyanine Dyes. *Bioconjugate Chem.* **29**, 3886–3895 (2018).

149. Jiang, Z. *et al.* Cyanine–Gemcitabine Conjugates as Targeted Theranostic Agents for Glioblastoma Tumor Cells. *J. Med. Chem.* **62**, 9236–9245 (2019).

150. Usama, S. M., Jiang, Z., Pflug, K., Sitcheran, R. & Burgess, K. Conjugation of Dasatinib with MHI-148 Has a Significant Advantageous Effect in Viability Assays for Glioblastoma Cells. *ChemMedChem* **14**, 1575–1579 (2019).

151. Choi, P. J. *et al.* The synthesis of a novel Crizotinib heptamethine cyanine dye conjugate that potentiates the cytostatic and cytotoxic effects of Crizotinib in patient-derived glioblastoma cell lines. *Bioorganic & Medicinal Chemistry Letters* **29**, 2617–2621 (2019).

152. Boutaffala, L. *et al.* NIK promotes tissue destruction independently of the alternative NF-κB pathway through TNFR1/RIP1-induced apoptosis. *Cell Death Differ* **22**, 2020–2033 (2015).

153. Ren, X. *et al.* A small-molecule inhibitor of NF-κB-inducing kinase (NIK) protects liver from toxin-induced inflammation, oxidative stress, and injury. *The FASEB Journal* **31**, 711–718 (2017).

154. Blaquiere, N. *et al.* Scaffold-Hopping Approach To Discover Potent, Selective, and Efficacious Inhibitors of NF-κB Inducing Kinase. *J. Med. Chem.* **61**, 6801–6813 (2018).

155. Takakura, N. *et al.* A novel inhibitor of NF-κB-inducing kinase prevents bone loss by inhibiting osteoclastic bone resorption in ovariectomized mice. *Bone* **135**, 115316 (2020).

156. Cheng, G. *et al.* Identification of new NIK inhibitors by discriminatory analysis-based molecular docking and biological evaluation. *Arch Pharm (Weinheim)* **352**, e1800374 (2019).

157. Takeda, T. *et al.* Mangiferin, a novel nuclear factor kappa B-inducing kinase inhibitor, suppresses metastasis and tumor growth in a mouse metastatic melanoma model. *Toxicology and applied pharmacology* **306**, 105–112 (2016).

158. Li, Y. *et al.* NIK links inflammation to hepatic steatosis by suppressing PPARα in alcoholic liver disease. *Theranostics* **10**, 3579–3593 (2020).

159. Li, Z. *et al.* Discovery of a Potent and Selective NF-κB-Inducing Kinase (NIK) Inhibitor That Has Anti-inflammatory Effects in Vitro and in Vivo. *J. Med. Chem.* **63**, 4388–4407 (2020).

160. Brightbill, H. D. *et al.* NF-κB inducing kinase is a therapeutic target for systemic lupus erythematosus. *Nat Commun* **9**, 179 (2018).

161. Cheng, G. *et al.* Identification of new NIK inhibitors by discriminatory analysis-based molecular docking and biological evaluation. *Arch. Pharm. Chem. Life Sci* **352**, 1800374 (2019).

162. Mortier, J. *et al.* NF-kappaB inducing kinase (NIK) inhibitors: identification of new scaffolds using virtual screening. *Bioorg Med Chem Lett* **20**, 4515–4520 (2010).

163. Ranuncolo, S. M., Pittaluga, S., Evbuomwan, M. O., Jaffe, E. S. & Lewis, B. A. Hodgkin lymphoma requires stabilized NIK and constitutive RelB expression for survival. *Blood* **120**, 3756–3763 (2012).

164. Pippione, A. C. *et al.* N-Acetyl-3-aminopyrazoles block the non-canonical NF-kB cascade by selectively inhibiting NIK †Electronic supplementary information (ESI) available: Additional

biochemical data, chemistry, NMR characterization of final compounds, and biochemical protocols. See DOI: 10.1039/c8md00068a. *Medchemcomm* **9**, 963–968 (2018).

165. Bugge, A., Dib, L. & Collins, S. Measuring respiratory activity of adipocytes and adipose tissues in real time. *Methods Enzymol* **538**, 233–247 (2014).

APPENDIX A

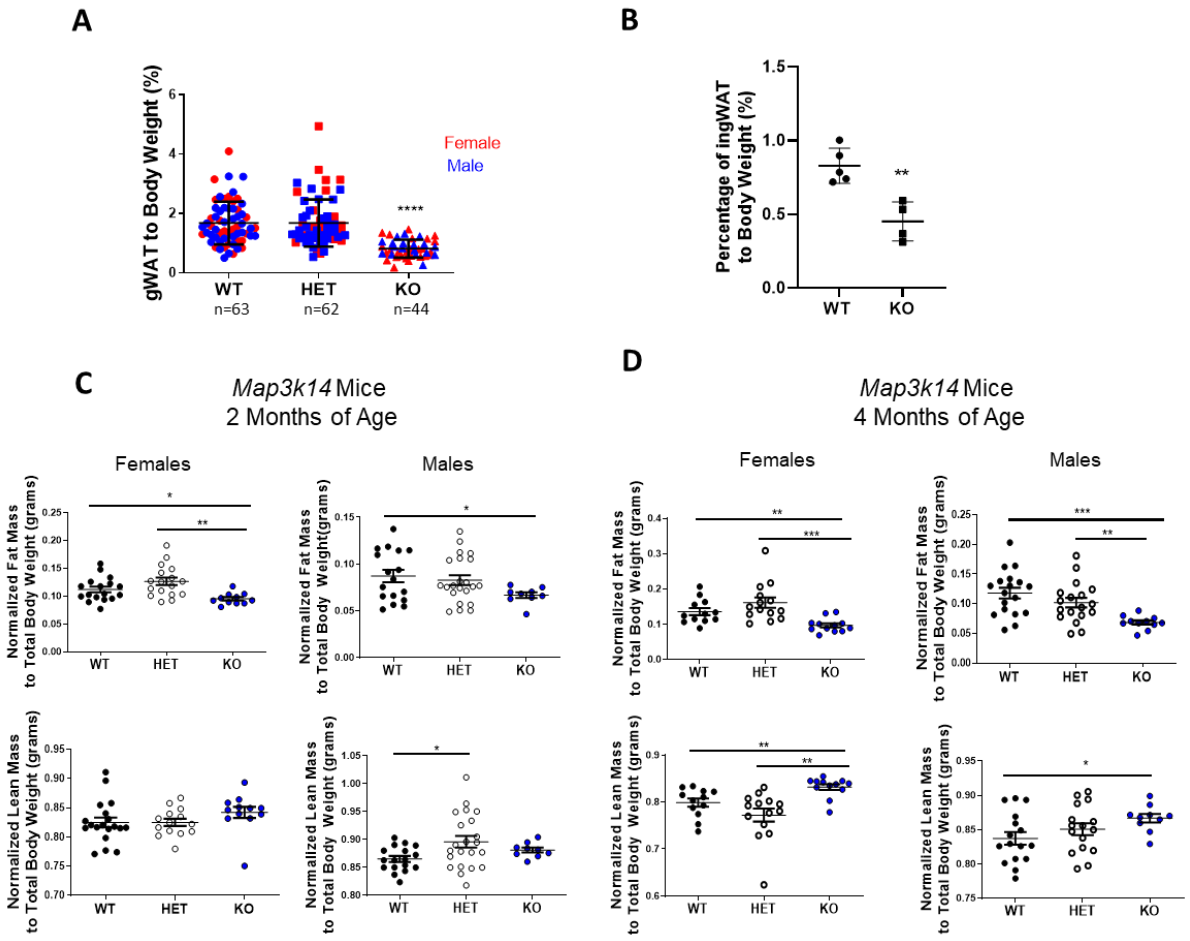

Supplemental Figure 1:

(A) Weights of 4-month-old chow fed WT, HET, and NIK KO male and female gonadal WAT on a chow diet. Data are represented as mean ± SD, **** p ≤.0001, Tukey Multiple Comparison Test. **(B)** Analysis of inguinal WAT from chow fed male WT and NIK KO mice. Data represented as mean ± SD, ** p ≤.01, Unpaired Student t-test. **(C)** Echo MRI data of fat and lean mass ratios of male and female MAP3K14 mice at 2 months and **(D)** 4 months of age. Data mean ± SEM, * p≤.05, ** p ≤.01, *** p ≤.001, Unpaired Student t-test.

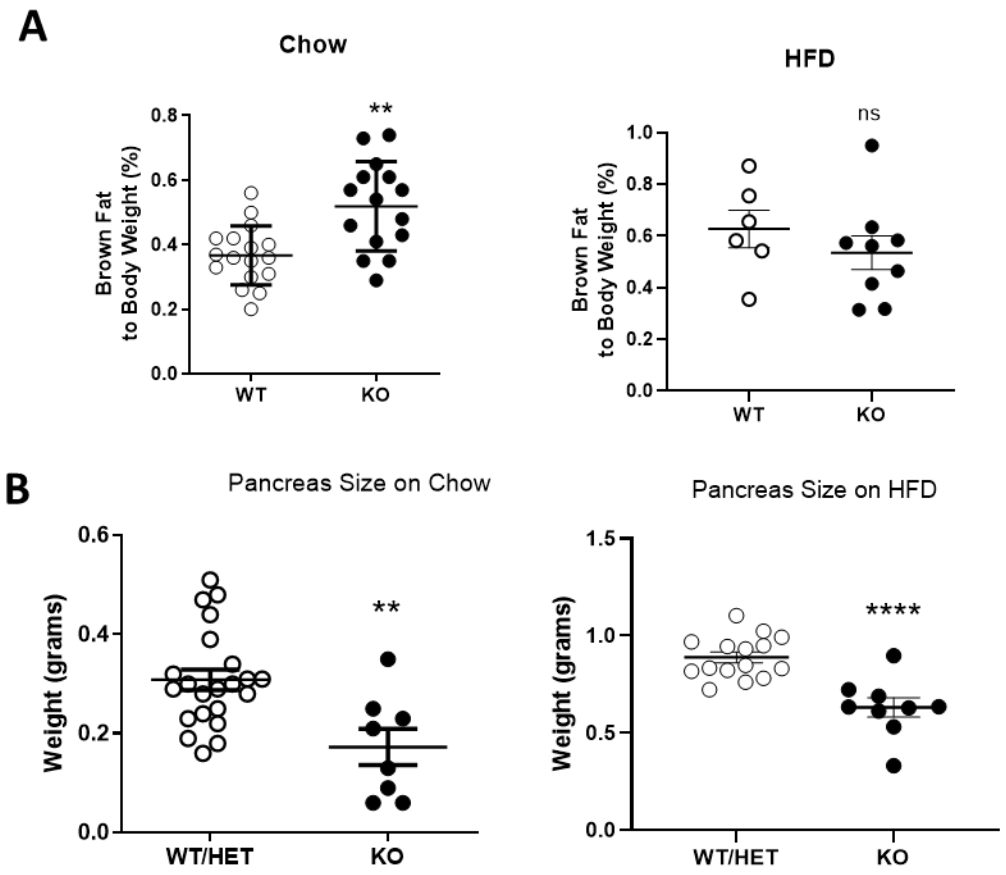

Supplemental Figure 2:

(A) Percentages of brown adipose tissue to body weight from WT and NIK KO male and female mice either on a chow or high-fat diet (HFD). **(B)** Pancreas weights from WT and NIK KO male and female mice either on a chow or (HFD).

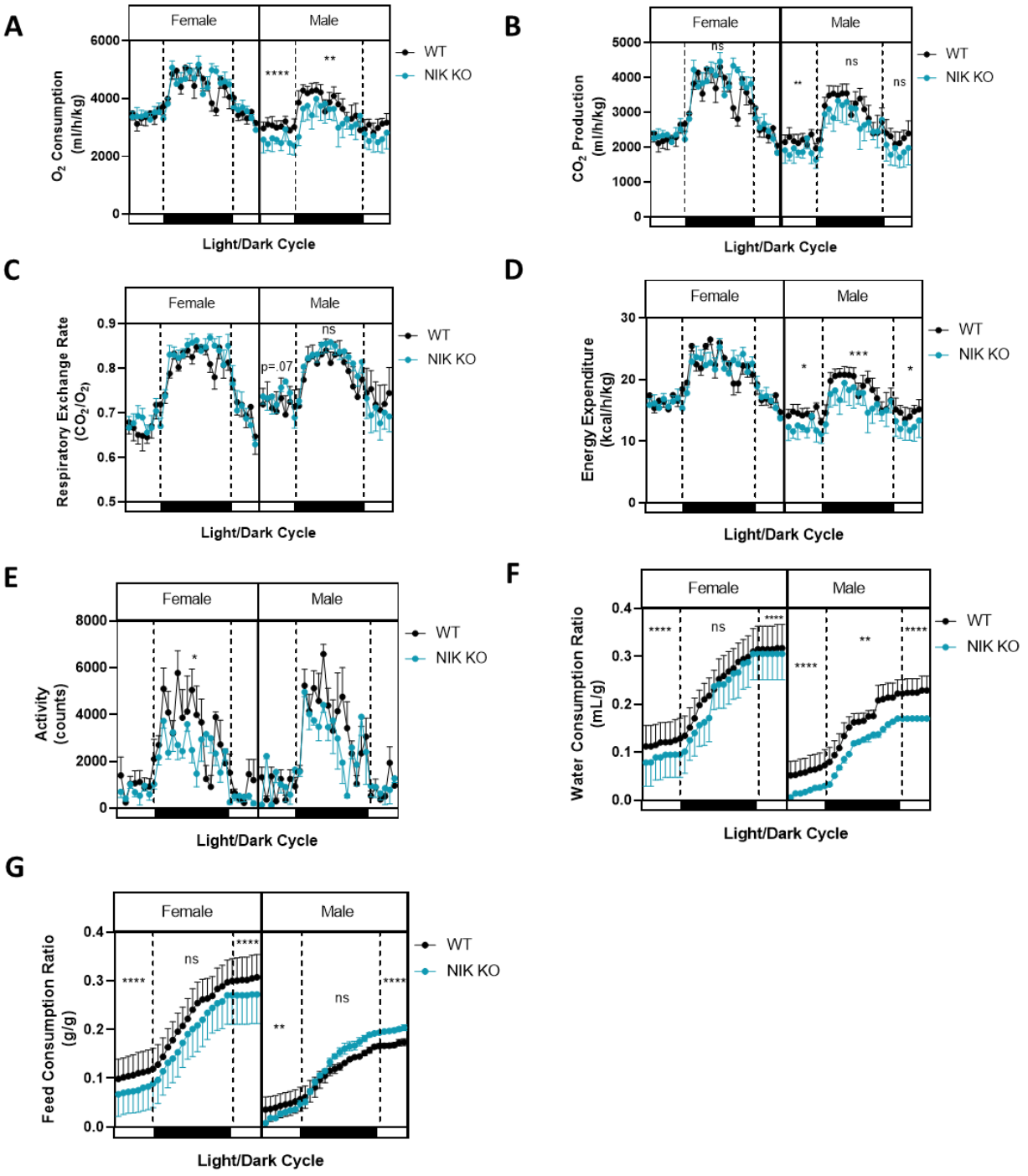

Supplemental Figure 3:

(A-G) Analysis of a 24hr period of metabolic cage data. Representing chow fed male and female, WT and NIK KO mice at 2 months of age. **(A-G)** Data are represented as mean ± SEM, *p≤.05, ** p ≤.01,***p ≤.001, **** p ≤.0001, Unpaired Student t-test.

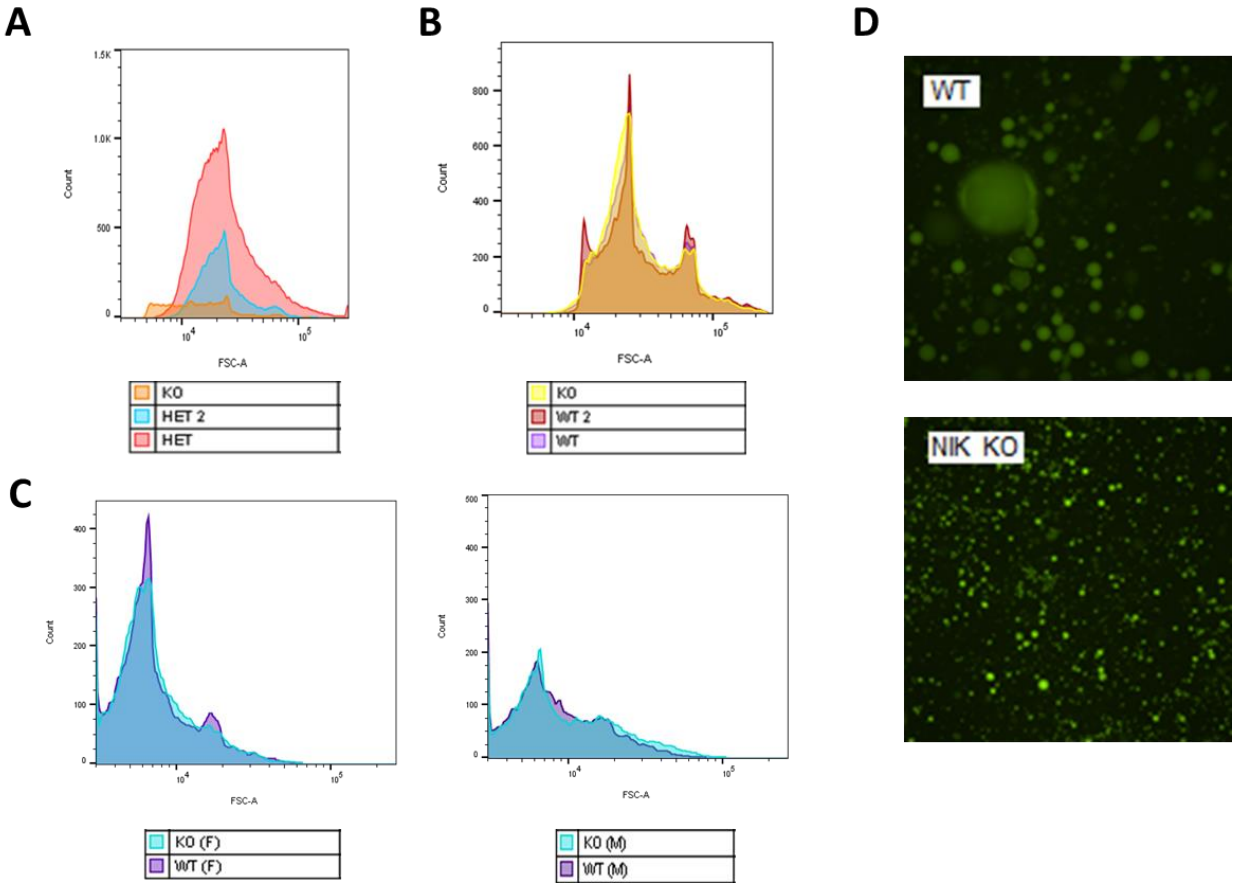

Supplemental Figure 4:

(A-C) Replicates of flow cytometry of isolated adipocyte from mouse gWAT (either male or female on a chow diet). Stained with BODIPY for sorting. **(D)** Images of isolated adipocytes from gWAT stained with BODIPY.

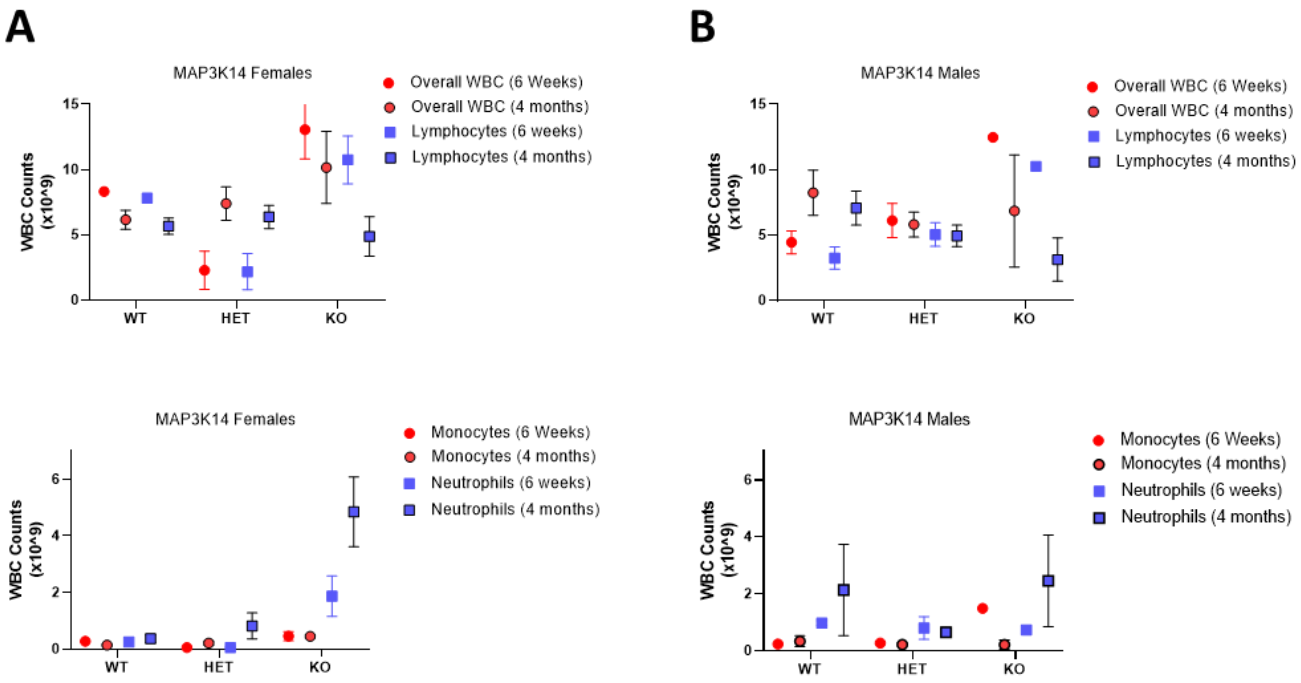

Supplemental Figure 5:

Blood analysis of white blood cells (overall, Lymphocytes, Monocytes, or Neutrophils) from 6 weeks or 4 month old **(A)** females or **(B)** males (on a chow diet).

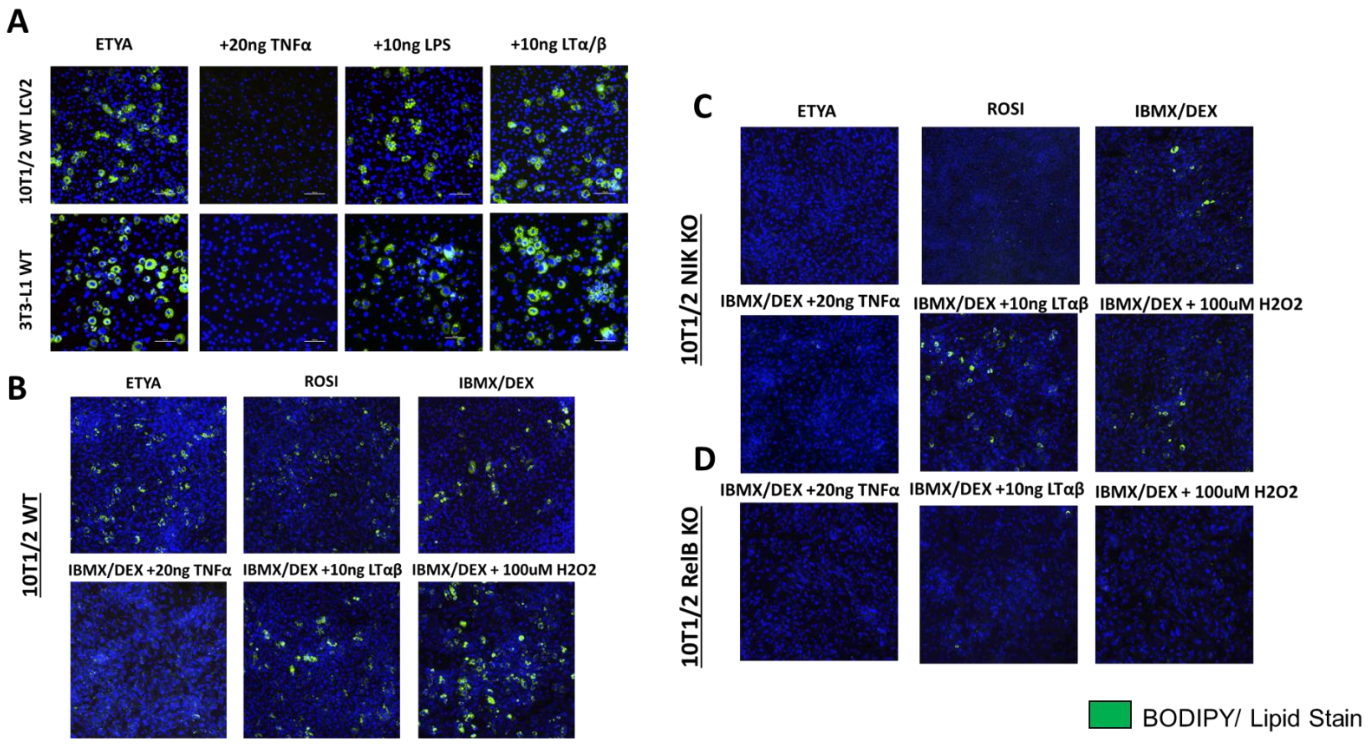

Supplemental Figure 6:

BODIPY lipid staining of **(A)** WT control C3H10T1/2 cells or WT 3T3-L1 cells differentiated with ETYA alone or ETYA with TNFα, LPS, or LTα/β; **(B)** WT, **(C)** NIK KO, or **(D)** RelB KO C3H10T1/2 cells differentiated with ETYA alone, Rosiglitazone (ROSI) alone, Isobutyl-methylxanthine/Dexamethasone (IBMX/DEX) alone, IBMX/DEX + TNFα, IBMX/DEX +LTα/β, IBMX/DEX + H_2O_2.

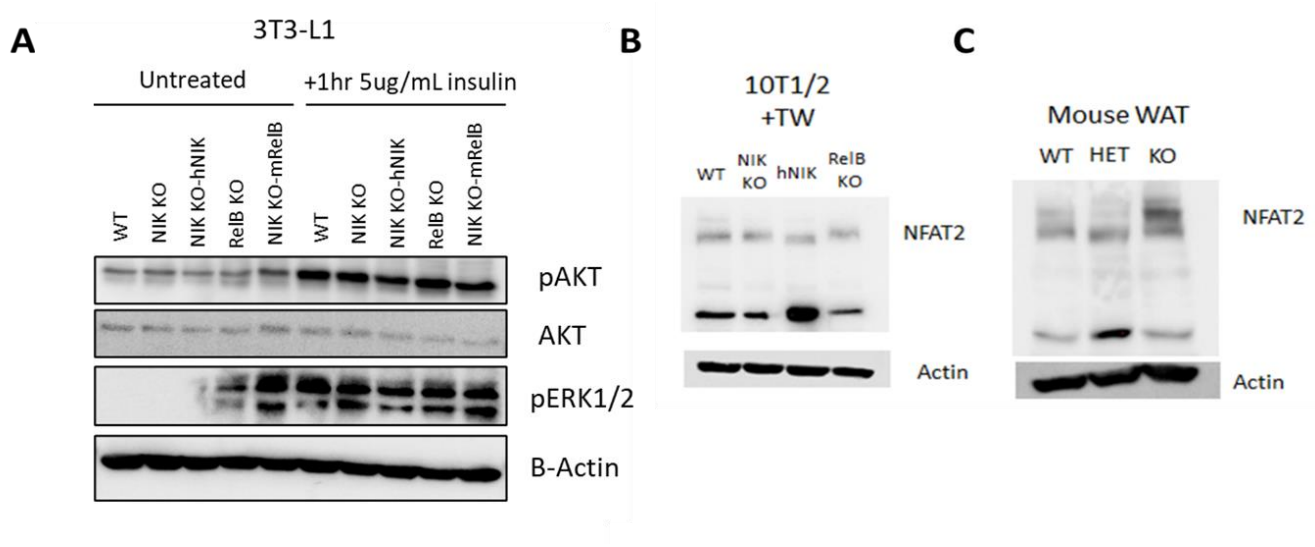

Supplemental Figure 7:

(A) Protein Analysis of AKT and active AKT (pAKT) and pERK1/2 of 3T3-L1 cells with and without insulin. **(B)** Protein expression of the Nuclear Factor Activator of T-cells (NFAT2) in C3H10T1/2 cells treated with TWEAK or **(C)** in mouse gonadal white adipose tissue (gWAT).

APPENDIX B

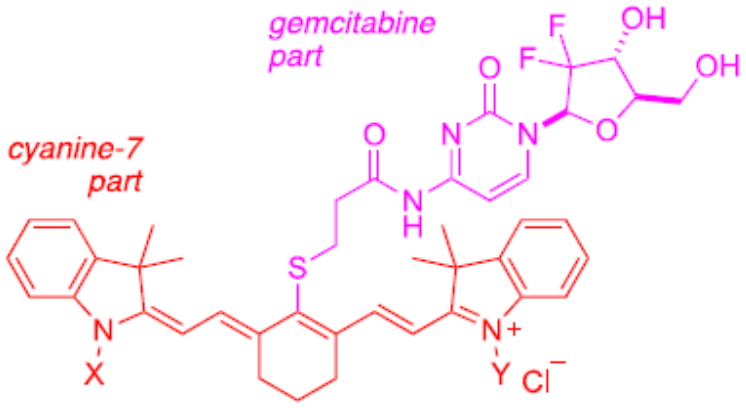

Supplemental Figure 8:

Schematic showing conjugation of Gemcitabine to the meso-chloride of heptamethine cyanine dye, MHI-148. Reprinted with permission from “Cyanine-Gemcitabine Conjugates as Targeted Theranostics Agents for Glioblastoma Tumor Cells” by Jiang *et al*., 2019, *J. Med. Chem*., 62, 20, 9236–9245. Copyright 2019 American Chemical Society.

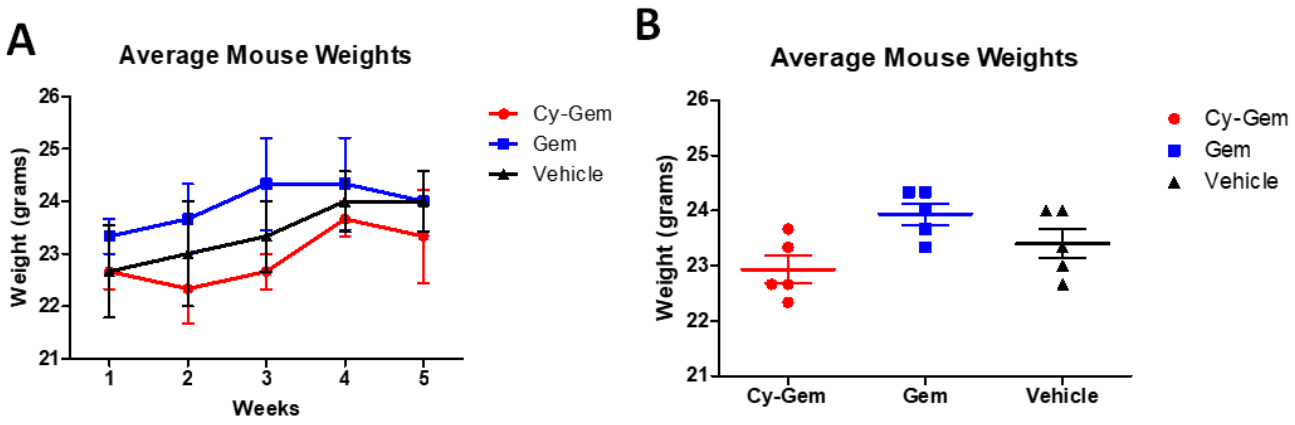

Supplemental Figure 9:

(A) Average of mouse weights in grams by treatment group over 5 weeks with SEM (n=3). Two-way ANOVA with Bonferroni posttest shows no statistically significant differences between groups. **(B)** Average of mouse weights in grams by treatment group with SEM. Points represent average mouse weight by week within a treatment group. (n=3). Two-way ANOVA with Bonferroni posttest shows no statistically significant differences between groups.

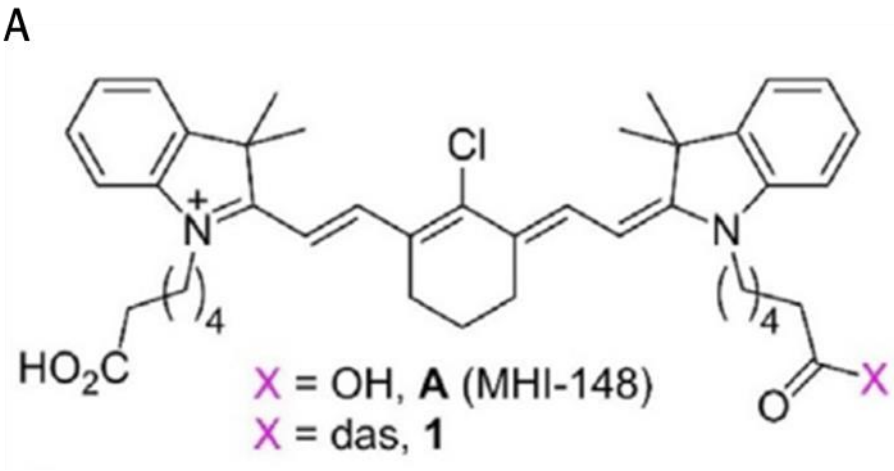

Supplemental Figure 10:

Schematic showing conjugation of Dasatinib to the end hydroxy group of heptamethine cyanine dye, MHI-148. Reprinted with permission from “Cyanine-Gemcitabine Conjugates as Targeted Theranostics Agents for Glioblastoma Tumor Cells” by Jiang *et al*., 2019, *J. Med. Chem*., 62, 20, 9236–9245. Copyright 2019 American Chemical Society.

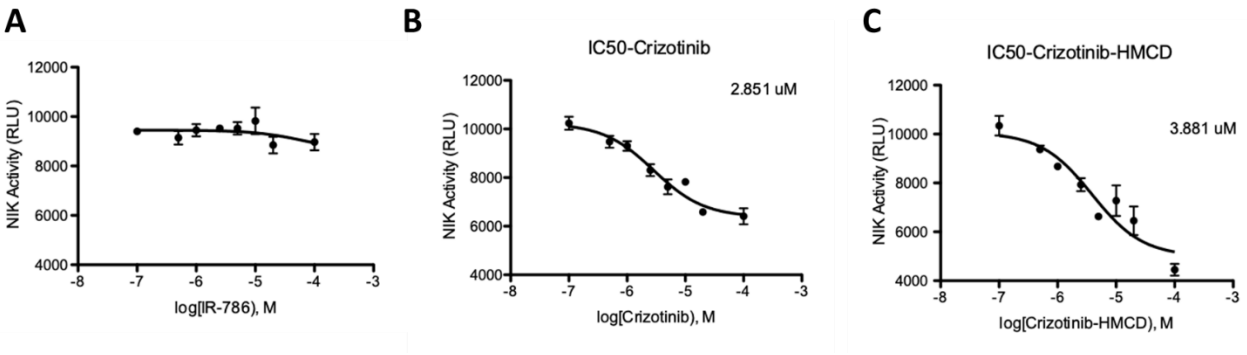

Supplemental Figure 11:

(A-C) Kinase Assay showing NIK activity treated with either **(A)** dye alone (IR-786), **(B)** Crizotinib alone, or **(C)** Crizotinib conjugated to the heptamethine dye (Criz-HMCD). Work done by Dr. Dong Lee.

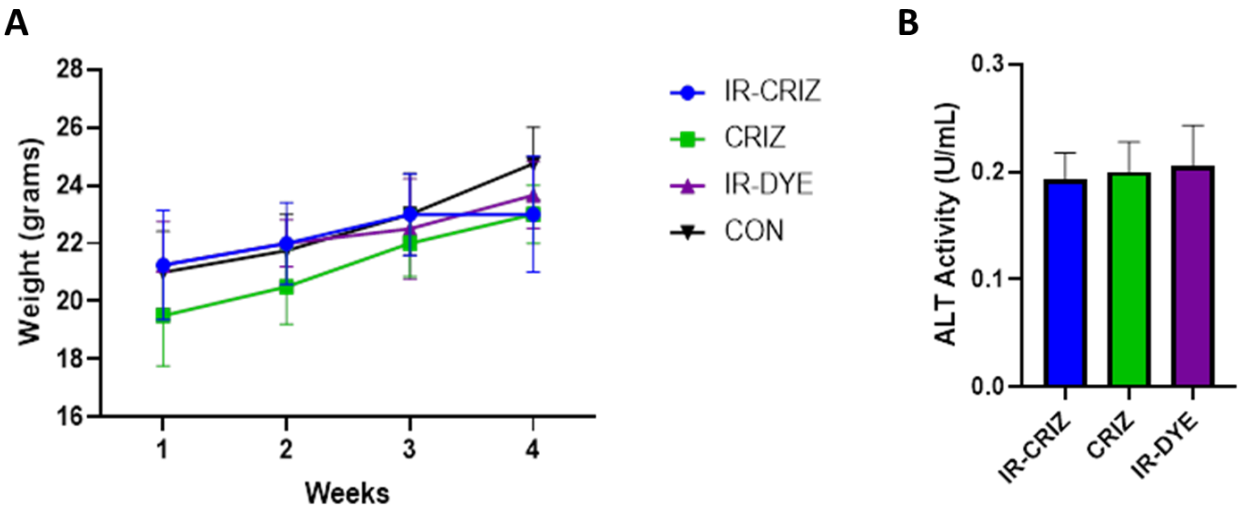

Supplemental Figure 12:

(A) Average mouse weights of mice with intracranial GBM and treated with IV injections of IR-Criz, Criz, or Dye alone. **(B)** Alanine Transferase levels in the plasma of tumor bearing mice treated with IV injections of IR-Criz, Criz, or Dye alone.

APPENDIX C

MATERIALS & METHODS

Animal Work

All animal experiments were done in accordance with animal use protocol (2019-0102) with approved IACUC guidelines. *Map3k14* mice were purchased from Jackson lab (B6N.129-Map3k14tm1Rds/J) and maintained by heterozygous breeding.

Cell Culture

Preadipocyte cell lines, C3H10T1/2 and 3T3-L1 were cultured in DMEM supplemented with 10% FBS, 100 U/ml penicillin and 0.1mg/ml streptomycin (Thermo Fisher Scientific, Waltham, MA). 293 T cells were obtained from ATCC (www.atcc.org) and cultured in DMEM supplemented with 10% FBS, 100 U/ml penicillin and 0.1mg/ml streptomycin. Bone marrow MSC cells were isolated from the femurs of mouse and cultured in DMEM supplemented with 10% FBS, 100 U/ml penicillin and 0.1mg/ml streptomycin**.**

Bone Marrow Cell Isolation

Mouse femurs are collected and sterilized in 70% ethanol for 5 minutes and then transferred to a 50mL conical tube of sterile PBS on ice. Afterwards, femurs were crushed in sterile PBS in a mortar with a pestle that was also sterilized with 70% ethanol. From the crushed femurs, 5mL of DMEM (with 10% FBS and 1% penicillin/streptomycin) is then used to collected cells into a 50mL conical tube through a 70μM filter. The femurs are re-crushed and cells are collected with another 5mL of DMEM. Cells are then centrifuged at 1500rpm for 8 minutes. Media is removed and the

cell pellet is resuspended in 3mL of ACK lysis buffer (Lonza 10-548E) for 2 minutes. ACK cell suspension is diluted with 10mL of media and pelleted again. The cell pellet is resuspended in 10mL of media and filtered through a 40μM filter. Cells are plated at 10 x 10^6 cells /15cm dish (untreated TC plates are used).

CrispR-Cas9 Gene Knockout

NIK: Oligos encoding guide RNAs for murine NIK (gNIK- 1: AGGAUGGGGCAUUCCGCUGU gNIK-2: UGGAGCGCAUGCACCAGGUA, gNIK-3: AGUAUCGAGAAGAGGUCCAC) RelB: Oligos encoding guide RNAs for murine RelB (g RelB-1: AGCGGCCCUCGCACUCGUAG, gRelB-2: GCGCUUCCGCUACGAGUGCG, gRelB-3: ACUGCACGGACGGCGUCUGC) Each gRNAs were cloned into Lenti-CrispR-v2 (Addgene, Cambridge, MA) respectively. C3H10T1/2 and 3T3-L1 cells were transduced with a mixture of lentiviruses (described below) carrying the three murine gRNAs. Puromycin resistant single colony cells were isolated by serial dilution and experiments were repeated with at least two clones. Loss of NIK or RelB expression was confirmed by immunoblot analysis. For controls, cells were transduced with empty LentiCrispR-V2.

Gene Overexpression

Lentiviral construct of over-expression constructs (NIK, IKKα, RelB, RelA, PPARγ and C/EBPα) was obtained from DNASU (Tempe, AZ).

Lentivirus Production

24µg of lentiviral plasmids and 72µg of polyethyleneimine (Sigma-Aldrich) were used to transfect 293T cells. After 3 days of transfection, viral supernatant was concentrated 20 fold to 500µl using Lenti-X Concentrator (Clontech, Mountain View, CA), and 100µl of concentrated virus was used to infect cells. Stably transduced cells were selected for 72hr in medium containing .6µg/ml puromycin or 6µg/ml blasticidin (Thermo Fisher).

Seahorse Extracellular Flux Analysis

Cells

Metabolic activity was analyzed using a Seahorse XFe96 Analyzer (Agilent, Santa Clara, CA). For 3T3-L1 cells, forty-thousand cells per well in 80µL of media were plated in the collagen-coated (40ng/µL) Agilent Seahorse XFe96 microplates and left to settle overnight before analysis with the FluxPak kits according to company standards. Mitochondrial Stress Tests were conducted according to the manufacturer's guidelines. Base media was supplemented with 25mM glucose (Sigma, G7021, St. Louis, MO), 2mM glutamine (Sigma, G85420, St. Louis, MO), and 1mM pyruvate (Gibco). Inhibitors were used at the following final concentrations (10x inhibitor was added to injection ports to reach final concentration): 1µM oligomycin A (Sigma, 75351, St. Louis, MO), 2µM FCCP (Sigma, C2920, St. Louis, MO), and mixture of 0.5µM rotenone (Enzo Life Sciences, Farmingdale, NY, ALX-350-360) and 0.5µM antimycin A (Sigma, A8674, St. Louis, MO).

For Glycolysis Stress Tests, cells were plated in a similar manner, but glucose-starved for 1hr in Seahorse DMEM base media with 2mM glutamine before analysis. Reagents

for injections were used at the following final concentrations (10x reagent was added to injection ports to reach final concentration): 10mM glucose (Sigma, G7021), 10uM oligomycin A (Sigma, 75351), 50mM 2-DG (Thermo Fischer Scientific, 50-519-066). After Seahorse analysis, DNA content was measured using DRAQ5 staining (Thermo Fisher Scientific, 50-712-282) for normalization. Analyses were conducted using Seahorse Wave Controller Software v2.6 and XF Report Generators (Agilent Technologies).

Tissue

Analysis of metabolic activity of adipose tissue was adapted from PMID: 24529442 [165]. 96 well Seahorse plates were coated twice with Cell-Tak (50µg/mL, Corning® Cell-Tak™ Cell and Tissue Adhesive, Cat. No. 354240). Tissue was excised fresh, rinsed well in PBS, and cut into small, >1mg, pieces of similar size and plated into the center of the wells. For Mitochondria Stress Test, base media was supplemented with 25 mM glucose (Sigma, G7021), 2 mM glutamine (Sigma, G85420), and 1 mM pyruvate (Gibco). Inhibitors were used at the following final concentrations (10x inhibitor was added to injection ports to reach final concentration): 20µM oligomycin A (Sigma, 75351), 20µM FCCP (Sigma, C2920), and mixture of 20µM rotenone (Enzo Life Sciences, ALX-350-360) and 20µM antimycin A (Sigma, A8674).

For Glycolysis Stress Test base media was supplemented with 2mM glutamine, and reagents for injections were used at the following final concentrations (10x reagent was added to injection ports to reach final concentration): 25mM glucose (Sigma, G7021),

20μM oligomycin A (Sigma, 75351), 100mM 2-DG (Thermo Fischer Scientific, 50-519-066).

Run time for tissue was increased to 30 minutes per injection with four measurements per compound (4 cycles of 3 min mix, 1.5 min wait, 3 min measure). Afterwards, tissue was homogenized and lysed and normalized by protein.

Immunofluorescence

For immunofluorescence of C3H10T1/2 mitochondria staining, cells were transfected with 1μg DsRed2-Mito-7 (Addgene Plasmid #55838) by lipofectamine (Invitrogen L3000008) for 48-72hrs. Cells were then fixed with 4% PFA for 20 minutes at 37°C. After fixation, cells were washed twice with PBS and then stained with Hoechst (1:1000) diluted in 1% BSA, .1% Triton-X in PBS for 10 minutes. Cells were imaged by confocal (Nikon TI A1R inverted confocal microscope).

BODIPY Staining

For immunofluorescence imaging, BODIPY™ 490/509 (4,4-Difluoro-1,3,5,7,8-Pentamethyl-4-Bora-3a,4a-Diaza-s-Indacene) (Sigma Aldrich 790389) was used. 5mM of BODIPY dye was diluted 1:2500 in PBS and incubate on live cells for 10 minutes at 37°C. Afterwards, cells were washed twice with PBS and then fixed in 4% PFA for 20 minutes at 37°C. After fixation, cells were washed twice with PBS and then stained with Hoechst (1:1000) diluted in 1% BSA, .1% Triton-X in PBS for 10 minutes. Cells were imaged by confocal (Nikon TI A1R inverted confocal microscope).

ATPlite

Tissue was normalized by weight (about 5mg) and ran in triplicate. Tissue was lysed using kit reagents, following manufacture guidelines (Perkin Elmer, 6016941). Lysates were measured for luminescence. Knockout was normalized to respective wildtype sample per run for fold change.

2-NBDG Uptake

Small pieces of tissue (about 2-5mg) were cut from subcutaneous and gonadal WAT and placed in a 96well plate in duplicate or triplicate with 300µg/mL2-NBDG (Cayman, 11046) (enough to cover tissue, about 50-100µL). Tissue was then incubated at 37°C for 1 hour. Afterwards, tissue was washed with PBS 2x and then lysed. Supernatant was then analyzed by plate reader for 2-NBDG (455-570nm). Fluorescent readouts are normalized to protein content.

Lipolysis

About 2-5mg was placed in a 12 well plate in duplicate or triplicate. Tissue was left to sit in 300µL DMEM without FBS for an hour in the incubator. Then 100µL of media was removed for t=0 and isoproterenol was added for a final concentration of 100µM. Tissue was incubated with the isoproterenol for an hour and then 30µL of media was removed for t=1 timepoint, final samples were taken after overnight incubation. 10µL of each sample at the different points were mixed with160µL of glycerol reagent (Sigma, F6428) and read at an absorbance of 540nm for glycerol levels.

Adipocyte Differentiation

Adipocyte differentiation was induced by treating confluent cells for 2 days with 5 µg/ml insulin (Thermo Fisher Scientific) and 100µM ETYA (final concentration 10µM) (Santa Cruz Biotech, Dallas, TX) in Dulbecco's modified Eagle's medium containing 10% FBS, and then every 2 days for 6 Days with insulin (5 µg/ml) dissolved in the same medium. Treatment with NIK inhibitor B022 was purchased from MEDCHEM EXPRESS (Cat. No. HY-120501) and used at a dosage of 5µM.

TNFα (ProSpec CYT-223) and TWEAK (PeproTech 31006) were used at 10ng/mL.

Oil Red O Staining

For the Oil Red O staining, Oil Red O staining solution (0.5% Oil-Red O in isopropyl alcohol solution-distilled water [60:40]) was filtered through the Whatman no. 1 filter paper. Cells were fixed with 10% formaldehyde solution for 30 min at 37°C, then washed with 60% isopropyl alcohol followed by staining with the filtered Oil Red O solution for 20 min and then washed with distilled water three times.

To measure Oil Red O staining of adipocyte differentiated cells, dye is eluted with 100% isopropanol for 10 minutes. Eluted dye is transferred to 96 well plate and optical density measurements were done on Perkin Elmer plate reader at 500nm, .5 sec.

Immunoblot

Cells were lysed in RIPA lysis buffer (Thermo Fisher Scientific) with protease/phosphatase inhibitor cocktail (Thermo Fisher Scientific). Equal amounts of protein were mixed with NuPage 4X LDS sample buffer (Thermo Fisher Scientific) containing reducing agent and denatured at 100˚C for 7 min. Proteins were separated

on 8% ~ 12% SDS-PAGE and transferred to nitrocellulose membranes (Amersham). The membranes were blocked for 1h with 5% non-fat dry milk in 0.1% Tween-20/TBS (TBST) and incubated with primary antibodies diluted in blocking buffer at 4°C overnight. After washing in TBST, membranes were incubated with goat anti-rabbit IRDye800CW (LI-COR Biosciences), goat anti-mouse IRDye680 (LI-COR Biosciences) or goat anti-rabbit HRP conjugate (Thermo Scientific) diluted in blocking buffer and incubated for 1 hour at room temperature. The blots were washed with TBST and developed using Chemiluminescent HRP Substrate (EMD Millipore) for detection of HRP or an Odyssey Infrared Imaging system (LI-COR Biosciences) for detection of IRDye fluorescent dyes.

Antibodies

Following antibodies were used C/EBPα: CST8178 (Cell Signaling Technology), GPD1 (sc-376219) (Santa Cruz Biotechnology, Dallas, TX), IKKα: CST2682, NFKB2: CST4882, NIK: CST4994, p-RelA (p-p65) (CST3033), RelA (p65) (sc-8008), PPARγ: CST2443, RelB: CST4992, GAPDH: sc137179 and β-actin: sc69879.

RNA Isolation, cDNA Synthesis, and Quantitative-RT-PCR

Cells

Total RNA was isolated from cells by Purelink™ RNA Mini Kit (Life Technologies). cDNA was synthesized from 1 µg total RNA using iScript reverse transcription supermix (Bio-Rad, Hercules, CA) following the manufacturer's protocol. Quantitative RT-PCR

was performed using iTaq Universal SYBR Green Supermix (Bio-Rad) with StepOnePlus Real-Time PCR System (Applied Biosystems, Foster City, CA).

Tissue

Mouse tissue was used frozen or fresh after harvesting. Tissue was frozen with liquid nitrogen and ground to a powder with a pestle in a mortar (a minimum of 50mg of tissue is needed, for WAT 1g may be needed). Tissue was then lysed with Trizol (1mL per gram of tissue). For WAT, samples were centrifuged after being lysed and the top layer of the fat cake was punctured with a pipette and the supernatant was removed without collecting the fat layer or pellet. 1/5th the volume of chloroform was then added (200µL chloroform: 1mL Trizol). 400-500µL (for 1mL of Trizol and 200µL of chloroform) of the upper, aqueous layer was transferred to a new tube being careful not to disturb the interphase. Equal volume of pure 70% ethanol was then added to the tube. RNA was then collected in subsequent steps using Invitrogen Purelink RNA mini kit. Zymo DNAse was used with 40-80µL per sample. cDNA was synthesized from 2µg of RNA using iScript reverse transcriptase and buffer mix.

Target Gene	Forward Sequence	Reverse Sequence
SLC2a4 (GLUT4)	5'- GAA ACC CAT GCC GAC AAT GA -3'	5'- CTG TGC CAT CTT GAT GAC CG -3'
LEP (Leptin)	5'- TTC CTG GTG GCT TTG GTC CTA -3'	5'- AGC ACA TTT TGG GAA GGC AG -3'

AIPOQ (Adiponectin)	5’- GTT GCA AGC TCT CCT GTT CC -3’	5’- GAG CGA TAC ACA TAA GCG GC -3’
GPD1	5’- ACA CCC AAC TTT CGC ATC AC -3’	5’- TAG CAG GTC GTG ATG AGG TC -3’
GAPDH	5’- CTT TGT CAA GCT CAT TTC CTG G -3’	5’- TCT TGC TCA GTG TCC TTG C -3’
RPLP0	5’-AAG CGC GTC CTG GCA TTG TCT-3’	5’-CCG CAG GGG CAG CAG TGG T- 3’

3T3-L1 gene expression was normalized to GAPDH.

Mouse tissue gene expression was normalized to RPLP0.

Histology

Mouse tissue was fixed in 10% formalin for 24hrs. WAT was serially dehydrated in 50% ethanol for 2 days and then in 70% ethanol before processing and paraffin embedding. Liver stained with Oil Red O was fixed similarly, but then embedded in a tissue block with OCT for cryo-sectioning. WAT tissue was then stained with hematoxylin and eosin.

Whole Mount WAT Staining

Small portions of dissected gonadal adipose tissue were stained with BODIPY™ 490/509 (4,4-Difluoro-1,3,5,7,8-Pentamethyl-4-Bora-3a,4a-Diaza-s-Indacene) (Sigma Aldrich 790389) (5uM diluted 1:2500 in PBS) for 20 minutes at 37°C. Tissue was then then rinsed in PBS and fixed in 4% PFA overnight. Afterwards, the tissue is rinsed again

with PBS and stained with Hoechst (1:1000) for 15 minutes. Tissues are then placed in an 8-chamber slide with PBS and imaged with a Nikon microscope.

Adipocyte Size Analysis

Adipocyte sizes were analyzed unbiasedly from 10x H&E histology or 10x whole mount BODIPY stained images in adiposoft plugin from ImageJ.

Animal Diet

Chow diet contained 4% fat while HFD diet contained 45% fat (Lab Supply 58125). Mice analyzed on a HFD were weaned from adults on a HFD and then maintained on a HFD for at least 2 months.

EchoMRI™

EchoMRI™ 100H machine was used to analyzed fat and lean mass of chow and HFD mice at 2 or 4 months of age. Mice were weighed before imaging and imaged in MRI tubes.

Metabolic Cages

Metabolic analysis on the mice was conducted in TSE Phenomaster™ metabolic cages through Rodent Preclinical Phenotyping Core at TAMU (https://genomics.tamu.edu/preclinical-phenotyping/). Mice were weighed the day of and housed individually for 48hrs. Data was analyzed based on last 24hrs to compensate for mouse adjustment to the new environment.

Glucose Tolerance Testing

For glucose tolerance testing mice were morning fasted for 6hrs in clean cages. Mice were weighed and from tail clip initial glucose levels are recorded from glucose meter. The mice are then intraperitoneally injected with 20% D-glucose at 2g/kg (µL= 10 x BW). Blood glucose (in mg/dL) is then recorded at t=15, t=30, t=60, t=120 minutes post injection.

Insulin Tolerance Testing

For insulin tolerance testing mice were morning fasted for 4hrs in clean cages. Mice were weighed and from tail clip initial glucose levels are recorded using a glucose meter. The mice are then intraperitoneally injected with.5 U/kg Insulin (µL= 5 x BW of .1 U/mL insulin). Blood glucose (in mg/dL) is then recorded at t=15, t=30, t=45, t=60, t=90 minutes post injection.

MTS Proliferation Assay

BT25-RFP-LUC cells were plated 5,000 cells per well among 4 96 well plates for a four day time course. Compounds were treated at a final concentration of 5µM at day 0 in 100 µL of media. Each day 20µL of MTS (Promega, G3582) was mixed with the media, incubated at 37°C for 1 hour and then absorbance was read at 490nm.

Sphere Assay

200cells/200µL of BT25-RFP-LUC cells were plated in triplicate-quadruplet in a 96 well plate. Cells were grown up for 3 days and then treated with 5µM of the various

compounds and then grown for the rest of the week with the inhibitors. Wells were then imaged under brightfield at 4x.

Invasion Assay

Collagen was prepared for a final concentration of 2.0mg/mL. 28µL of collagen mixture was plated in in half well 96 well plates. Plate with collagen was then incubated for 45 minutes at 37°C. BT25-RFP-LUC cells were then plated at 50,000 cells/well in complete DMEM F12, and compounds were added to media at a final concentration of 5µM. 2 days later cells were fixed with 3% glutaraldehyde for 30 minutes and then stained with toluidine blue. Invading cells were counted under a 25x objective.

Xenograft Experiments

All animal experiments were done in accordance with AUP/IACUC guidelines. 7-week-old Foxn1 nu females were ordered from Jackson Lab. 5x10e5 U87-RFP-LUC cells were injected subcutaneously into the right flank of the mice or injected intracranially.

Tumor growth was monitored by luminescence (with D-luciferin injections and fluorescence (RFP; 570-620nm)

Intravenous Chemotherapeutic Injections

Three to four days post tumor cell injection intraperitoneal (IP) or intravenous (IV) injections of the drugs and vehicle were administered with IV injections being administered by retro orbital injections. For Cy-Gem/Gem experiment, the mice were

injected again 4 days later (Day 8), and the injections were subsequently administered once weekly for 5 weeks. Cy-Gem was prepared as 3 mM solution and gem was prepared as 10 mM solution diluted in 2% DMSO, 9% ethanol, 9% BSA in PBS buffer. For IV injections, volume (< 100 mL) of each compound administered was calculated based on the body weight of each mouse to deliver 10 mg/kg dose. For IR-CRIZ/CRIZ experiment, compounds were diluted in 10% DMSO and 2% TWEEN-80 in PBS. IR-CRIZ/CRIZ were injected by IV once a week at 3mg/kg from fresh 2mM stocks. Dasatinib and Cy-Das were injected by IP from 5mM stocks diluted in 10%DMSO in PBS. Drug clearance/localization of cyanine dyes and conjugated compounds was monitored by fluorescence imaging (745-840nm).

Fluorescence/ Luminescence *In Vivo* Imaging

Mice were anesthetized with isoflurane and then imaged for fluorescence or luminescence on an IVIS Spectrum (in vivo imaging system; Perkin Elmer). For luminescence imaging, mice were subcutaneously injected with D-Luciferin (15mg/mL; Perkin Elmer, cat. no. 122796) in µLs at 10x the mouse's weight. During imaging mice remained anesthetized by isoflurane. Fluorescence was measured by radiant efficiency and luminescence was measured by counts. Red Fluorescence Protein (RFP) from the U87 cells was captured at an excitation wavelength of 570nm and an emission wavelength of 620nm. The near IR dye fluorescence was capture at an excitation wavelength of 745nm and an emission wavelength of 840nm. Images were captured and data were analyzed using Living Image Software (Perkin Elmer).

H&E Staining

Brain tissue was fixed in 4% PFA overnight and dehydrated in 30% sucrose. Tissue was then embedded in OCT and frozen at -80C. Tissue was cryosectioned at 20 microns and then stained with Mayer's Hematoxylin and Eosin. Slides were imaged on Lion Heart imager by Biotek with 4x images stitched together.

Statistical Analysis

Statistical Analysis was done using GraphPad PRISM software, specifics on data representation and tests used for analysis can be found in figure legends. *p ≤.05, ** p ≤.01, *** p ≤.001, **** p≤.0001. Unpaired student t-tests were ran as two-tailed. All statistically significant analysis were ran based on a 95% confidence interval.